Lire
la première partie
de la thèse

Chapter 6

LES of confined bluff body gas-solid flow

The conclusions of the particle-laden turbulent confined jet presented in Chapter 5 are limited to simple geometries. However in the context of combustion, such a configuration is often prohibited because the resulting jet flame is too long in comparison with the length of the combustion chamber, and is difficult to stabilise. Thus, most combustion devices are designed so as to anchor the flame at a specific location. The use of a flame holder is tricky due to the very high temperatures that may damage the device itself. Another possibility is to stabilise the flame behind a sudden expansion like a backward-facing step, like in gas ovens for instance. The flow is strongly decelerated and forms a corner recirculation zone (CRZ). The recirculating hot gases provoke the ignition of the incoming fresh gases. As far as aeronautical combustion chambers are concerned, highly swirling flows that pass through a sudden expansion are preferred since they provide a much more compact stabilised flame. A central toroidal recirculation zone (CTRZ) is created, acting as a flame holder in the center of the flow, close to the injector tip. The combustion chamber of the Mercato test-rig, experimentally and numerically investigated respectively at ONERA and CERFACS, exhibits the two types of recirculation zones, as shown in Fig. 6.1. In such devices, the recirculation zones induce high turbulence levels and high mixing rates, which greatly stabilises the flame and also reduces pollutant emissions. Before computing reactive two-phase flows in such devices, which requires evaporation and combustion modeling, a validation of the turbulent dispersion of the particles is needed. Indeed, the accurate description of the fuel droplet motion is crucial to determine the resulting fuel vapor distribution. To this purpose, a particle-laden confined bluff body experimentally investigated by Borée *et al.* (2001) in a flow-loop of EDF-GDF is focused on hereafter. A large amount of detailed data is available in this geometry where a jet of air and solid particles emerges without any swirl in a coflow of air. RANS simulations using the EE approach have already been performed by Vit *et al.* (1999). The same kind of experiment, but including a swirling air flow, has been conducted by Sommerfeld & Qiu (1991), and has been simulated by Apte *et al.* (2003*b*) with the EL approach, and by Boileau *et al.* (2007) with the EE mesoscopic approach,

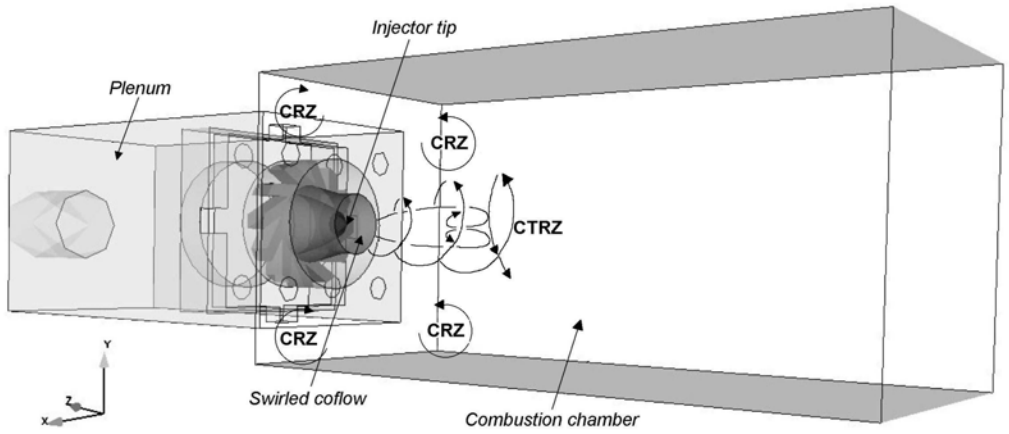

Figure 6.1 - *Sketch of the combustion chamber of the Mercato test-rig.*

with the objective of evaluating the model performances.

Although there is no swirling flow, the bluff body flow from Borée *et al.* (2001) is interesting for aeronautical applications. First, combustion chambers like the Mercato one exhibit the same flow structures with corner recirculation zones and stagnation points. Their accurate prediction is closely linked to the capture of the large structures and the intermittency of the fluid flow (see for instance Chin & Tankin (1992); Schefer *et al.* (1994); Namazian *et al.* (1992)), and requires accurate turbulence modeling. Second, the dispersed phase itself is also important in such devices (Hardalupas *et al.*, 1994; Boileau *et al.*, 2007). Depending on their inertia and their mass loading, the particles remain more or less in the recirculation zones, modifying the burner efficiency as well as the pollutant emissions. With this in prospect, the data provided by Borée *et al.* (2001) allow to test in detail not only the gas LES models, but also the dispersed phase modeling. The objective in this chapter is to study in detail the models behavior and the underlying mechanisms.

Part of this work has been done in collaboration with Marta Garcia and Vincent Moureau during the Summer Program organised by the Center for Turbulence Research (CTR) of Stanford University in July 2006. Such a collaborative work has allowed three different validations, as shown in Fig. 6.2. First, the gas LES solver from AVBP_TPF was confronted to the gas LES solver from CDP[1]. Since the two codes gave very similar results and captured most of fluid

[1]The LES solver CDP developed at Stanford University solves implicitly the incompressible Navier-Stokes equations. The time integration of CDP is based on the fractional-step method (Kim & Moin, 1985) and the space integration relies on a second-order central scheme that conserves the kinetic energy (Mahesh *et al.*, 2004; Ham & Iaccarino, 2004). The dynamic Smagorinsky model (Germano *et al.*, 1991) is used to model the subgrid stress tensor. The dispersed phase is treated using the EL approach described in Section 1.2. More details can be found in Apte *et al.* (2003*b*).

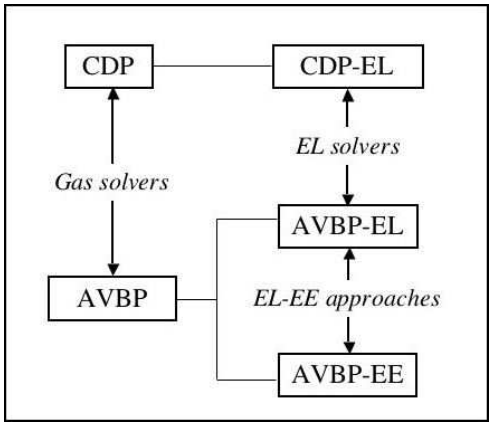

Figure 6.2 - *Methodology adopted to validate the two-phase flow simulations*

flow structures, the EE and EL formulations were then evaluated. This was done in two steps. First, the EL solver from AVBP_TPF developped by García *et al.* (2005)[2] was also confronted to the EL solver from CDP. Then, the EL and EE mesoscopic approaches were compared using the same gas LES solver from AVBP_TPF. Note that the EE mesoscopic approach used in this configuration corresponds to the simplified model tested in Section 5.5 where the RUM contributions are neglected.

Section 6.1 briefly presents the experimental setup, the measurement methods and the available data.
In Section 6.2, the gas phase results are compared and analysed. The sensitivity of the results to the convective scheme, the grid, the LES model, the wall treatment, and the inlet boundary conditions is investigated.
Finally, Section 6.3 deals with the two-phase flow simulation for the lowest mass loading of the central jet and monodisperse particle distribution. The main purpose is to compare the two approaches (EL and EE). For the sake of clarity, only the results obtained with AVBP_TPF using either the EE or the EL approach are shown, the CDP results being available in Riber *et al.* (2006).

[2] In AVBP_TPF, both the EE mesoscopic approach and the EL approach are available. The gas LES solver is identical and only the formulation for the dispersed phase is different.

6.1 Description of the configuration

This section describes the bluff body configuration from Borée *et al.* (2001), explains the underlying concept and details the experimental setup.

6.1.1 Concept and main purpose

Borée *et al.* (2001) created a vertical axisymetrical particle-laden confined bluff body flow (see Fig. 6.3) on the flow loop Hercule of EDF-DER-LNH. Both air and particles are injected in the inner jet whereas air blowers are used to generate the coflow. The measurement zone is located downstream of the inner and annular ducts ($z > 0$), where large recirculation zones are created between the central jet and the coflow due to the geometry. The resulting flow is similar to the flows obtained in industrial combustion devices, where fuel droplets are injected together with air.

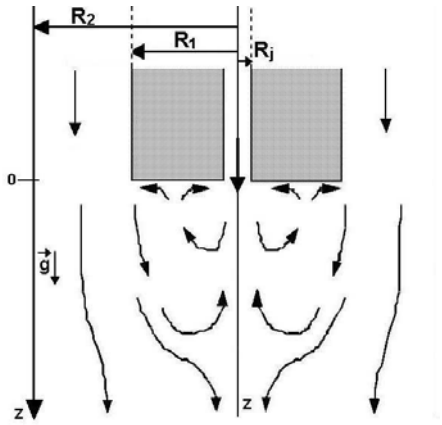

Figure 6.3 - *Schematic of the configuration of Borée* et al. *(2001). The dimensions are :* $R_j = 10$ *mm,* $R_1 = 75$ *mm,* $R_2 = 150$ *mm. The length of the experimental chamber is* 1.5 *m.*

The topology of the gas flow mainly depends on the ratio between the velocity in the inner pipe and the velocity in the coflow. With a low velocity in the annular flow, Borée *et al.* (2001) managed to obtain two stagnation points on the axis. Such a single phase flow has been shown to be very interesting when adding particles. Indeed, particle inertia as well as fluid-particle interactions are the main mechanisms in such two-phase flows (Simonin, 1991).
The volume and the accuracy of the data make this configuration a very good test case to study turbulent closure models. The data include radial profiles of the following quantities at seven stations along the axis ($z = 3,\ 80,\ 160,\ 200,\ 240,\ 320$ and 400 mm) in the measurement zone:

- Mean axial and radial velocity components for the carrier and the dispersed phases,
- RMS axial and radial velocity components for both phases,
- Particle number density and particle mass flux.

Furthermore, axial profiles of mean and RMS axial velocities are provided on the centerline.

6.1.2 Characteristics of the flow for both phases

• The gas phase

The experiments are conducted at ambient temperature, $T_f = 293\ K$, and standard pressure, $P_f = 1.013\ 10^5\ Pa$.
The inner pipe is 1.5 m long and the radius is $R_j = 10\ mm$. The air volume flux of the inner jet is $Q_{f,j} = 3.4\ m^3.h^{-1}$, which corresponds to a mean velocity, $\overline{U}_{f,j} = 3.4\ m.s^{-1}$, whereas the maximum velocity in the inner duct reaches $U_{f,j}^{max} = 4\ m.s^{-1}$. As a result, the Reynolds number is $Re_j = 2R_j\overline{U}_{f,j}/\nu_f \approx 4500$, which is rather low. The ratio $U_{f,j}^{max}/\overline{U}_{f,j} = 1.18$ at the outlet of the inner pipe is however consistent with fully developped turbulent pipe flow.
The dimensions of the annular outer region are : $L_e = 2\ m$, $R_1 = 75\ mm$, $R_2 = 150\ mm$. The air volume flux in the coflow is $Q_{f,e} = 780\ m^3.h^{-1}$, which corresponds to mean and maximum velocities equal to: $\overline{U}_{f,e} = 4.1\ m.s^{-1}$ and $U_{f,e}^{max} = 6\ m.s^{-1}$. The associated Reynolds number of the annular jet is $Re_e = 2\,(R_2 - R_1)\,\overline{U}_{f,e}/\nu_f \approx 40000$.
Table 6.1 summarises this information.

Gas phase	Length (mm)	Radius (mm)	Volume flux $(m^3.h^{-1})$	Mean velocity $(m.s^{-1})$	Max. velocity $(m.s^{-1})$	Reynolds number $(-)$
Inner pipe	1500	10	3.4	3.4	4.	4500
Annular pipe	2000	75	780	4.1	6.	40000

Table 6.1 - *Characteristics of the gas phase at the outlet of the inner and annular pipes. Configuration of Borée* et al. *(2001).*

Schefer *et al.* (1994) show that the topology of a turbulent bluff body flow strongly depends on the ratio $\overline{U}_{f,j}/\overline{U}_{f,e}$. The three possible configurations are illustrated in Fig. 6.4, where sketches of mean gas velocity vectors are drawn for three decreasing ratios: $\overline{U}_{f,j}/\overline{U}_{f,e} = 2.8$, 1.4 and 0.84. Moreover, seeding the gas flow with small particles gives access to photographs of the particle distribution, and so on the flow topology. This is done in Fig. 6.5 by Schefer *et al.*

(1994) for the three ratios given above.
At the highest ratio $\bar{U}_{f,j}/\bar{U}_{f,e} = 2.8$, the flow along the axis is similar to a free-jet flow. The air flows coming from the inner and annular pipes converge far from the outlet of the inner duct. Two counter-rotative eddies separate the two flows before they converge. There is no stagnation point on the axis, but one is visible on both sides of the central jet.
In the vicinity of $\bar{U}_{f,j}/\bar{U}_{f,e} = 1$, a single stagnation point is formed along the centerline and the flow looks like a non-penetrating jet.
When decreasing the ratio down to one, a second stagnation point appears on the axis. The location of the stagnation point closest to the inner pipe is linked to the inner air mass flux. The location of the second one mainly depends on the bluff body geometry, and does not move when $\bar{U}_{f,j}/\bar{U}_{f,e} < 1$. The two counter-rotative eddies move away from each other with decreasing ratio.

In Borée *et al.* (2001), the ratio in the gaseous flow is: $\bar{U}_{f,j}/\bar{U}_{f,e} = 0.83 < 1$. Similarly to Schefer *et al.* (1994), two stagnation points are observed along the centerline. Choosing a ratio lower than one creates an interesting gas flow behaviour when modeling particle dispersion, as the particles, depending on their inertia, are more or less kept in the recirculation zone delimited by the two stagnation points.

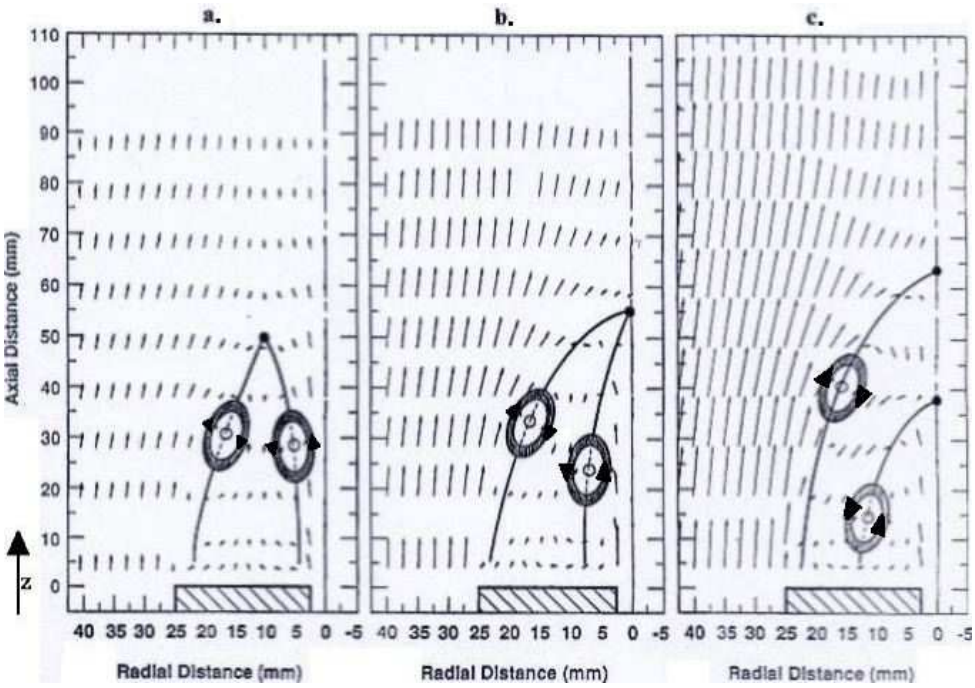

Figure 6.4 - *Plots of the measured mean velocity vectors in a bluff body stabilised methane jet for* $\bar{U}_{f,j}/\bar{U}_{f,e} = 2.8$ *(a.),* $\bar{U}_{f,j}/\bar{U}_{f,e} = 1.4$ *(b.), and* $\bar{U}_{f,j}/\bar{U}_{f,e} = 0.84$ *(c.). Black dots show the location of the stagnation points and round arrays give the direction of rotation of the shear layer vortices. From Schefer* et al. *(1994).*

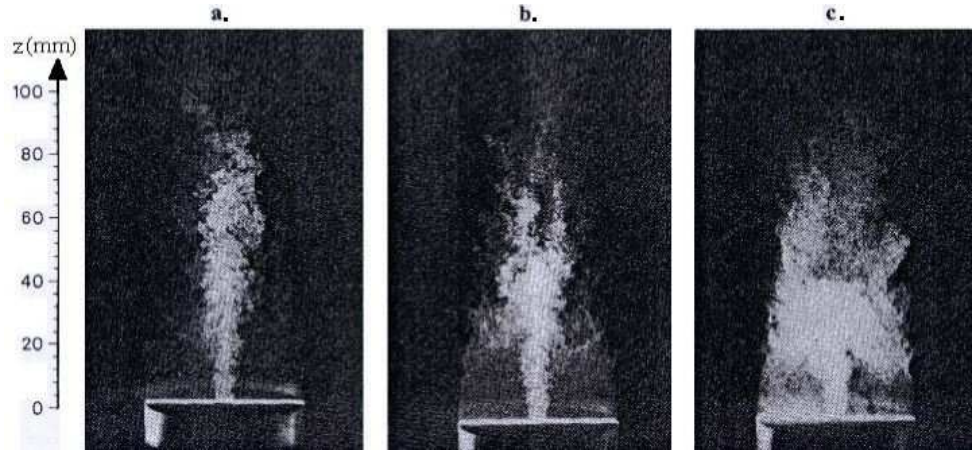

Figure 6.5 - *Mie scattering measurements of the instantaneous particle distribution in a bluff body stabilised methane jet for* $\bar{U}_{f,j}/\bar{U}_{f,e} = 2.8$ *(a.),* $\bar{U}_{f,j}/\bar{U}_{f,e} = 1.4$ *(b.), and* $\bar{U}_{f,j}/\bar{U}_{f,e} = 0.84$ *(c.). From Schefer* et al. *(1994).*

• The dispersed phase

Polydisperse glass particles with material density, $\rho_p = 2470\ kg.m^{-3}$, are injected through a particle feeder in the inner jet only. The particle feeder is located two meters upstream of the inner pipe outlet. Two mass flux of glass beads, $Q^1_{p,j} = 1\ kg.h^{-1}$ and $Q^2_{p,j} = 5\ kg.h^{-1}$, have been experienced to study the influence of particle inertia on the two-phase flow, and also the role of particle-particle collisions. The corresponding mass loading in the inner duct then varies from $M^1_{p,j} = 22\%$ to $M^2_{p,j} = 110\%$.
The particle diameter covers a wide range of size classes from $d_p = 20\ \mu m$ to $d_p = 110\ \mu m$. Figure 6.6 shows the particle distribution, in mass and in number. The resulting mean diameter is respectively $d_{p,M} = 63\ \mu m$ and $d_{p,N} = 50\ \mu m$. Special care has been taken to analyse the particle distribution. It was important to ensure that the glass beads remained spherical and that the particle-particle collisions did not induce any particle break-up. This was confirmed by repeating the measurements and observing the particles with a microscope.

• Characteristic time scales

Table 6.2 gives the relaxation time of the particles τ_p, depending on the particle diameter d_p. To give an order of magnitude of the characteristic time scale of the particles, a Stokes flow around the particles is assumed (see Eq. (1.15) in Section 1.2.1).

The comparison of the particle relaxation time τ_p, with a characteristic time scale of the fluid most energetic eddies $\tau_{f,t}$, gives the Stokes number. Similarly to the particle-laden confined jet flow (see Section 5.1.3), $\tau_{f,t}$ is estimated assuming that the length of the most energetic eddies

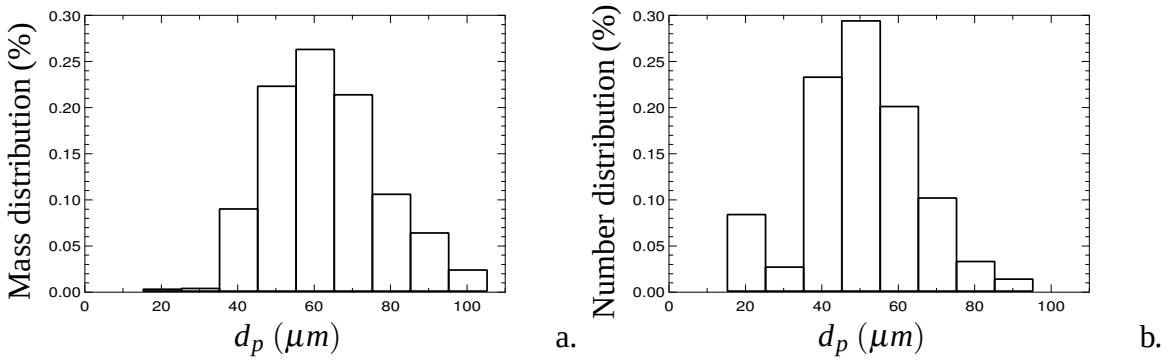

Figure 6.6 - *Initial mass (a.), and number (b.) distribution of the particle size. Configuration of Borée* et al. *(2001).*

$\mathbf{d_p}\ (\mu m)$	20	30	40	50	60	70	80	90	100	110
$\tau_\mathbf{p}\ (ms)$	3.1	6.9	12.3	19.2	27.6	37.6	49.1	62.2	76.7	92.9

Table 6.2 - *Relaxation time of the particles injected depending on their diameter. Configuration of Borée* et al. *(2001).*

corresponds to one third of the duct diameter and their velocity is the maximum fluctuating velocity in the pipe:

$$St = \frac{\tau_p}{\tau_{f,t}} \qquad \text{where} \qquad \tau_{f,t} = \frac{\frac{2R_j}{3}}{u'_{f,max}} \approx 7\ ms \tag{6.1}$$

The influence of particle inertia on the two-phase flow topology increases with the Stokes number. Table 6.3 presents the characteristic Stokes number of the two-phase flow depending on the particle diameter. It comes that the motion of the smallest particles with diameter $d_p = 20\ \mu m$ is expected to be very different from the biggest ones, with diameter $d_p = 110\ \mu m$: while the smallest particles almost follow the gas flow, the inertia of the biggest ones make them much more independent of the fluid flow.

$\mathbf{d_p}\ (\mu m)$	20	30	40	50	60	70	80	90	100	110
$\mathbf{St}\ (-)$	0.4	1.0	1.8	2.7	3.9	5.4	7.0	8.9	11.0	13.3

Table 6.3 - *Stokes number depending on the particle diameter. Configuration of Borée* et al. *(2001).*

Contrary to the configuration of Hishida *et al.* (1987), calculating the supplying pipes is here mandatory since they are at the origin of the large recirculation zones in the chamber itself. In

the inner duct, both air and particles are injected. To determine whether a specific treatment of the particle inlet boundary condition is required (see Section 5.4), it must be quantified if particles have enough time to adapt to the changes in gas mean velocity within the inner duct. To do so, the relaxation time of the particles is compared to their transit time in the pipe.

The transit time of the particles in the inner pipe, T_p^T, is determined using the length of the duct (the starting point is the particle feeder) and the inner maximum gas velocity:

$$T_p^T = \frac{L_j^{'}}{U_{f,j}^{max}} = 250\ ms \tag{6.2}$$

It comes that the particle relaxation time is largely smaller than their transit time in the inner pipe, whatever the diameter considered. Thus, the particles have time to adapt to fluid turbulence before they reach the outlet of the inner pipe and no specific treatment on particle agitation is required at the inlet of the central pipe.

6.1.3 Experimental setup

The mean and RMS velocities, for the gas phase and for each class of particles, are obtained by the Particle Doppler Anemometry (PDA) measuring technique presented in Section 5.1.2.

When dealing with two-phase flows, it is necessary to choose different material for the particles, so that they can be either a measure of the fluid flow or a measure of the dispersed phase itself. Borée *et al.* (2001) used three types of particles: glass beads for the dispersed phase, smoke for the inner jet fluid flow and water droplets for the annular gas flow.

Seeding the flow with so many different particles is a delicate task and specific care has to be taken. As far as the gas flow is concerned, sufficient volume flux of the seeded particles is required. Considering the high annular volume flux, water droplets were a cheap and safe solution. They were injected using four water injectors and they were checked not to collide with each other close to the injector tip. For the inner pipe, smoke particles were more adapted because they did not collide with glass beads. They were added to the central jet using a smoke machine. Both the smoke and water droplets proved to be good tracers. Their diameter was respectively 2 μm and 5 μm, corresponding to particle relaxation times at least 100 times lower than the characteristic time scale of the fluid most energetic eddies. In addition, it was verified that both tracers did not have any effect on the particulate phase measurements, comparing the dispersed phase flow measurements with and without fluid tracers. Finally, all parts of the set-up were grounded and the air flow was humid enough to avoid static electricity influence.

For the dispersed phase, the glass beads did not show any breaking, so that the curvature and the geometric radius remained the same. Their refraction index was $n = 1.51$ and because they were hollow, they were well suited for PDA measurements.

Hereafter, the experimental results are plotted using symbols for comparison with numerical results. The cylindrical coordinate system (z, r, θ) is used to indicate axial (downward), radial and azymuthal directions. As no mean swirling motion was detected, only the axial and radial velocity components are provided. The mean components resulting from LES-averaging are respectively noted W and V whereas the RMS components are w_{rms} and v_{rms}. The symbols $\cdot_f$ and $\cdot_p$ denote the fluid and the particles. Section 6.2 deals with the simulations of the single-phase flow whereas results of two-phase flow simulations are analysed in Section 6.3.

6.2 Single-phase flow simulations

6.2.1 Computational domain

The total volume of the configuration is large, due to the length of both the ducts (2 m) and the chamber itself (1.5 m). In comparison, the combustion chamber of the Mercato test-rig schematised in Fig. 6.1 is 28 cm long and 13 cm wide. As a consequence, calculating the whole geometry would be computationaly expensive.

Since the location of the second stagnation point is known to mainly depend on the geometry global diameter, the diameters of the inner and annular pipes have been kept: $R_j = 10$ mm ; $R_1 = 75$ mm ; $R_2 = 150$ mm, but the length of the pipes has been shortened to 0.2 m or 0.1 m depending on the mesh considered (see Section 6.2.3), and the length of the chamber itself has been decreased from 1.5 m to 0.8 m. There are two main arguments for this: first, considering the low Reynolds number and the grid resolution in the inner pipe as well as the accuracy of the numerical scheme, it is impossible to wait for natural destabilisation of the gas flow. A specific inlet boundary condition is therefore used to help the flow destabilisation (see Section 6.2.2). Besides, the accurate prediction of particle motion in a pipe (or a channel) is still difficult to obtain, especially because of particle-wall interactions (Wang & Squires, 1996). The modified pipe length stays compatible with the particle relaxation and transit times presented in Section 6.1.2 has been accounted for. The second reason why shortening the length of the chamber is the location of the furthest stagnation point in the vicinity of $z = 400$ mm, that is to say far from the chamber outlet.

Finally, the volume of the computational domain has been divided by two, which drastically decreases the computational cost of LES.

6.2.2 Boundary conditions

Figure 6.7 shows the computational domain and the boundary conditions. The characteristic boundary conditions developed by Poinsot & Lele (1992*a*) are used for these simulations.

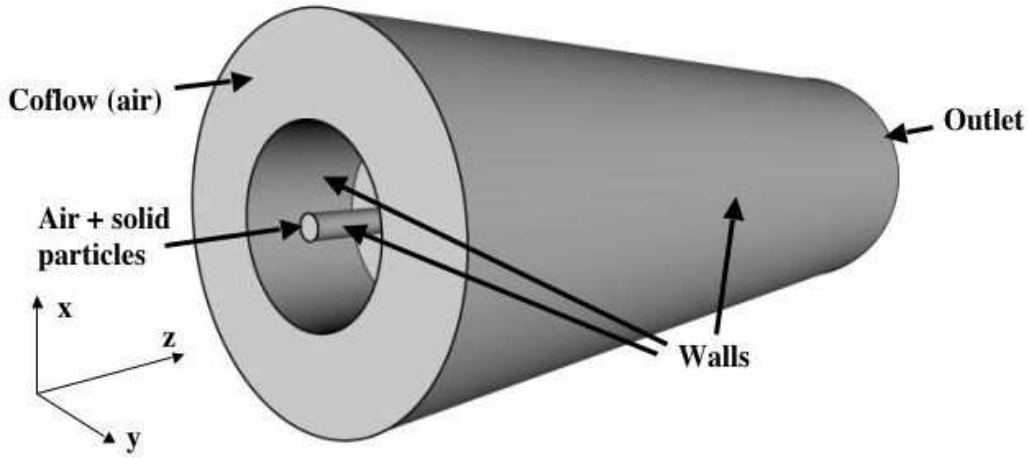

Figure 6.7 - *Computational domain. Configuration of Borée* et al. *(2001).*

The experimental profiles of mean and fluctuating fluid velocities are unknown at the inlet of the pipes, but they are available at the inlet of the test section: $z = 3\,mm$. Consequently, typical mean axial velocity profiles of fully-developed pipes are imposed at the inlet of the inner and annular pipes, corresponding to the experimental mass flux. This method leads to a good agreement between experimental and numerical mean velocity profiles at $z = 3\,mm$.
As already said, due to the low Reynolds numbers in the ducts, no destabilisation of the gas flow can be obtained without flow forcing. At the inlet of both pipes, the fluid velocity varies in time and space to reproduce the effect of an incoming turbulent field as observed in the experiment. The method in constructing the incoming turbulent signal is based on the Random Flow Generation (RFG) algorithm introduced in Section 5.2.2. Forcing the flow in such a way considerably accelerates the establishment of fully developed turbulent flows. It also ensures the presence of coherent perturbations not warranted with a pure white noise. Typical fluctuating profiles of fully-developed pipes are imposed at the inlet of the pipes and again, agreement between experimental and numerical fluctuating profiles are good at $z = 3mm$. The influence of this forcing is presented in Section 6.2.8.
The outlet is nearly non-reflective at atmospheric pressure, $P_f = 1.013\,10^5\,Pa$.
Wall numerical treatment depends on the grid resolution near the wall. When it is low, only wall modeling is accurate and the law-of-the-wall developed by Schmitt *et al.* (2007) is employed. Increase in resolution in the near-wall region allows the direct use of non-slipping walls. In all cases, the walls are isothermal at ambient temperature, $T_f = 293K$.

6.2.3 Characteristics of the grids

The impact of the grid type is investigated in Section 6.2.7. Table 6.4 details the characteristics of the three meshes tested, with names *bb_meshnst1*, *bb_meshnst2* and *bb_meshst*. Figures 6.8 and 6.9 display respectively longitudinal and front views of the three grid resolutions.

Name	**bb_meshnst1**	**bb_meshnst2**	**bb_meshst**
Grid type	Tetrahedra	Tetrahedra	Hexahedra
Number of nodes $(-)$	367313	549369	3255085
Number of cells $(-)$	2058883	3115898	3207960
Smallest cell volume $(.10^{-10}\ m^{-3})$	1.72	2.0	4.94
Length of the pipes (m)	0.2	0.1	0.1
Length of the chamber (m)	1.5	1.5	0.8
$\mathbf{y^+}$ **in the inner pipe** $(-)$	15	15	7.5
$\mathbf{y^+}$ **in the coflow** $(-)$	64	64	15
Time step (μs)	3.2	3.49	4.22

Table 6.4 - *Characteristics of the three meshes tested. Configuration of Borée et al. (2001).*

In the unstructured grids, special care has been taken to generate small cells in the recirculation zone and in the near-wall region. The non-dimensional wall distance y^+, varies from 15 in the inner jet from 64 in the annular jet. The main difference between the two unstructured grids is the resolution in the region $250 < z < 750$ *mm*, which considerably increases the number of nodes and cells. Besides, the length of the ducts have been shortened for *bb_meshnst2*, thanks to the use of the inlet forcing method mentionned in Section 6.2.2. Still, the resolution in the pipes is almost the same for both unstructured grids.

The main motivation for testing a structured grid on this configuration is the comparison with CDP that uses hexahedral cells. To make exact comparisons with both codes, the length of the test section was decreased down to 0.8 m. Although the number of cells is equivalent for *bb_meshnst2* and *bb_meshst*, it is important to remind that the total volume of both grids is really different. Furthermore, the differences in y^+ must be mentionned: the non-dimensional wall distance in the structured grid is twice smaller in the inner pipe and four times smaller in the coflow than in the two unstructured grids. Focusing on the resolution in the pipes, there are much more cells in the inner one as well as in the wall-region of the coflow. As expected, the smallest cell volume is all the same larger in the structured case, which increases the timestep.

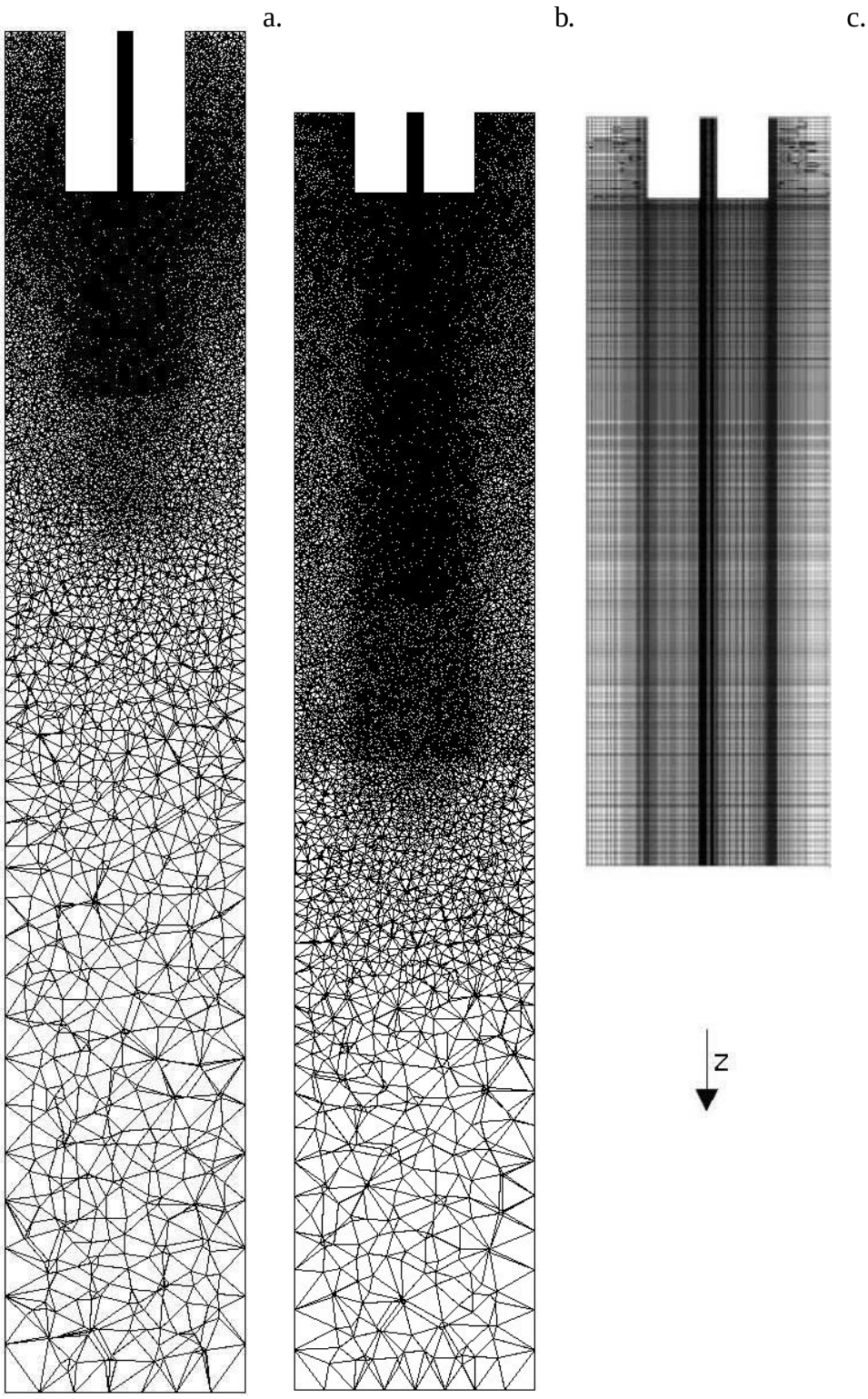

Figure 6.8 - *Longitudinal cutting plane ($x = 0$) of the three meshes tested: bb_meshnst1 (a.), bb_meshnst2 (b.), and bb_meshst (c.). Configuration of Borée et al. (2001).*

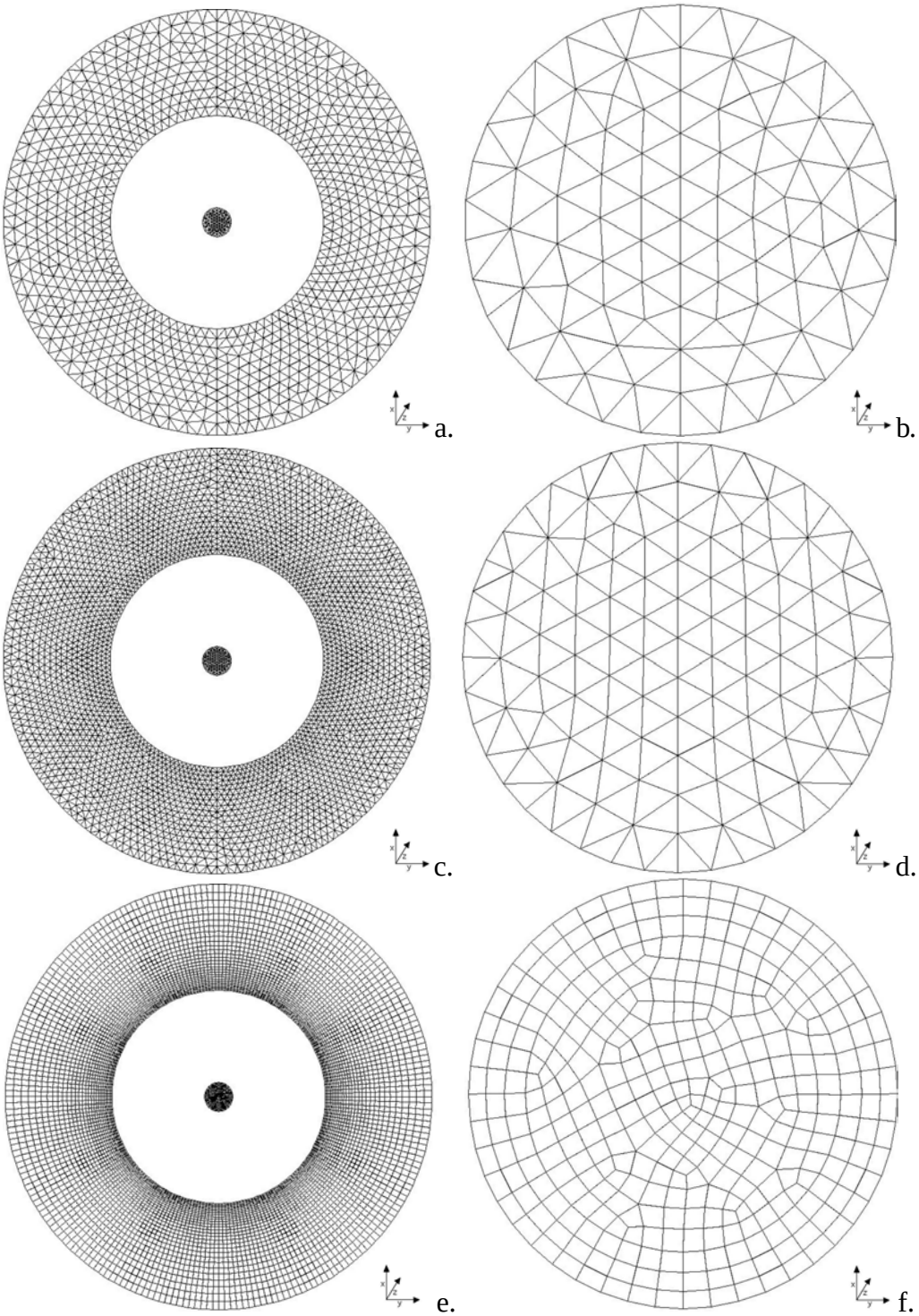

Figure 6.9 - *Global front view (left) and detail of the inner inlet (right) for the three meshes tested: bb_meshnst1 (a. & b.), bb_meshnst2 (c. & d.), and bb_meshst (e. & f.). Configuration of Borée et al. (2001).*

6.2.4 Test Cases

A series of test cases have been run, to investigate the following parameters:

- **the numerical scheme** (see Section 3.2): the TTGC scheme, 3^{rd} order accurate in space and time, is known to provide better results than the LW scheme, especially in recirculating flows.
- **the grid:** structured grids are rarely used to calculate swirled flows since they are said to generate preferential directions (Section 6.2.3). Their influence on recirculating but not swirling flows is tested here, as well as the grid resolution.
- **the subgrid-scale model:** the WALE model detailed in Section 4.2.1 is more suited to bounded flows than the Smagorinsky model. The resulting change in fluid turbulent viscosity profile in the near-wall region is analysed to show the influence on the global statistics.
- **the wall treatment:** it is linked to the subgrid-scale model. A law-of-the-wall model (Schmitt *et al.*, 2007) is used with the Smagorinsky subgrid model whereas the WALE model does not require any wall modeling.
- **the inlet boundary condition:** the RFG method detailed in Section 5.2.2 helps the flow destabilise in the pipes and ensures turbulent velocity profiles along the ducts.

Table 6.5 summarises the different cases performed for the gas flow.

Name	Mesh	Scheme	Turb. model	Wall model	Inlet BC
Nst1_lw_smago_lwm_norfg	*bb_meshnst1*	LW	Smagorinsky	Law-of-the-Wall	No RFG
Nst1_ttgc_smago_lwm_norfg	*bb_meshnst1*	TTGC	Smagorinsky	Law-of-the-Wall	No RFG
Nst1_ttgc_wale_wnm_norfg	*bb_meshnst1*	TTGC	WALE	None	No RFG
Nst1_ttgc_wale_wnm_rfgint	*bb_meshnst1*	TTGC	WALE	None	RFG Int.
Nst2_ttgc_wale_wnm_rfgint	*bb_meshnst2*	TTGC	WALE	None	RFG Int.
Nst2_ttgc_wale_wnm_rfgall	*bb_meshnst2*	TTGC	WALE	None	RFG All
St_ttgc_wale_wnm_rfgall	*bb_meshst*	TTGC	WALE	None	RFG All

Table 6.5 - *Test cases and corresponding parameters. Configuration of Borée* et al. *(2001).*

Results related to the various cases are presented hereafter. The gas LES solver of AVBP_TPF

is validated in Section 6.2.6 by direct comparison with CDP using the same structured grid, and experimental data. Then, in Section 6.2.7, the influence of the convective scheme and the grid are highlighted. These two elements are shown to be the most important parameters. Note that they are also the most CPU-time consumers. Finally, Section 6.2.8 focuses on the influence of the subgrid model coupled with the wall treatment, and the inlet boundary condition. Although these parameters make the calculations closer to the experimental flow, their effects on the flow statistics are less significant than the grid and the convective scheme.

As discussed in Section 4.3.2, the analysis of the averaged quantities resulting from LES requires a simulation time long enough to ensure convergence, and a sampling time small enough to ensure that the smallest structures can contribute to the averaged solution. In the present configuration, the lowest frequency to be represented is associated to the two counter-rotating structures on each side of the axis. Considering their size, $l_{f,l} \approx 0.08\,m$, and their mean rotating velocity, $U_{f,l} \approx 1\,m.s^{-1}$, the order of magnitude of the associated time is $\tau_{f,l} \approx 0.08\,s$. The most energetic eddies in the inner pipe consitute a reasonable choice to determine the highest frequencies. Considering their size, $l_{f,t} \approx 7\,mm$, and their velocity, $u'_{f,t} \approx 1.5 m.s^{-1}$, the order of magnitude of the associated time-scale is $\tau_{f,t} \approx 4.6\,ms$. All the cases presented in Table 6.5 have been run for $T_{av} \approx 0.5\,s$ and the time between two samples is $\Delta t_r \approx 1.2\,ms$. The statistics of the mean fields are then well converged. This is not always the case for the RMS quantities but the overall tendency gives sufficient information to compare the models.

6.2.5 Gas flow analysis

Figure 6.10 shows an instantaneous field of the gas velocity modulus in the cutting plane $y = 0$ for the case *St_ttgc_wale_wnm_rfgall*. A large amount of structures of different sizes are visible. The largest ones are linked to the diameter of the coflow, intermediate ones appear in the shear layers and structures coming out of the inner jet are also clearly identified.

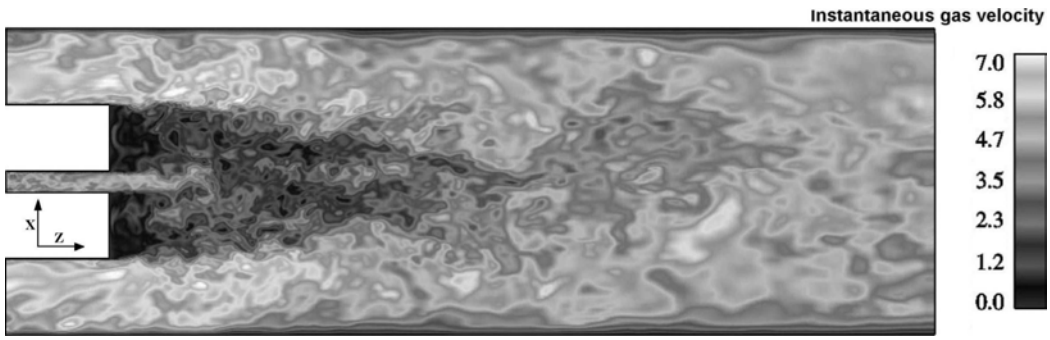

Figure 6.10 - *Topology of the gas flow. Instantaneous field of gas velocity modulus obtained with* AVBP_TPF *in the cutting plane* $y = 0$. *St_ttgc_wale_wnm_rfgall case. Configuration of Borée* et al. *(2001).*

The time-averaged field considerably differs from the instantaneous flow structure. Figures 6.11 a. – c. respectively present the mean field of gas axial velocity, and the RMS fields of gas axial and radial velocities in the cutting plane $y = 0$. The iso-contour line of zero mean axial velocity $W_f = 0$, is added on the three pictures. All fields are rather symmetric, which indicates good convergence of the simulations. As expected, there are two points with zero velocity along the axis, corresponding to distinct inner jet and coflow stagnation points. The peak of axial fluctuations is at the inner jet stagnation point whereas the radial fluctuations are maximum in the vicinity of the furthest stagnation point. Both axial and radial fluctuations show secondary peaks, respectively in the external shear layer and close to the first stagnation point. At these locations, turbulence is highly anisotropic.

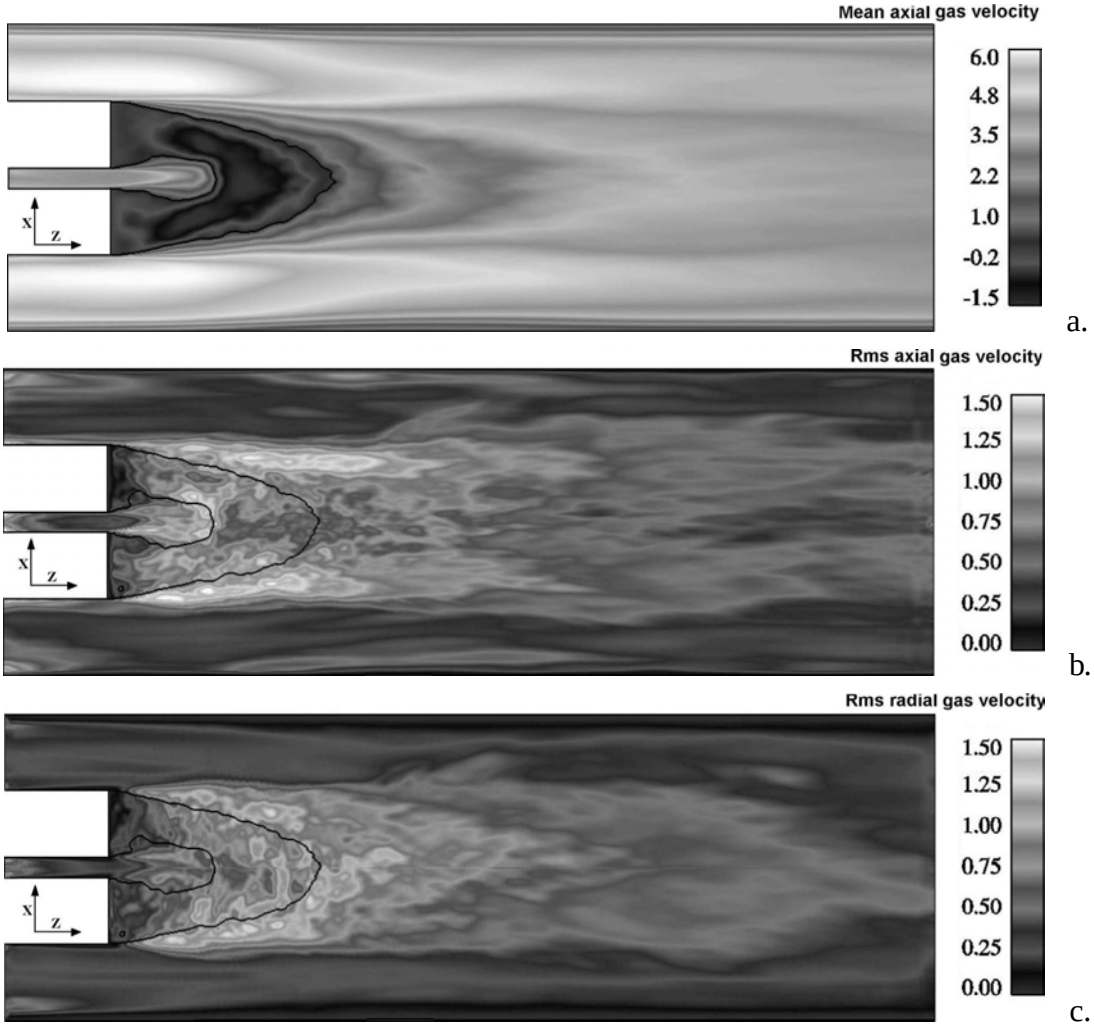

Figure 6.11 - *Topology of the gas flow. Mean field of gas axial velocity (a.). RMS fields of gas axial velocity (b.), and gas radial velocity (c.) obtained with* AVBP_TPF *in the cutting plane* $y = 0$. *The black line corresponds to the iso-contour line* $< W_f >= 0$. *St_ttgc_wale_wnm_rfgall case. Configuration of Borée* et al. *(2001).*

6.2.6 Validation of the gas LES solver from AVBP_TPF

The accuracy of the LES solver from AVBP_TPF for the gas phase is evaluated by computing the single-phase flow and comparing it to the data provided by Borée *et al.* (2001) and to the results of CDP. In this section, the case *St_ttgc_wale_wnm_rfgall* is analysed, not only because it provides the most accurate results but also because it is the best candidate for direct comparisons with CDP. Indeed, both codes use here the same structured grid. There are however some differences in the two codes, summarised in Table 6.6.

	CDP	**AVBP_TPF**
Time step (μs) / CFL $(-)$	147 / 50	4.2 / 0.7
Averaging time (s) / iterations $(-)$	2.65 / 18000	0.52 / 120000
Convective scheme	2^{nd} order that conserves kinetic energy (Ham & Iaccarino, 2004)	TTGC
LES model / Wall model	Dynamic Smagorinsky/None	WALE/None
Inner jet / Coflow Inlet BC	Forcing / No forcing	Forcing / Forcing

Table 6.6 - *Comparison of the parameters and models used for the single-phase flow LES performed with* CDP *and* AVBP_TPF *on the structured grid bb_meshst. Configuration of Borée* et al. *(2001).*

As already mentioned, CDP resolves implicitly the incompressible Navier-Stokes equations whereas AVBP_TPF resolves explicitely the compressible Navier-Stokes equations. The main consequence is that the time step is 35 times larger for CDP, leading to consequent differences in the computational cost of such a calculation. As a result, the total averaging time is smaller for AVBP_TPF, but the convergence has been ensured to be good enough. Another noticeable difference comes from the treatment of the inlet boundary condition in the coflow. No turbulence has been injected on the gas flow in the outer duct in the case of CDP whereas the RFG method described in Section 6.2.2 has been used for both injection ducts with AVBP_TPF.

Before analysing the statistics in terms of mean and RMS velocities, it is useful to evaluate the LES criterion defined in Section 4.3.3. This is done in Fig. 6.12. The location of the iso-contour line $Q_f^{LES} = 0.8$ shows that the LES is rather well-resolved in the domain, especially close to the centerline and in the coflow shear layers. The quality is poorer in the coflow outer region and in the central jet. However, the increase in resolution in this region would decrease the time-step.

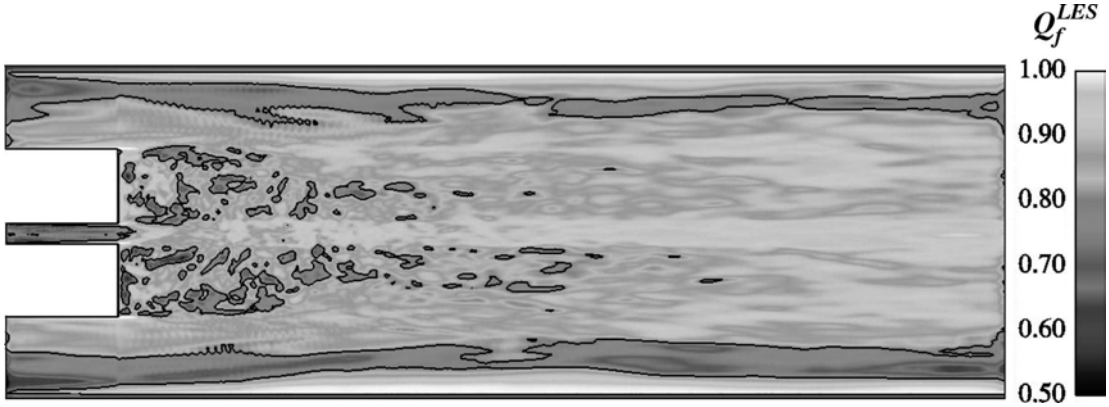

Figure 6.12 - *Mean field of LES criterion given by Eq. (4.40) for the gas phase in the cutting plane $y = 0$. The black line stands for the iso-contour line $Q_f^{LES} = 0.8$. St_ttgc_wale_wnm_rfgall case. Configuration of Borée et al. (2001).*

Figure 6.13 displays mean and RMS gas axial velocities along the axis, and Figs 6.14 – 6.17 present the radial profiles for the two codes along with the experimental measurements. The global agreement between the two codes and experiments is very good and most of the flow physics is captured by the two LES solvers. The width and the length of the recirculation zone are well predicted (Fig. 6.14). Differences between both codes in predicting the location of the two stagnation points (Fig. 6.13 a.) are minor. This point is known to be the main difficulty when calculating bluff body flows and the sensitivity to the parameters is shown in the following sections. The two LES solvers capture the mean radial component correctly, except at the end of the recirculation zone. The mean radial velocity level remains small (less than 1 $m.s^{-1}$ in Fig. 6.15) compared to the mean axial velocity level. Focusing on the RMS velocities (Fig. 6.16 and 6.17), the agreement with measurements is also good. The location and the amplitude of the peaks are well predicted, except in the coflow where CDP underpredicts both the radial and axial RMS velocities. The origin of the discrepancy is the treatment of the coflow inlet boundary condition, with no turbulence injected with CDP in the outer duct. Section 6.2.8 underlies the influence of this inlet boundary condition.

The overall result is that both codes provide very similar results, also close to the measurements, even though they use different methods. This indicates that the accuracy of the gas LES solver of AVBP_TPF is sufficiently good to test the dispersed phase with reasonable confidence on this configuration. Nevertheless, it must be underlined that the results are greatly sensitive to the numerical parameters and the grid used.This is developed in Sections 6.2.7 and 6.2.8.

For the sake of clarity, only the most informative graphs are discussed hereafter, but all the radial and axial profiles are available, and provided in Appendix A.

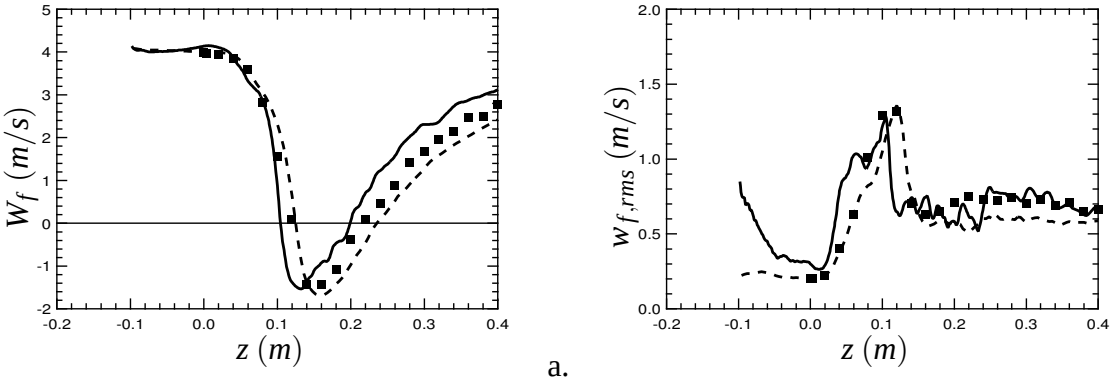

a. b.

Figure 6.13 - **Code influence.** *Axial profiles of mean (a.), and RMS (b.), axial gas velocity. Symbols: experiment – Dotted-dashed line: CDP – Solid line: AVBP_TPF/St_ttgc_wale_wnm_rfgall.*

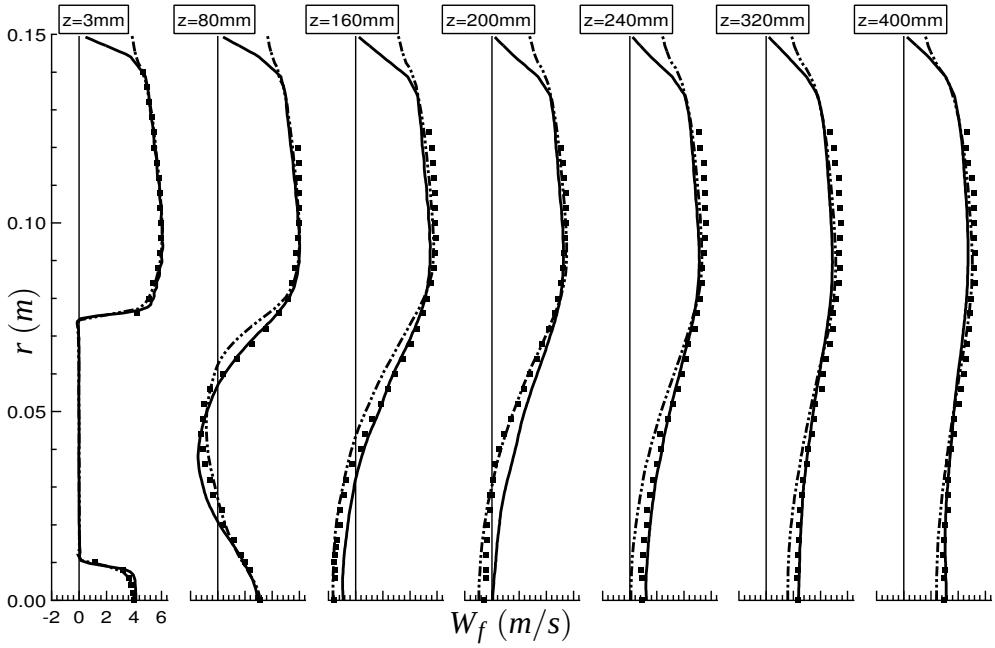

Figure 6.14 - **Code influence.** *Radial profiles of mean axial gas velocity at 7 stations along z axis. Symbols: experiment – Dotted-dashed line: CDP – Solid line: AVBP_TPF/St_ttgc_wale_wnm_rfgall.*

6.2.7 Influence of the numerical scheme and the grid

The numerical scheme is critical when performing LES as well as the grid quality. Whether results are more accurate with a low-order scheme used on a refined grid or with a high-order scheme coupled with a coarser grid is still an open question (Sengissen *et al.*, 2005). While Colin & Rudgyard (2000) and Vreman (1995) for example aim at developping high-order schemes on coarse grids, other authors use little dissipative 2^{nd} order schemes on more

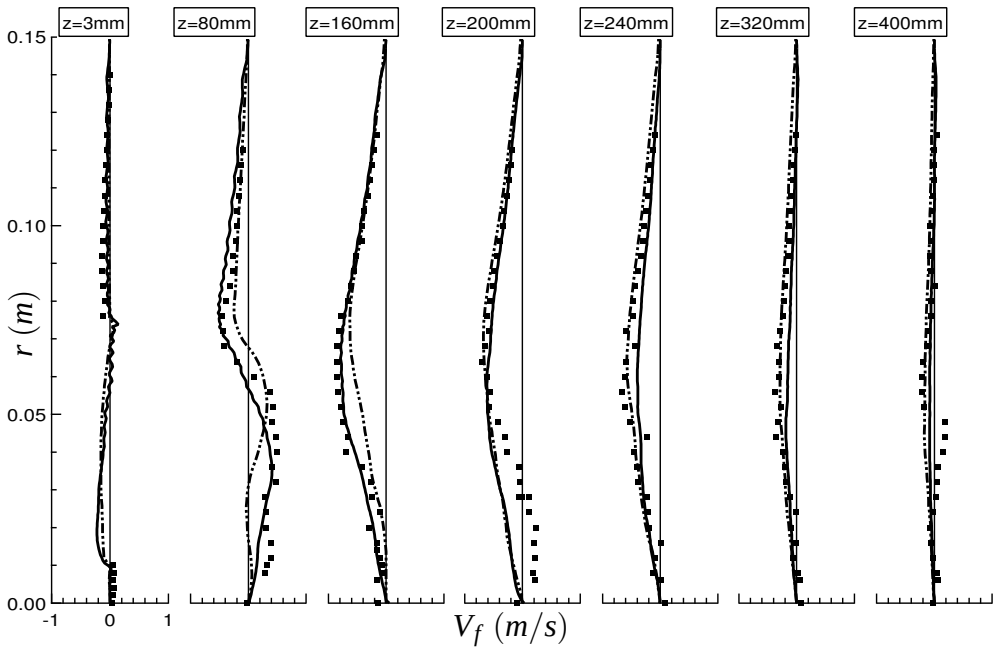

Figure 6.15 - **Code influence.** *Radial profiles of mean radial gas velocity at 7 stations along z axis. Symbols: experiment – Dotted-dashed line: CDP – Solid line: AVBP_TPF/St_ttgc_wale_wnm_rfgall.*

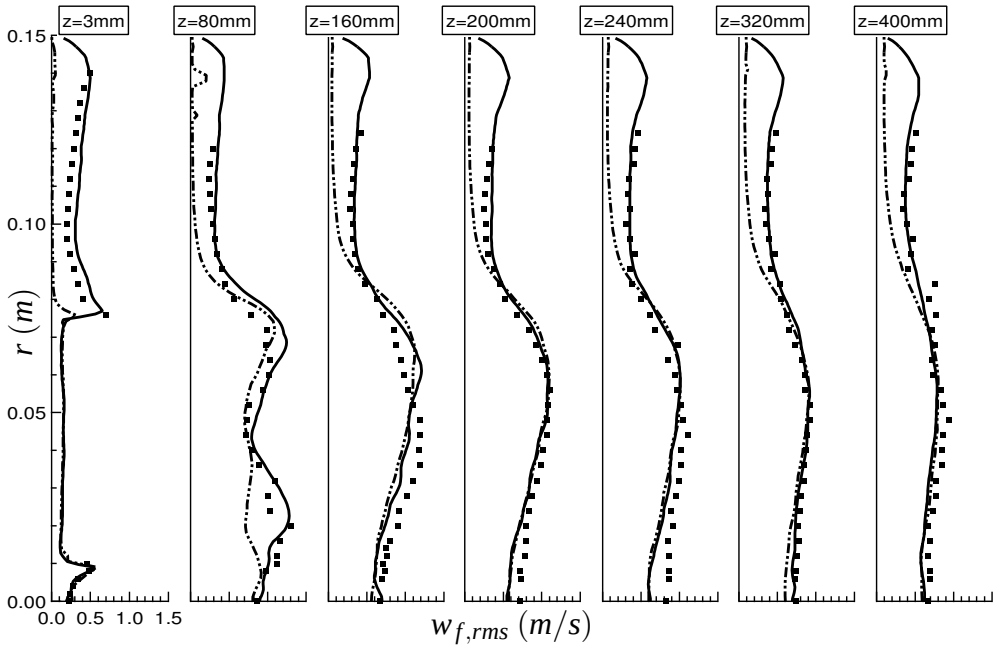

Figure 6.16 - **Code influence.** *Radial profiles of RMS axial gas velocity at 7 stations along z axis. Symbols: experiment – Dotted-dashed line: CDP – Solid line: AVBP_TPF/St_ttgc_wale_wnm_rfgall.*

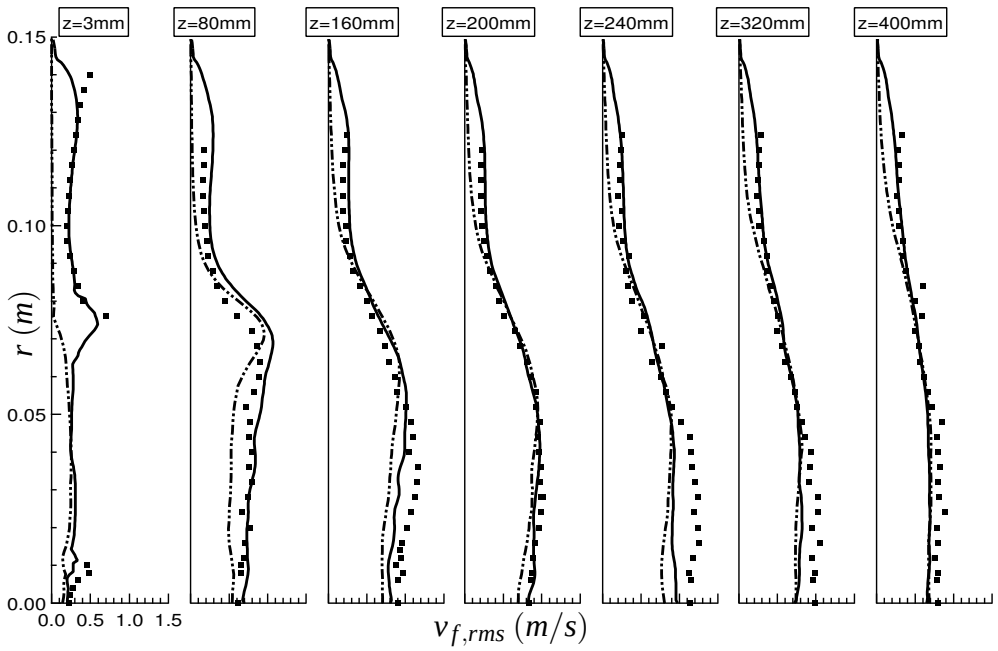

Figure 6.17 - **Code influence.** *Radial profiles of RMS radial gas velocity at 7 stations along z axis. Symbols: experiment – Dotted-dashed line: CDP – Solid line: AVBP_TPF/St_ttgc_wale_wnm_rfgall.*

refined grids (Jimenez & Moin, 1991; Mahesh *et al.*, 2004). Naturally, the computational cost of the simulation is a key point for the final choice.
In the following, the results obtained with the LW and TTGC schemes are compared and differences in the flow topology as well as in the mean and RMS profiles are highlighted. For this first test, the coarsest unstructured grid *bb_meshnst1* is used. In a second step, only the TTGC scheme is kept to study the influence of both the grid resolution and the grid type on the prediction of the stagnation point location.

• INFLUENCE OF THE CONVECTIVE SCHEME

To evaluate the influence of the numerical schemes on the single-phase flow results, the cases *Nst1_lw_smago_lwm_norfg* and *Nst1_ttgc_smago_lwm_norfg* (see Table 6.5) are compared. Both computations carried out with the coarsest grid *bb_meshnst1*, use the subgrid Smagorinsky model associated with the law-of-the-wall model. Moreover, the RFG method is not used at the inlet of the ducts so that the only difference between the two cases is the numerical scheme.

The qualitative impact of the scheme order of accuracy on the small structures is clear on Fig. 6.18 where instantaneous iso-surfaces of Q-criterion introduced in Section 5.3.2 are displayed for both schemes. Both fields exhibit two kinds of coherent structures: some longitu-

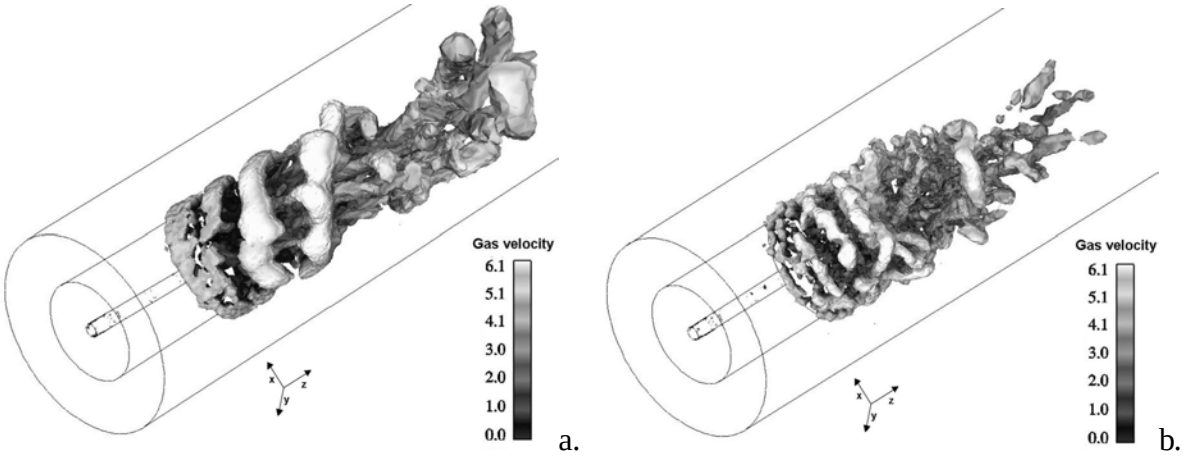

Figure 6.18 - **Convective scheme influence.** *Instantaneous iso-surfaces of Q-criterion for the cases Nst1_lw_smago_lwm_norfg (a.), and Nst1_ttgc_smago_lwm_norfg (b.). The iso-surfaces are colored by instantaneous velocity. Configuration of Borée* et al. *(2001).*

dinal vortices come from the inner pipe wheras other are created in the external shear zone and are rather azimuthal. However, the structures created with the TTGC scheme are more detailed and more numerous.

The axial profiles of mean and RMS axial velocities plotted in Fig. 6.19 quantify this observation. When using LW, the zero mean axial velocity iso-contour line that delimits the recirculation zone is located too far downstream of the ducts. Besides, as shown in Fig. 6.20, the LW scehme under-estimates the axial fluctuating velocities at the outlet of the jets. This is also the case for the radial fluctuations.

This leads to the conclusion that two-phase flows must be computed with the TTGC scheme. Indeed, the particle distribution as well as the flame shape in bluff body flows is known to be mainly linked to the first stagnation point. It is however important to keep in mind that the computational cost of a simulation using TTGC is 2.5 bigger than using LW.

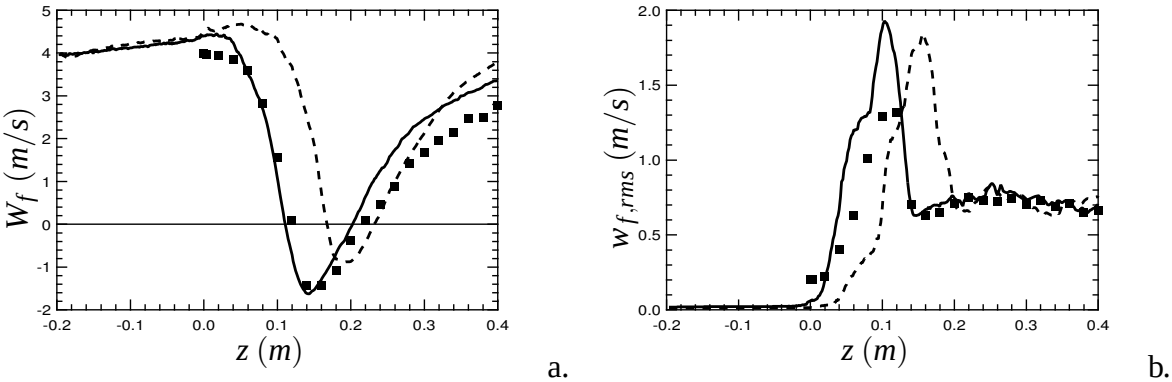

Figure 6.19 - **Convective scheme influence.** *Axial profiles of mean (a.), and RMS (b.), axial gas velocity. Symbols: experiment – Dashed line: Nst1_lw_smago_lwm_norfg – Solid line: Nst1_ttgc_smago_lwm_norfg.*

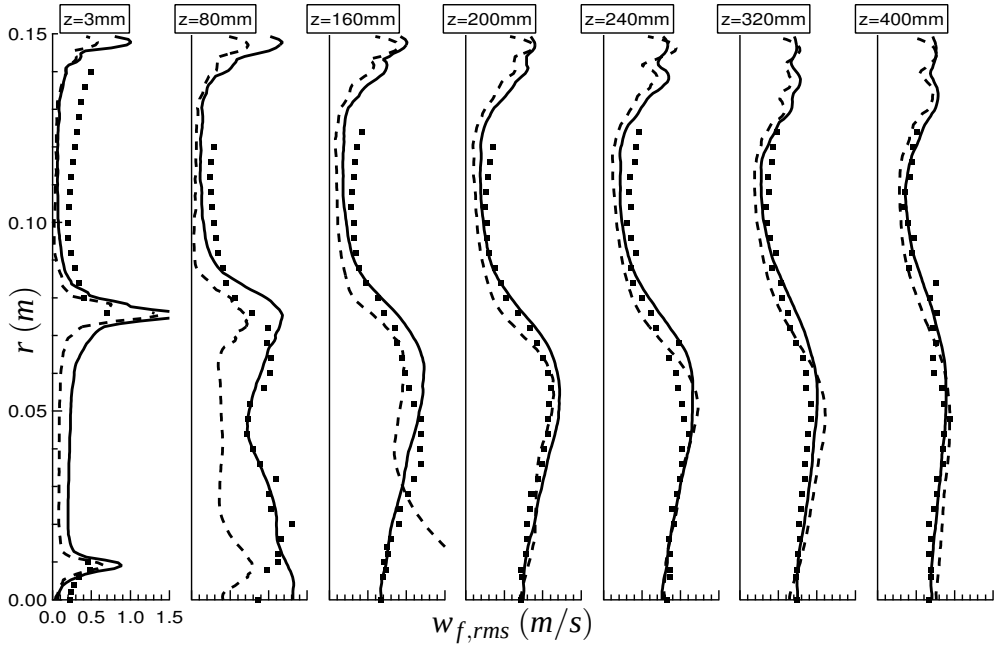

Figure 6.20 - **Convective scheme influence.** *Radial profiles of RMS axial gas velocity at 7 stations along z axis. Symbols: experiment – Dashed line: Nst1_lw_smago_lwm_norfg – Solid line: Nst1_ttgc_smago_lwm_norfg.*

• **INFLUENCE OF THE GRID**

The simulations are all performed here with the TTGC scheme, the WALE subgrid model associated with no-wall modeling, and the RFG method. The influence of the grid is investigated in two steps.
First, the cases *Nst1_ttgc_wale_wnm_rfgint* and *Nst2_ttgc_wale_wnm_rfgint* (see Table 6.5) are compared to show the impact of the grid resolution. The unstructured grids *bb_meshnst1* and *bb_meshnst2* are respectively used (see Table 6.4).
Second, the cases *Nst2_ttgc_wale_wnm_rfgall* and *St_ttgc_wale_wnm_rfgall* are focused on to show the impact of the grid type. The unstructured grid *bb_meshnst2* and the structured one *bb_meshst* are respectively used.

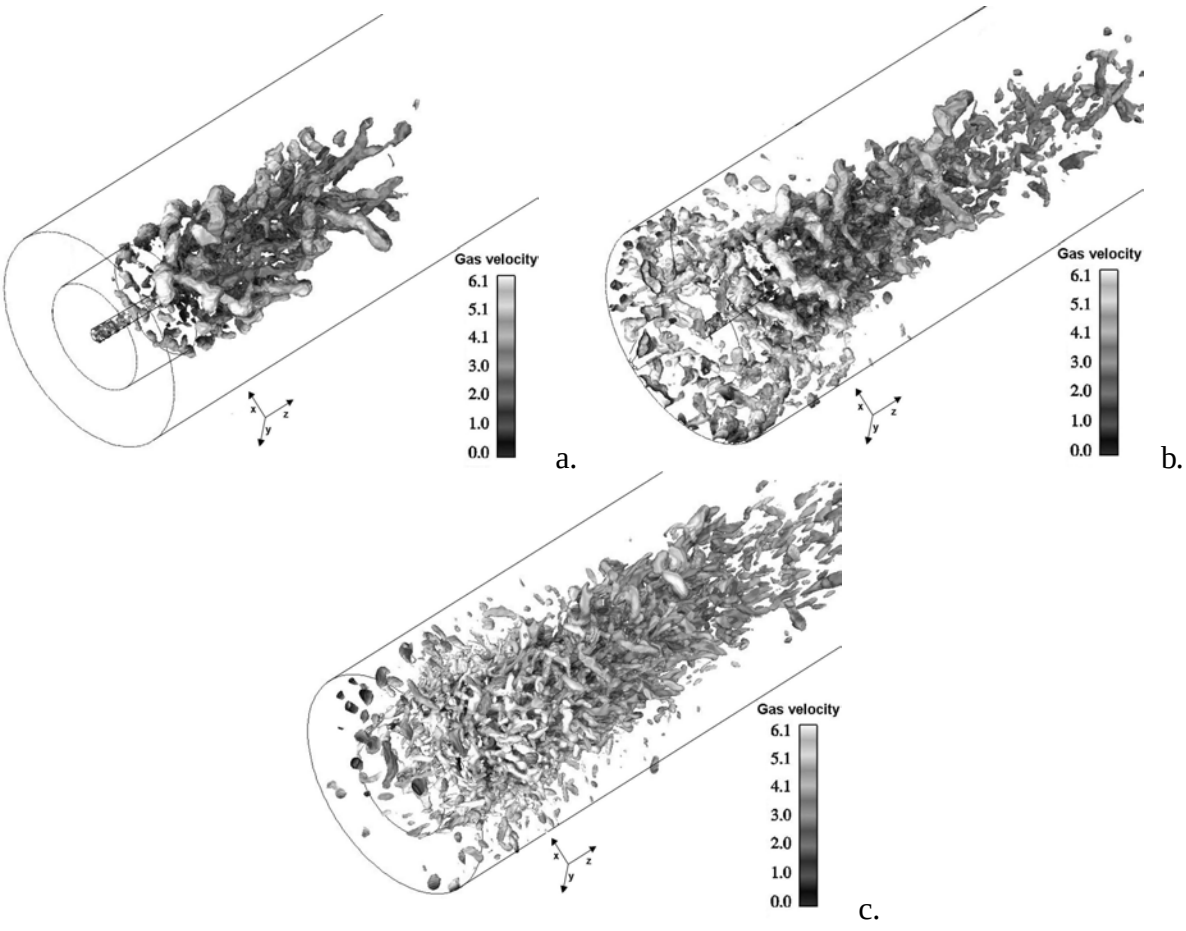

Figure 6.21 - **Grid influence.** *Instantaneous iso-surfaces of Q-criterion for the cases Nst1_ttgc_wale_wnm_rfgint (a.), Nst2_ttgc_wale_wnm_rfgint (b.), and St_ttgc_wale_wnm_rfgall (c.). The iso-surfaces are colored by instantaneous velocity. Configuration of Borée* et al. *(2001).*

The visualisation of the instantaneous iso-surfaces of the Q-criterion for the three cases *Nst1_ttgc_wale_wnm_rfgint*, *Nst2_ttgc_wale_wnm_rfgint* and *St_ttgc_wale_wnm_rfgall* is shown in Fig. 6.21. Note that because the RFG method is not used in the coflow for the case *Nst1_ttgc_wale_wnm_rfgint* only, no coherent structures are visible in the coflow in Fig. 6.21 a. Apart from this, the main difference in flow structure between the two unstructured grids is the location of the vortices, more extended in the case *Nst2_ttgc_wale_wnm_rfgall*. This is obviously due to the mesh refinement operated in the second quarter of the chamber in *bb_meshnst2*. The finest unstructured grid and the structured grid can be directly compared in Figs. 6.21 b. and c. The major difference is the size of the most visible coherent structures that are much smaller on the structured grid. In other words, both grids resolve large vortices in the same way but the structured grid allows the resolution of smaller vortices.

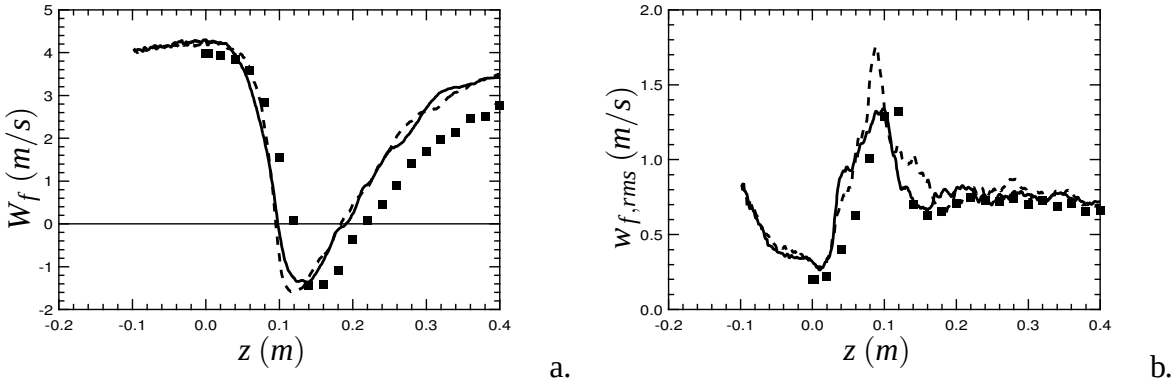

a. b.

Figure 6.22 - **Grid influence.** *Axial profiles of mean (a.), and RMS (b.), axial gas velocity. Symbols: experiment – Dashed line: Nst1_ttgc_wale_wnm_rfgint – Solid line: Nst2_ttgc_wale_wnm_rfgint.*

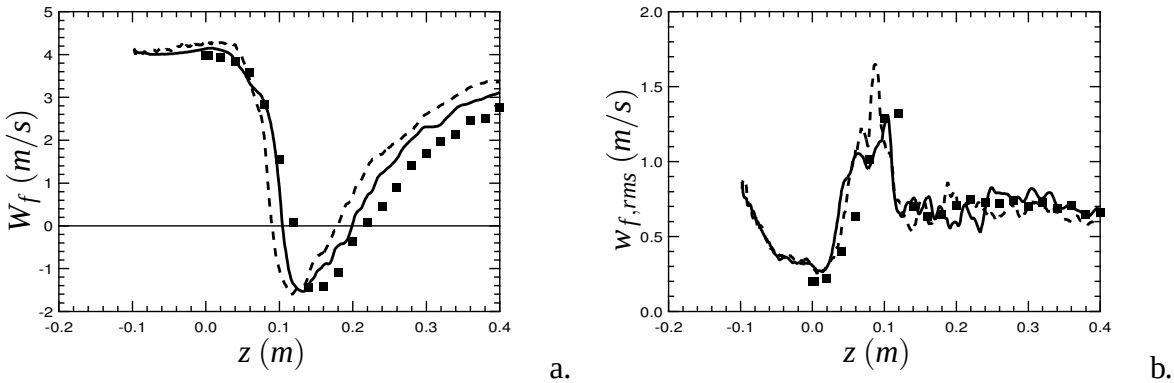

a. b.

Figure 6.23 - **Grid influence.** *Axial profiles of mean (a.), and RMS (b.), axial gas velocity. Symbols: experiment – Dashed line: Nst2_ttgc_wale_wnm_rfgall– Solid line: St_ttgc_wale_wnm_rfgall.*

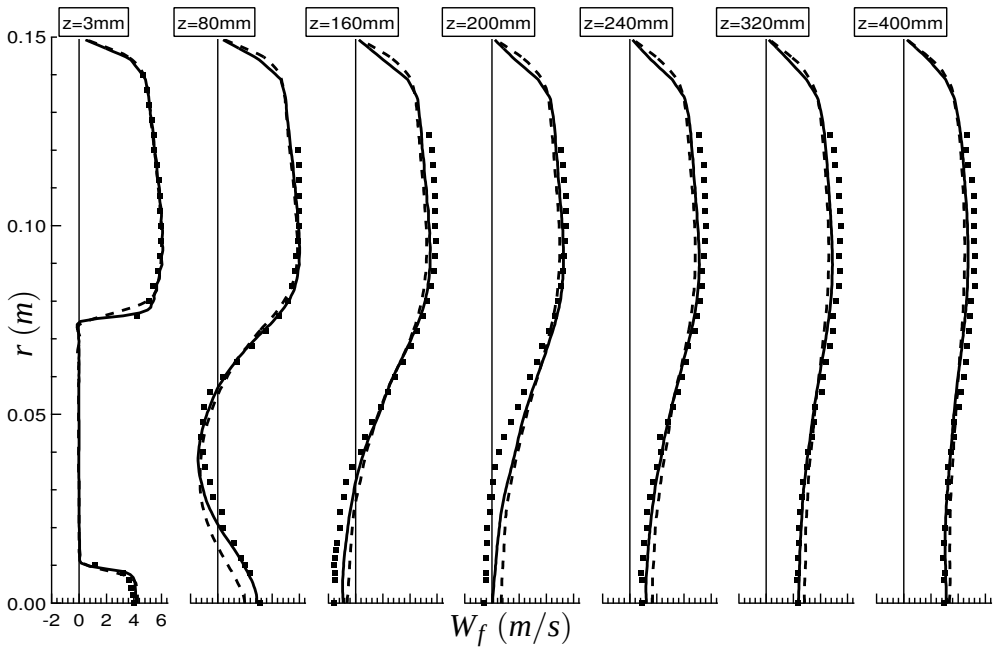

Figure 6.24 - **Grid influence.** *Radial profiles of mean axial gas velocity at 7 stations along z axis. Symbols: experiment – Dashed line: Nst2_ttgc_wale_wnm_rfgall– Solid line: St_ttgc_wale_wnm_rfgall.*

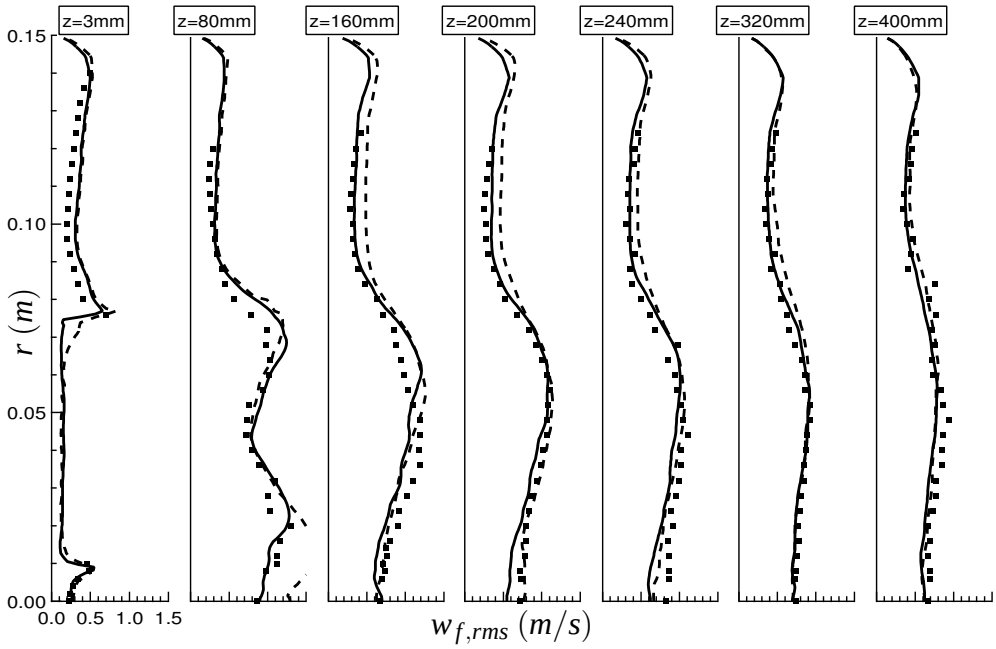

Figure 6.25 - **Grid influence.** *Radial profiles of RMS axial gas velocity at 7 stations along z axis. Symbols: experiment – Dashed line: Nst2_ttgc_wale_wnm_rfgall– Solid line: St_ttgc_wale_wnm_rfgall.*

These observable differences do not appear so clearly on the axial mean and RMS axial velocity profiles, plotted in Fig. 6.22. This also holds for the radial profiles presented in Appendix A. Figure 6.23 compares the same quantities for the finest unstructured grid and the structured one. The location of the peak of RMS axial velocity is well predicted with the two grids but its amplitude is closer to the measurements using the structured grid. The impact of the structured grid on the mean axial velocity is even clearer: the inner jet flow penetrates a little bit farther in the chamber, which improves the prediction of the location of the two stagnation points. When looking at the radial profiles of mean and RMS axial velocities in Figs. 6.24 and 6.25, the most significant change is at the station $z = 80$ *mm*. At this point, the mean and RMS axial velocities are respectively under and over-estimated with the unstructured grid.

Accounting for the cost efficiency slightly modifies the previous conclusions. Table 6.7 compares the computational cost of the three different meshes when simulating 0.1 *s* physical time with otherwise the same parameters. Using the coarsest unstructured grid *bb_meshnst1* is about five times cheaper than performing the simulations on the structured grid *bb_meshst*. This figure is to be related to the gain in quality of the predictions choosing the final configuration and grid.

Name	**bb_meshnst1**	**bb_meshnst2**	**bb_meshst**
Total CPU time (s)	44604	68460	235823
Efficiency / iteration / node (μs)	3.88	4.35	3.06
Efficiency / iteration / cell (μs)	0.69	0.77	3.10

Table 6.7 - **Grid influence.** *Code efficiency for single-phase flow calculations depending on the mesh. Statistics given for* 0.1 *s (physical time) computed with TTGC on 16 processors on a CRAY XD1 machine. Configuration of Borée* et al. *(2001).*

6.2.8 Influence of wall treatment, LES model and inlet boundary conditions

In addition to the numerical scheme and the grid that mainly influence the results, predictions can be improved using appropriate subgrid models (depending on the resolution in the near-wall region) and more realistic boundary conditions. Hereafter, the WALE subgrid model associated with no-wall modeling is compared to the Smagorinsky subgrid model associated with the law-of-the-wall model (Schmitt *et al.*, 2007). The use of turbulent forcing at the inlet of the ducts is also tested. Note that in contrary to the impact of the convective scheme or the on the cost efficiency, these minor modifications do not increase the CPU.

• INFLUENCE OF THE GASEOUS LES MODEL AND THE WALL TREATMENT

In turbulent bounded flows, all turbulent fluctuations are damped near the walls, so that the fluid turbulent viscosity $\nu_{f,t}$ (see Chapter 2), should go to zero at the wall. This is not the case when using the subgrid Smagorinsky model that gives a non-zero value of $\nu_{f,t}$ where velocity gradients exist. This is the main reason why Ducros *et al.* (1998*b*) developed the WALE subrid model that naturally predicts a zero value of fluid turbulent viscosity at the wall, whatever the geometry considered. As a consequence, the mean velocity profile is expected to be in better agreement with the measurements. In AVBP_TPF, both models are available and adequate wall treatments are then required depending on the resolution:

- When the resolution in the near-wall region is low, the use of the law-of-the-wall model (Schmitt *et al.*, 2007) associated with the Smagorinsky subgrid model is recommended. In this case, the recommended distance to the wall is $y^+ \in [50-500]$. On the other hand, when the grid in refined at the walls ($y^+ < 8$), no specific wall treatment is required and the WALE model is then more suited. For the sake of simplicity, hereafter, the denomination of the Smagorinsky subgrid model associated with the law-of-the-wall treatment is shortened to the Smagorinsky model. Similarly the WALE model refers to the WALE subgrid model without wall modeling.
- The characteristics of the coarsest unstructured grid, *bb_meshnst1* (see Table 6.4) allow to test the influence of the two combinations. The corresponding cases are *Nst1_ttgc_smago_lwm_norfg* and *Nst1_ttgc_wale_wnm_norfg* detailed in Table 6.5. In these simulations, the TTGC scheme is used and no turbulent forcing is imposed at the inlet of the pipes.

Figure 6.26 displays the mean fields of non-dimensional fluid turbulent viscosity in the cutting plane $y = 0$ for the two cases. As expected, results differ most in the vicinity of the walls where the fluid turbulent viscosity goes to zero only with the WALE model. The behavior of the two

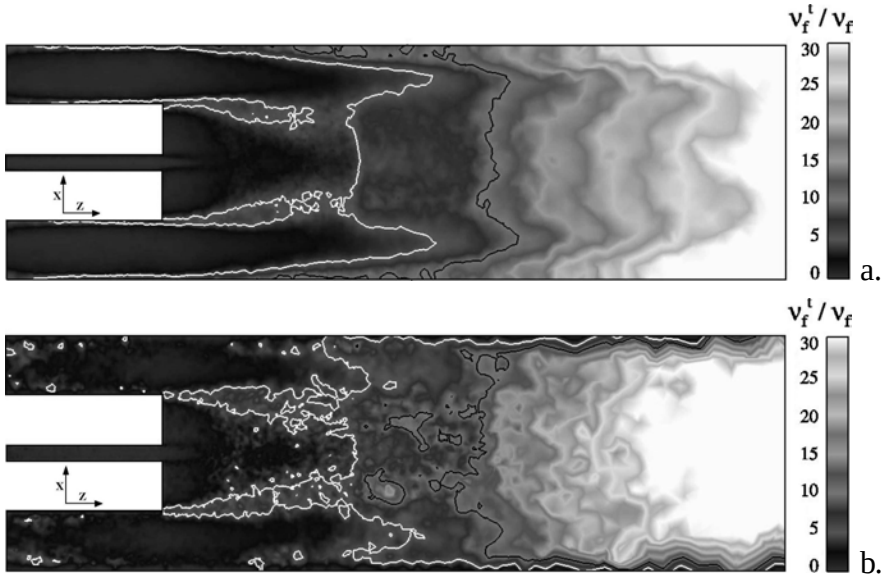

Figure 6.26 - **LES and wall modeling influence.** *Mean field of non-dimension turbulent viscosity for Nst1_ttgc_smago_lwm_norfg (a.), and Nst1_ttgc_wale_wnm_norfg (b.) in the cutting plane $y = 0$. The white and black lines respectively stand for $\nu_f^t/\nu_f = 5$ and $\nu_f^t/\nu_f = 10$. Configuration of Borée et al. (2001).*

models in the rest of the chamber is very similar. The impact on the velocity field is restricted to the near-wall region, as shown in Figs. 6.27 and 6.28. The mean axial velocity decreases to zero at the wall of the coflow and a slight increase in the RMS axial velocity is visible in the same zone when the WALE model is employed.

Figure 6.29 focuses on the radial profiles of turbulent viscosity and RMS axial velocities in the ducts themselves. The conclusion slightly differs. Both quantities are compared at four stations in the ducts: $z = -200$ *mm* ; $z = -150$ *mm* ; $z = -100$ *mm* and $z = -50$ *mm*, where the first one corresponds to the inlet of the inner and coflow pipes. There, the axial velocity fluctuations naturally develop in the duct when using the WALE model, which is not the case with the Smagorinsky model. As a consequence, the turbulent viscosity field generated by the Smagorinsky model (see Fig. 6.29 a.) is lower than with the WALE model (see Fig. 6.29 b.), except at the wall where the behaviour is non-physical. As a result, the WALE subgrid model without specific treatment at the wall should be preferred to the Smagorinsky model associated with the law-of-the-wall in our case.

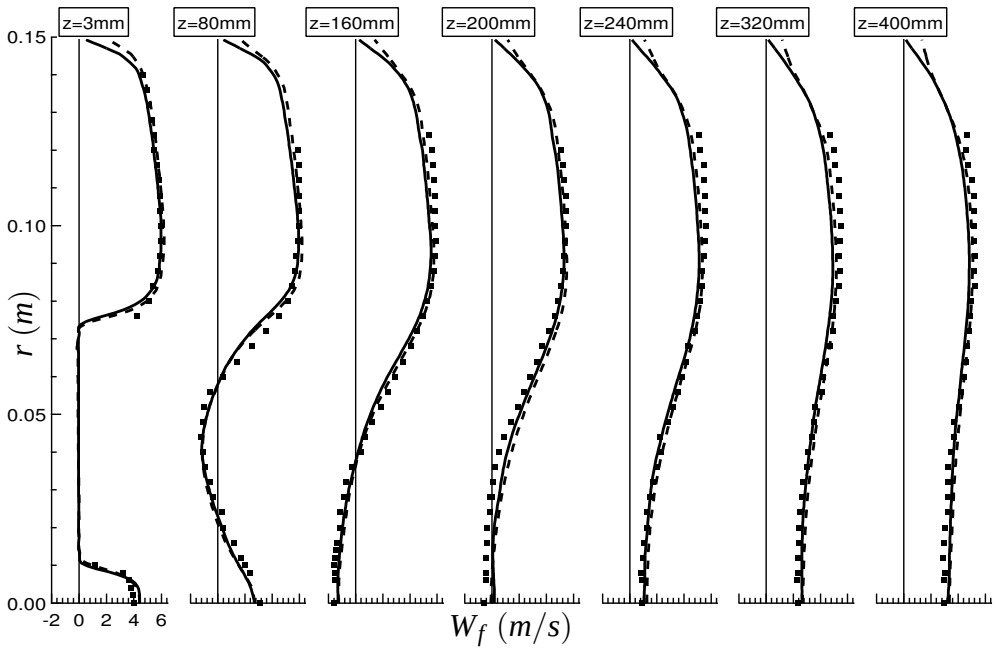

Figure 6.27 - **LES and wall modeling influence.** *Radial profiles of mean axial gas velocity at 7 stations along z axis. Symbols: experiment – Dashed line: Nst1_ttgc_smago_lwm_norfg – Solid line: Nst1_ttgc_wale_wnm_norfg.*

• **INFLUENCE OF THE INLET TURBULENT FORCING**

When only a typical mean axial velocity profile of fully-developed pipe is imposed at the inlet of both the inner and the coflow pipes, relaminarisation of the mean velocity profile is expected. This is mainly due to the unsufficient grid resolution, the unsufficient length of the ducts and the dissipation of the numerical scheme. The impact of the RFG method (see Section 6.2.2) on the mean and RMS velocity profiles is investigated hereafter.

– Inner pipe turbulent forcing

The influence of the inlet turbulent forcing method is investigated by comparing the cases *Nst1_ttgc_wale_wnm_norfg* and *Nst1_ttgc_wale_wnm_rfgint* described in Table 6.5. The axial profiles of mean and RMS axial velocities displayed in Fig. 6.30 show clearly the influence of the inlet boundary condition treatment. Focusing on the velocity fluctuations, they are shown to decrease in the central pipe due to a lack of resolution. Yet, the numerical value of $w_{f,rms}$ at the outlet of the duct is in good agreement with the experimental value. The consequence of this fluid agitation in the duct itself is a flat mean axial velocity profile in the pipe. Thus, the maximum of mean axial velocity is in better agreement with the experiments at the outlet of the duct ($z = 3\ mm$). Note that in Fig. 6.30 a., the accurate prediction of the location of the

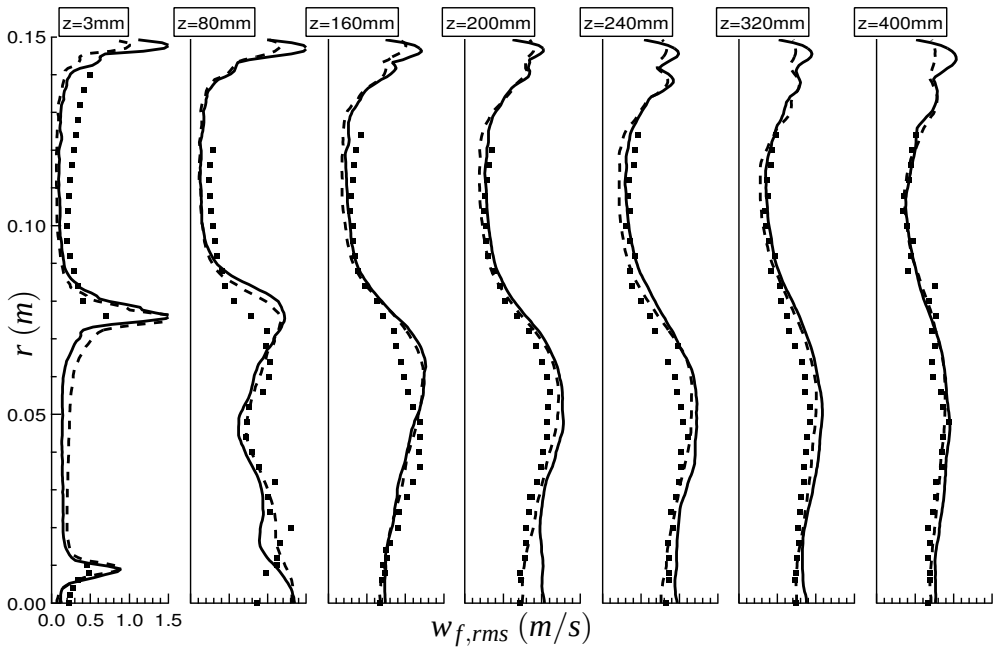

Figure 6.28 - **LES and wall modeling influence.** *Radial profiles of RMS axial gas velocity at 7 stations along z axis. Symbols: experiment – Dashed line: Nst1_ttgc_smago_lwm_norfg – Solid line: Nst1_ttgc_wale_wnm_norfg.*

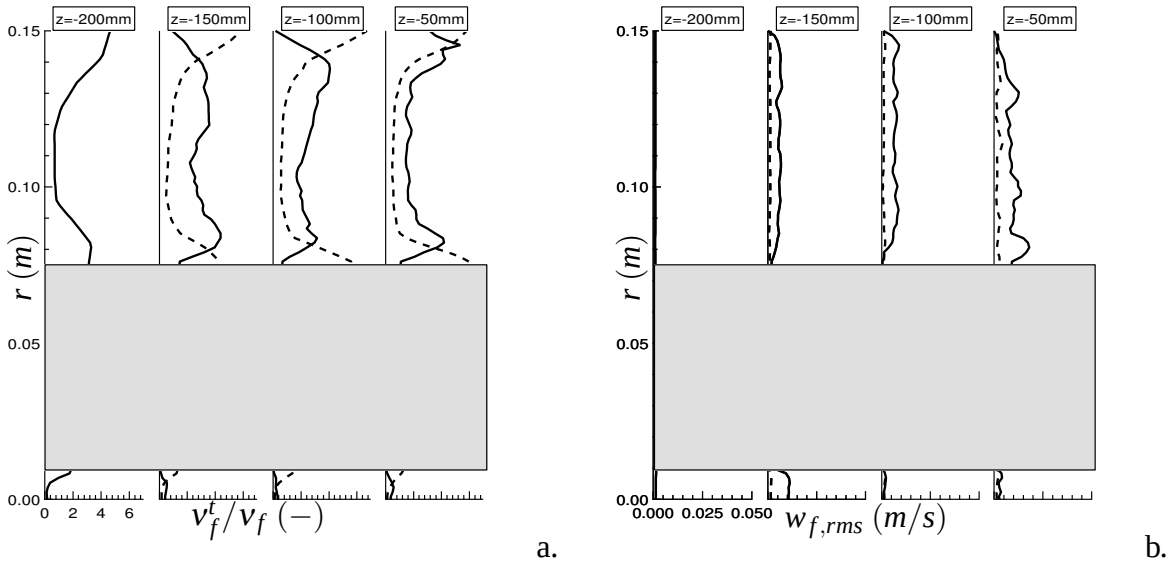

Figure 6.29 - **LES and wall modeling influence.** *Radial profiles of mean non-dimension turbulent viscosity (a.), and RMS axial gas velocity (b.) at 4 stations in the pipes along z axis. Dashed line: Nst1_ttgc_smago_lwm_norfg – Solid line: Nst1_ttgc_wale_wnm_norfg.*

recirculation zone for the case *Nst1_ttgc_wale_wnm_norfg* is only due to exact compensation of errors that is completely fortuitous.

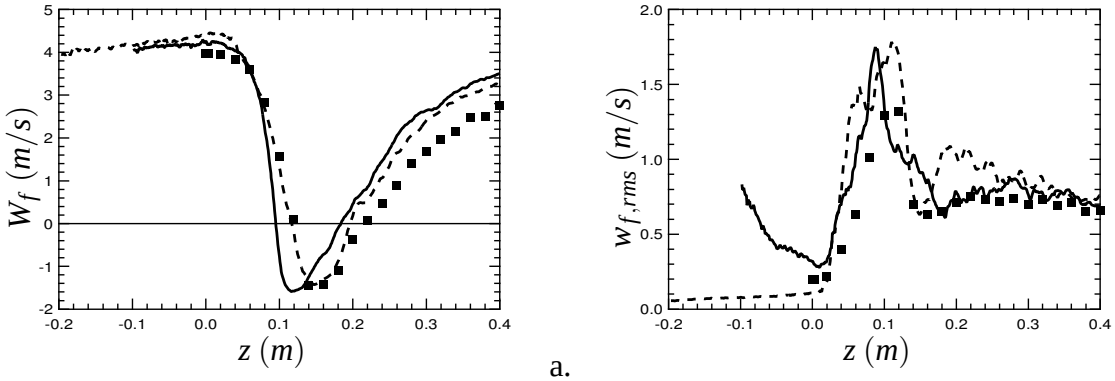

a. b.

Figure 6.30 - **Inner pipe turbulent forcing influence.** *Axial profiles of mean (a.), and RMS (b.), axial gas velocity. Symbols: experiment – Dashed line: Nst1_ttgc_wale_wnm_norfg – Solid line: Nst1_ttgc_wale_wnm_rfgint.*

– Coflow turbulent forcing

The influence of the outer inlet boundary condition is less crucial in terms of jet penetration and recirculation zone, and so, for the prediction of particle dispersion. Its impact was checked by comparing the cases *Nst2_ttgc_wale_wnm_rfgint* and *Nst2_ttgc_wale_wnm_rfgall*. The finest unstructured grid is used, associated with TTGC, the WALE model and no wall modeling. Inlet forcing is used in the central duct for both cases.
Injecting turbulence in the coflow still slightly modifies the mean axial velocity profile in the near wall region (see Fig. 6.31) and provides better agreement for the velocity fluctuations, as shown in Fig. 6.32.

6.2.9 Conclusion for the single-phase flow simulations

The results provided by the gas LES solver from AVBP_TPF show very good agreement with the measurements. The accuracy is as good as the results from CDP for radial and axial profiles of mean and fluctuating velocities. Nevertheless, the challenge has been difficult to take up and the investigation of many parameters has been necessary: the convective scheme and both the resolution and the type of grid used constitute the two key points of such simulations. Choosing the most accurate subgrid model, wall treatment and inlet boundary condition increases the level of accuracy of the predictions.

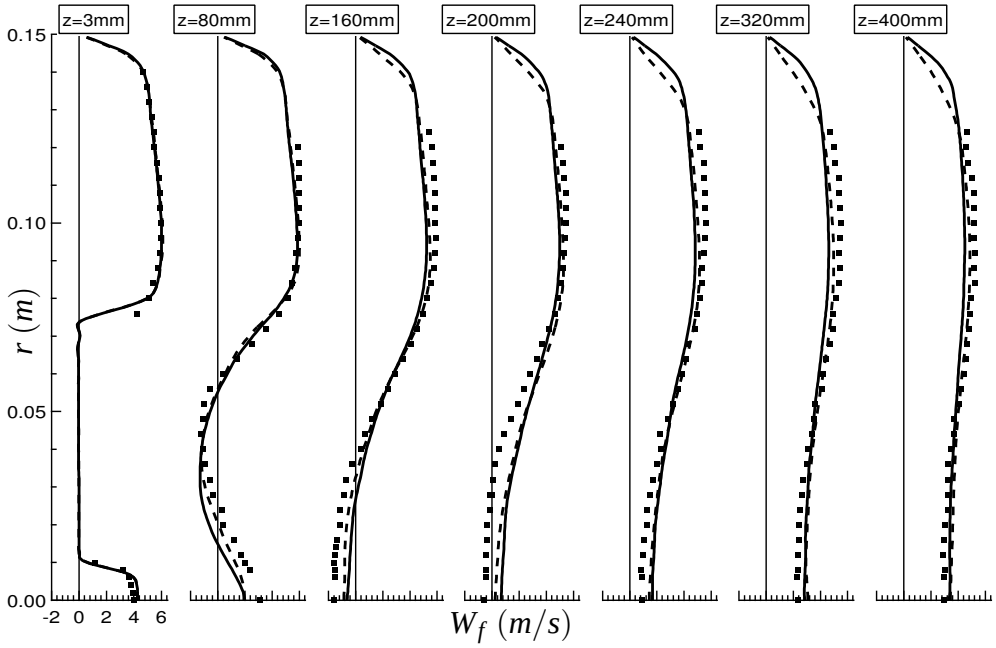

Figure 6.31 - **Coflow turbulent forcing influence.** *Radial profiles of mean axial gas velocity at 7 stations along z axis. Symbols: experiment – Dashed line: Nst2_ttgc_wale_wnm_rfgint – Solid line: Nst2_ttgc_wale_wnm_rfgall.*

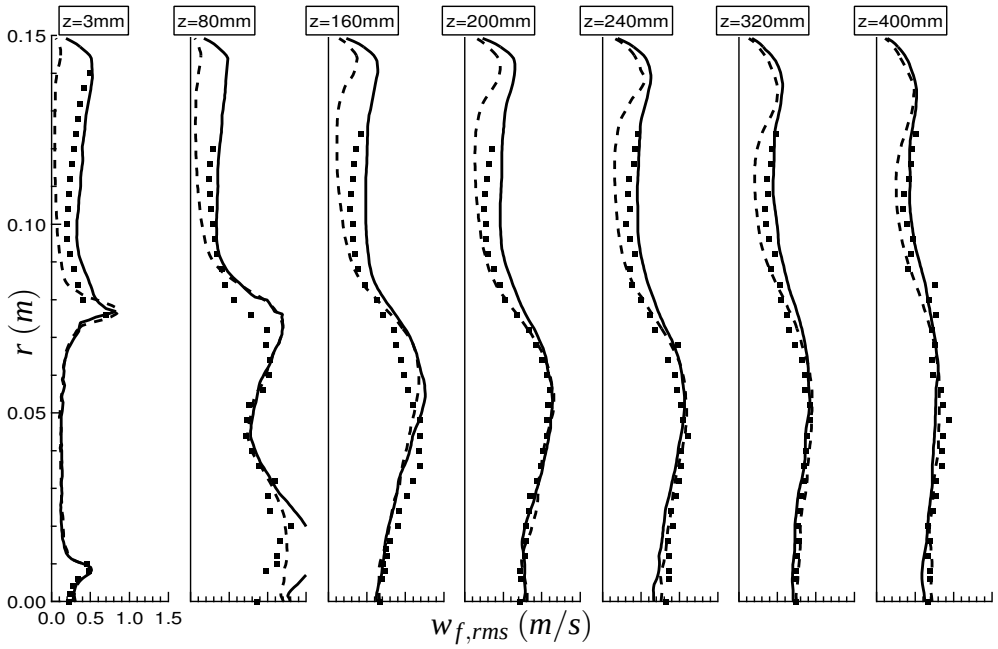

Figure 6.32 - **Coflow turbulent forcing influence.** *Radial profiles of RMS axial gas velocity at 7 stations along z axis. Symbols: experiment – Dashed line: Nst2_ttgc_wale_wnm_rfgint – Solid line: Nst2_ttgc_wale_wnm_rfgall.*

6.3 Two-phase flow simulations

Although the distribution of particles introduced experimentally in the inner pipe is multidisperse, a monodisperse distribution of particles is calculated and analysed hereafter. There are two main reasons. First, no work has been devoted to the multidisperse description of the dispersed phase using the EE mesoscopic approach during this PhD. Then, this topic has been studied separately by V. Moureau at CTR using the CDP Lagrangian solver to compare the results obtained with a multidisperse jet and a monodisperse distribution. In the monodisperse case, the particle diameter was equal to the mean diameter: $\bar{d_p} = 60\ \mu m$. He showed that considering a monodisperse distribution is sufficient to capture both the mean flow effects on the gas (through two-way coupling) and the dynamics of the 60 microns particle class in this case.

The validation of the particle dynamics in this recirculating gas flow is done in two steps using three different codes: CDP and AVBP_TPF-EL that both calculate the particle motion with a Lagrangian approach, and AVBP_TPF-EE that uses the Eulerian mesoscopic approach. First, since the gas LES solvers from AVBP_TPF and CDP give very similar results, the two Lagrangian solvers can be compared and validated by comparisons with the measurements. Second, the two approaches (EL and EE mesoscopic) are compared using AVBP_TPF-EL and AVBP_TPF-EE. As the gas solver and the grid are exactly the same, a direct comparison of the two methods is proposed. Hereafter, for the sake of clearness, the comparison between the two Lagrangian codes is not presented. The main results are however reported in Riber *et al.* (2006).

In this section, focus is made on comparing the EL and EE mesoscopic approaches using the same gas LES solver of AVBP_TPF and two different solvers for the dispersed phase. According to the results obtained for the particle-laden confined jet in Chapter 5, the simplified EE mesoscopic model, that consists in neglecting the RUM contributions in the particulate transport equations, is preferred for this bluff body configuration, Hereafter, Section 6.3.1 summarises the grid, and the numerical parameters for the gas and the dispersed phase. Then, a qualitative analysis of the particle motion is proposed in Section 6.3.2. Finally, a quantitative comparison of both approaches is provided in Section 6.3.3.

6.3.1 Numerical parameters

• The grid

In Section 6.2.7, the predictions of the gas phase have been shown to mainly depend on the grid resolution and type: the structured grid called *bb_meshst* provides the most accurate results mainly because it contains much more cells than the two unstructured grids tested. How-

ever, increasing the number of cells is computationaly expensive. As shown in Table 6.7, using the unstructured grid *bb_meshnst1* is about five times cheaper than using the structured grid *bb_meshst*. Considering the increase in CPU time due to the resolution of the dispersed phase, it has been decided to compare the EL and EE mesoscopic approaches on the unstructured grid *bb_meshnst1*. Note that the quality of the results obtained for the gas phase (see Section 6.2.7) is sufficient to conclude about the accuracy of the method used for the dispersed phase.

• The gas phase

In these two-phase flow simulations, the two codes AVBP_TPF-EL and AVBP_TPF-EE use strictly the same parameters for the gas, corresponding to the case *Nst1_ttgc_wale_wnm_rfgint* detailed in Section 6.2.4. Hereafter, Table 6.8 reminds the parameters for the gas phase.

Name	Mesh	Scheme	Turb. model	Wall model	Inlet BC
Nst1_ttgc_wale_wnm_rfgint	*bb_meshnst1*	TTGC	WALE	None	RFG Int.

Table 6.8 - *Description of the gaseous parameters. Configuration of Borée* et al. *(2001).*

• The dispersed phase

In contrast, the conditions for the dispersed phase are not strictly identical for both approaches. The physical properties of the particles are set in agreement with the experiments: their density is $\rho_p = 2470\ kg.m^{-3}$ and their diameter is chosen constant and equal to the mean one, $d_p = d_p = 60\ \mu m$. The treatment of the inlet boundary condition is the main difference. In the Eulerian simulations, the particles are injected at the inlet of the inner pipe (corresponding to $z = -200\ mm$) and their mean velocity and mass flux is imposed in agreement with the measurements. In the Lagrangian simulations, the particles are injected on the centerline of the inner pipe, but at $z = -1\ mm$, just before entering the chamber. The main reason for this choice is that modeling of the wall BC for the particles is not available in AVBP_TPF-EL yet. Moreover, a fluctuating particle velocity corresponding to 10 % of the mean particle velocity is added.

In terms of numerical parameters, the EE mesoscopic approach uses the same methodology as in the confined jet configuration, as shown in Table 6.9. The TTGC scheme is used with the particle AV model and the particle subgrid eddy-viscosity model is activated to account for the unresolved scales.

Convective scheme	AV model	Subgrid model	RUE flux limitor
TTGC	Jameson	eddy viscosity	No

Table 6.9 - *Numerical method for the dispersed phase computed with the EE mesoscopic approach. Configuration of Borée et al. (2001).*

6.3.2 Two-phase flow topology

In this section, the motion of particles is qualitatively analysed by showing instantaneous and time-averaged LES fields of particle velocity. The role of the particle subgrid model is briefly presented. Then, the EL and EE mesoscopic approaches are compared showing instantaneous fields of respectively reconstructed particle number density and particle number density.

Figure 6.33 compares instantaneous fields of gas and particle velocity in the cutting plane $y = 0$. Three main comments can be made. First, the gaseous smallest structures are much smaller than the particulate smallest structures. Second, there is a strong correlation between the two velocity fields: the shape and the intensity of the recirculation zones are comparable. Finally, the main difference between the two phases is the penetration of the jet. Indeed, the particles are stopped in the jet further than the gaseous stagnation point. This is confirmed by Fig. 6.33 c. where an instantaneous field of particle number density is plotted. Small clusters of particles form between the chamber inlet and the particle stagnation point. There, lots of particles are stopped before they are ejected from the centerline by the gaseous recirculation zones where they are kept.

The time-averaged LES fields look vey different from the instantaneous fields and are displayed in Fig. 6.34 for the dispersed phase only. Focus is made on the particle mean axial velocity, and RMS axial and radial velocities. All the fields are rather symmetrical, suggesting a good level of convergence. When comparing these particulate time-averaged LES fields with the gaseous ones presented in Fig. 6.11, the comments are not very different from the particle-laden confined jet configuration. The mean fields for the two phases are similar whereas the RMS fields show at least two differences. First, the particle RMS quantities are smaller than the gas ones. Second, the particle RMS axial velocity component is larger than the radial component, revealing again an anisotropy of the particle RMS field that is not observed for the gas phase.

In Fig. 6.35, the role of the particle subgrid eddy-viscosity model is shown, making the difference between the deviatoric and the spherical subgrid contributions of the subgrid viscosity. Again, the results are very similar to the confined jet configuration. The two fields show the same topology, suggesting that the subgrid eddy-viscosity model mainly acts in the regions where concentration of particles occurs. Moreover, the spherical part that is negligible for the

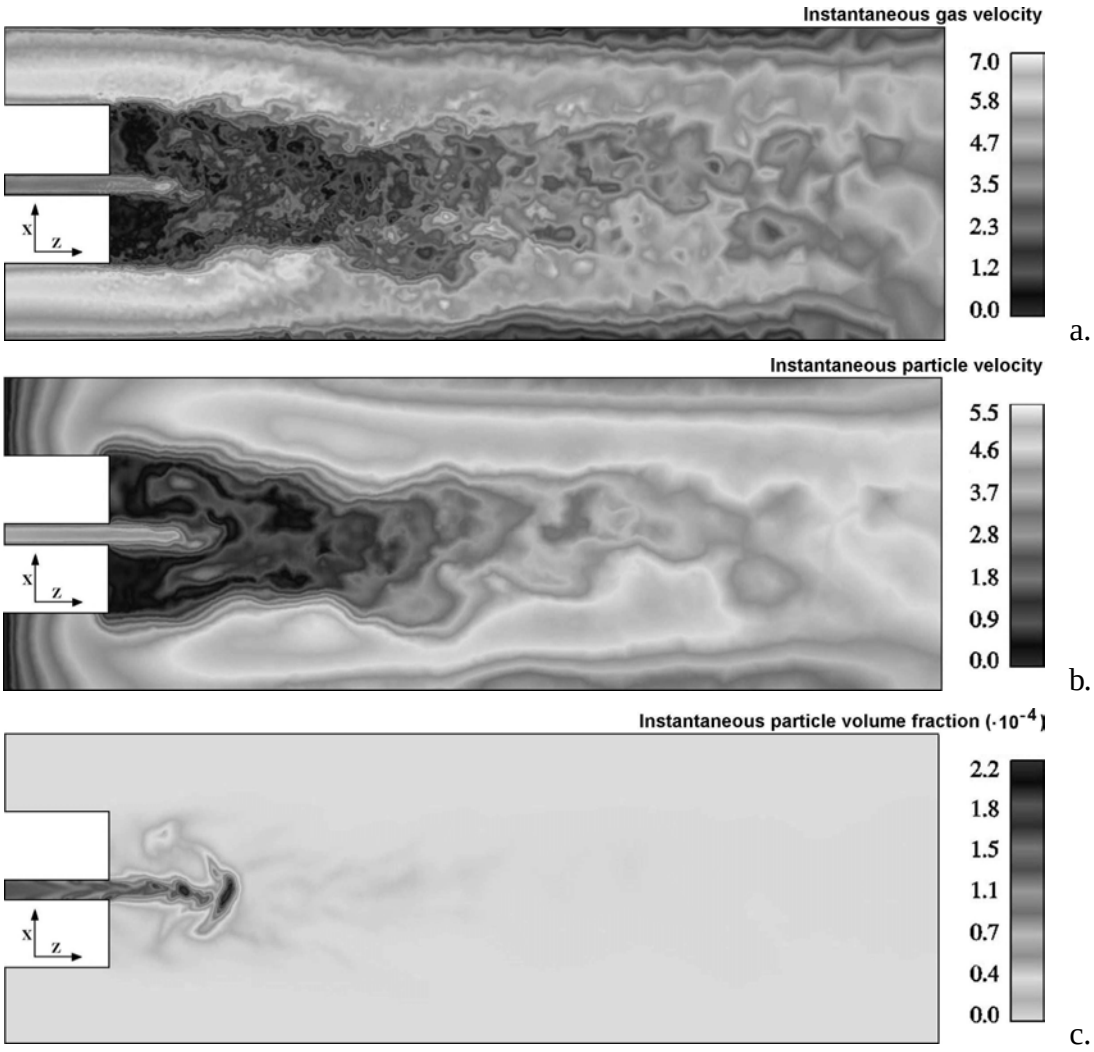

Figure 6.33 - *Topology of the two-phase flow. Instantaneous fields of gas velocity modulus (a.). particle velocity modulus (b.), and particle volume fraction (c.) obtained with* AVBP_TPF-EE *in the cutting plane* $y = 0$. *The black line corresponds to the iso-contour line* $\langle W_p \rangle = 0$. *Configuration of Borée* et al. *(2001).*

gas phase cannot be omitted for the dispersed phase as it is about three orders of magnitude larger than the deviatoric part.

Finally, as the purpose here is to evaluate the accuracy of the EL and EE mesoscopic approaches in this bluff body configuration, a comparison of instantaneous fields of particle number density for the two methods is provided in Fig. 6.36. Nevertheless, in the Lagrangian approach, real particles are tracked whereas a particle number density is transported in the Eulerian approach. To compare both methods, it is therefore necessary to reconstruct a particle number density

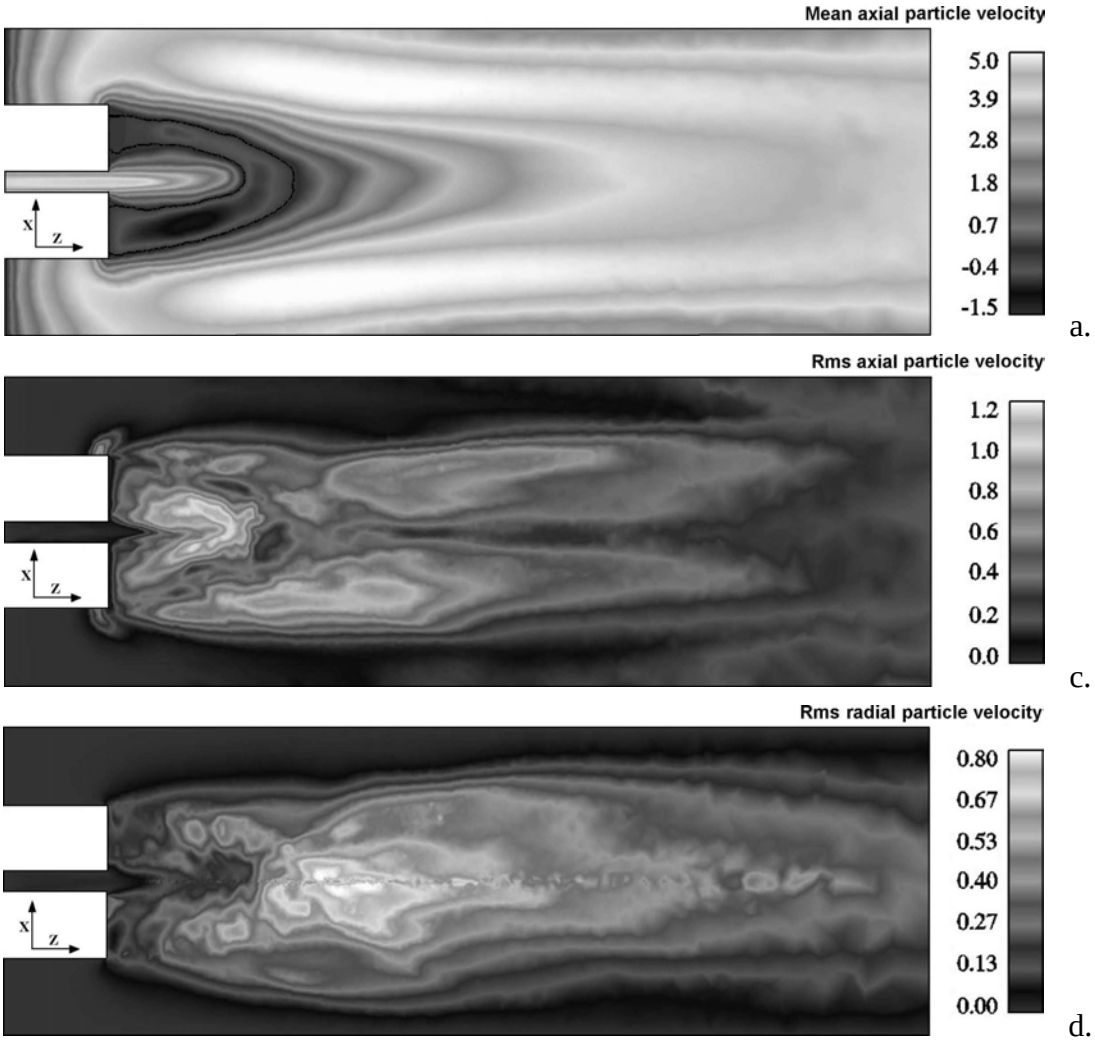

Figure 6.34 - *Topology of the two-phase flow. Mean fields of particle axial velocity (a.), and RMS fields of particle axial (b.) and radial (c.) velocity obtained with* AVBP_TPF-EE *in the cutting plane* $y = 0$. *Configuration of Borée* et al. *(2001).*

from the Lagrangian simulations using a volumic projection method. Then, the two fields seem very similar although more particles are visible in the recirculation zone close to the walls with the Lagrangian approach. This first comparison between the two approaches is consequently very promising for the EE mesoscopic approach that is often said to be too diffusive for the particle number density.

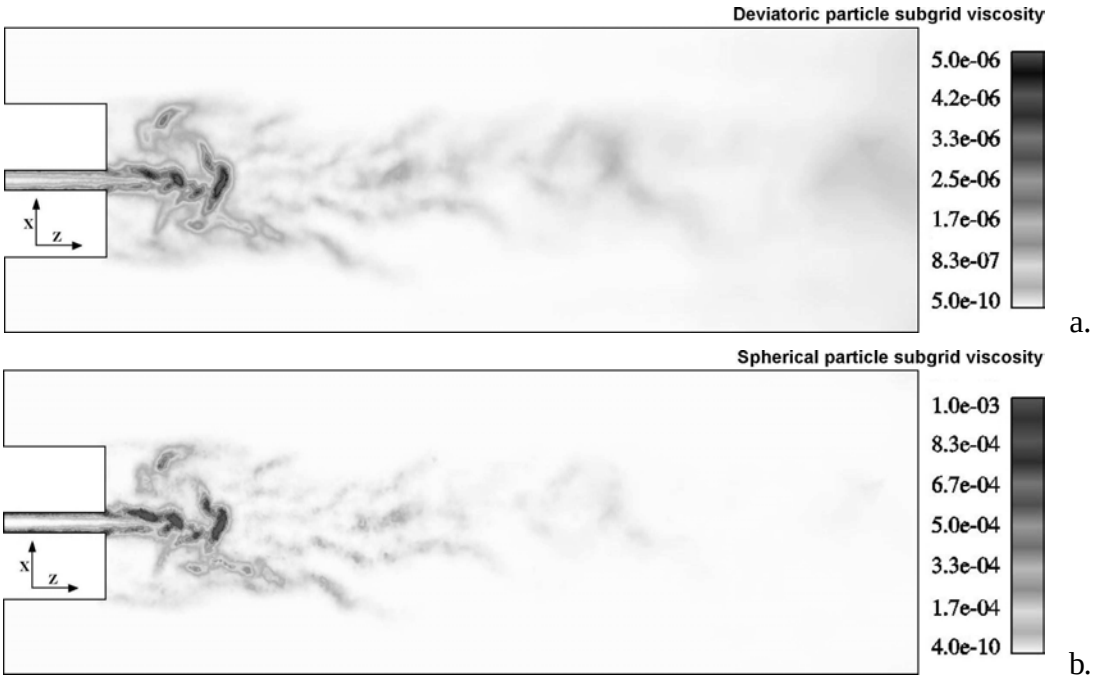

Figure 6.35 - *Instantaneous fields of particle deviatoric (a.) and spherical (b.) subgrid viscosity defined in Eq. (4.22) and obtained with* AVBP_TPF-EE *in the cutting plane* $y = 0$. *Configuration of Borée* et al. *(2001).*

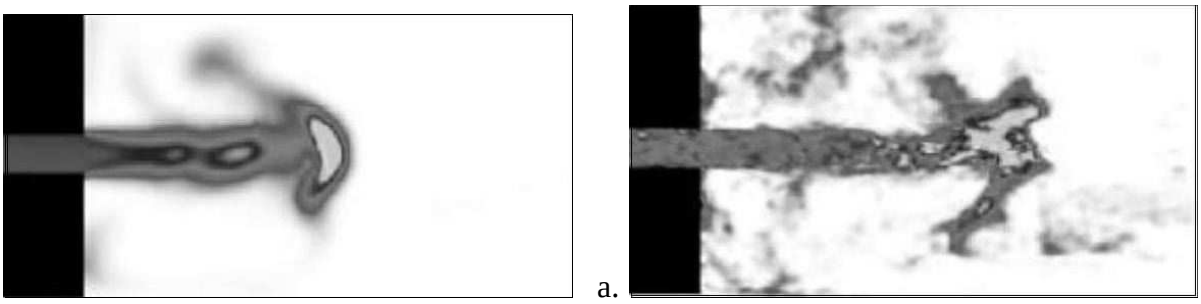

Figure 6.36 - *Instantaneous fields of reconstructed particle number density obtained with AVBP_TPF-EL (a.) and particle number density obtained with AVBP_TPF-EE (b.) in the cutting plane* $y = 0$. *Configuration of Borée* et al. *(2001).*

6.3.3 Comparison of the EL and EE mesoscopic approaches

In this section, radial profiles of mean and RMS velocities for both phases are diplayed and direct comparisons between the AVBP_TPF-EL and the AVBP_TPF-EE results (respectively dotted-dashed and solid lines) are proposed. The symbols stand for the experiments.

The results for the gas phase are presented in Figs. 6.37 – 6.40. There are at least three main points to comment. First, the two approaches give very similar results for all the quantities considered. Second, these results are in good agreements with the measurements, although there are some discrepancies when considering the mean axial velocity on the centerline of the chamber and the RMS velocities in the coflow. The same observations were made in Section 6.2, due to the gaseous parameters that are not optimum in this simulation: the resolution for grid *bb_meshnst1* has been shown to be unsufficient and the RFG method must be used in the coflow to improve the results in this region. Therefore, these discrepancies should not be due to the particle solver. Finally, the influence of the two-way coupling can be evaluated comparing Figs. 6.37 – 6.40 with Figs. A.4 – A.7 displayed in Appendix A. For this low mass loading case, the impact of the two-way coupling seems very little, both when comparing the experiments and the simulations. Consequently, extending the EE mesoscopic approach to two-way coupling without theoretically proving its validity (see Section 1.5) is not crucial in our case. The same conclusion may not be straightforward when calculating the high mass loading case.

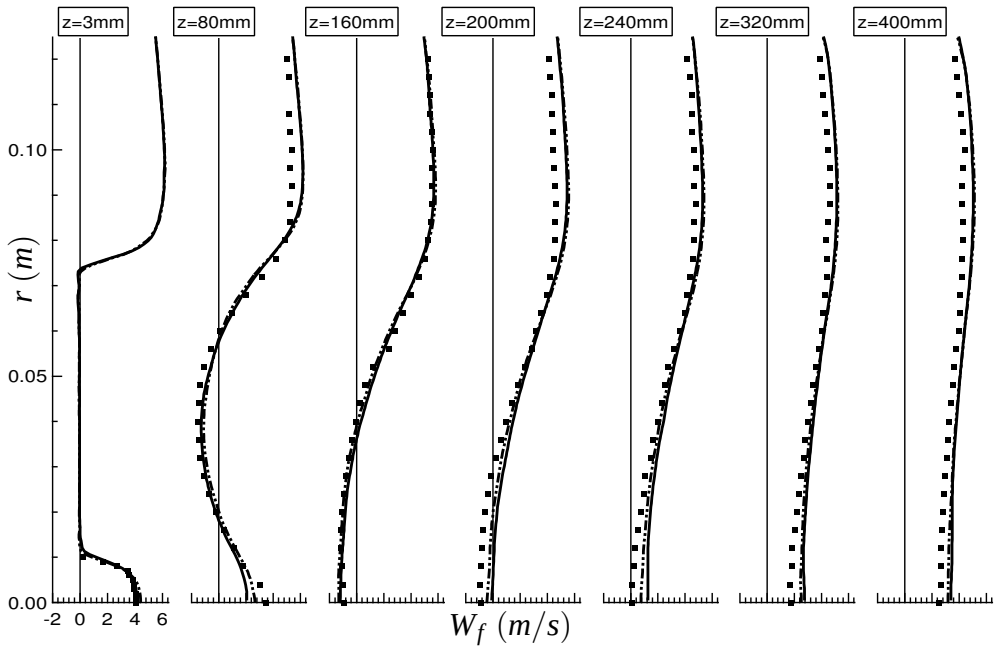

Figure 6.37 - *Radial profiles of mean axial gas velocity at 7 stations along z axis. Symbols: experiment – Dotted-dashed line: AVBP_TPF-EL – Solid line: AVBP_TPF-EE.*

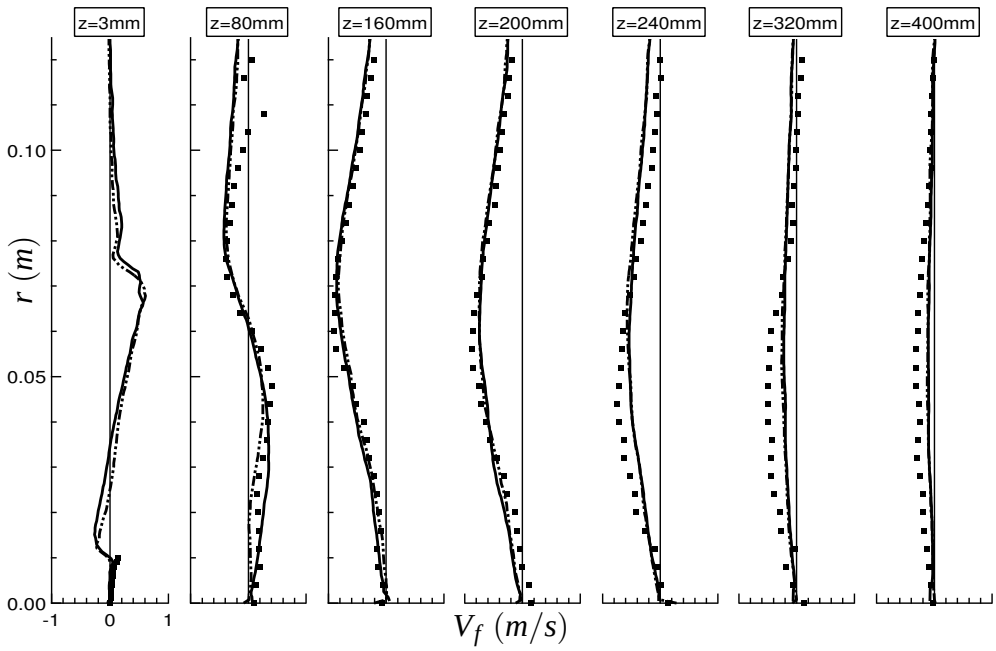

Figure 6.38 - *Radial profiles of mean radial gas velocity at 7 stations along z axis. Symbols: experiment – Dotted-dashed line: AVBP_TPF-EL – Solid line: AVBP_TPF-EE.*

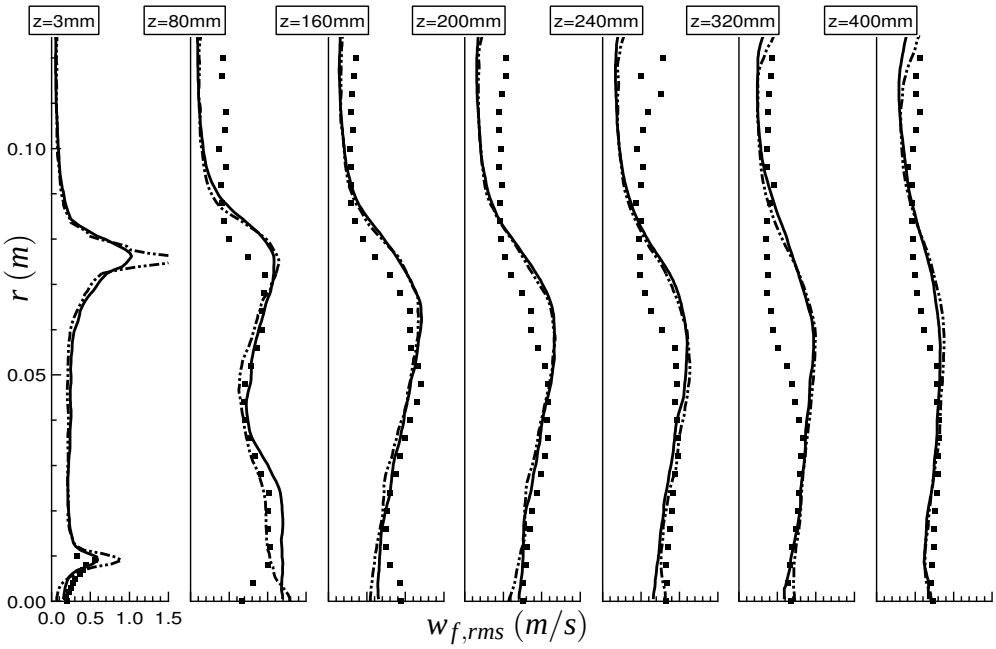

Figure 6.39 - *Radial profiles of RMS axial gas velocity at 7 stations along z axis. Symbols: experiment – Dotted-dashed line: AVBP_TPF-EL – Solid line: AVBP_TPF-EE.*

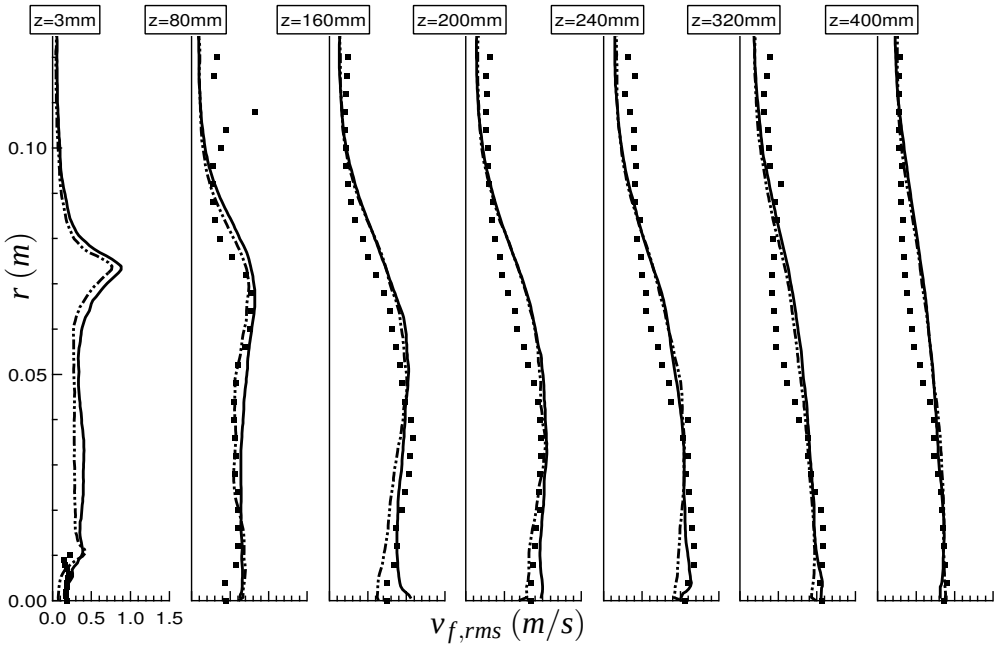

Figure 6.40 - *Radial profiles of RMS radial gas velocity at 7 stations along z axis. Symbols: experiment – Dotted-dashed line: AVBP_TPF-EL – Solid line: AVBP_TPF-EE.*

The results for the dispersed phase are displayed in Figs. 6.41 – 6.44. The overall agreement of both methods with the experiments is good. When comparing the mean axial and radial velocities, the EL and EE mesoscopic approaches give almost the same results. The particle jet spreading is well predicted while the location of the stagnation point is slightly under-estimated. This may be due to the discrepancies observed on the gas mean axial velocity in Fig. 6.37. The conclusion is slightly different when focusing on the RMS quantities. On the one hand, the two methods have some difficulties predicting the particle agitation at the locations $z = 80$ *m* and $z = 160$ *mm*, that is to say upstream from the stagnation point. This may be linked to the discrepancies observed at the same locations for the gas phase (see Fig. 6.39 for instance). Note that the over-predictions of RMS velocities in the coflow with the EL approach are due to the averaging process that would require more particles in this region. On the other hand, the EE mesoscopic approach under-predicts the particle agitation. This is not surprising since the RUM contributions are neglected here as it was the case in the confined jet configuration.

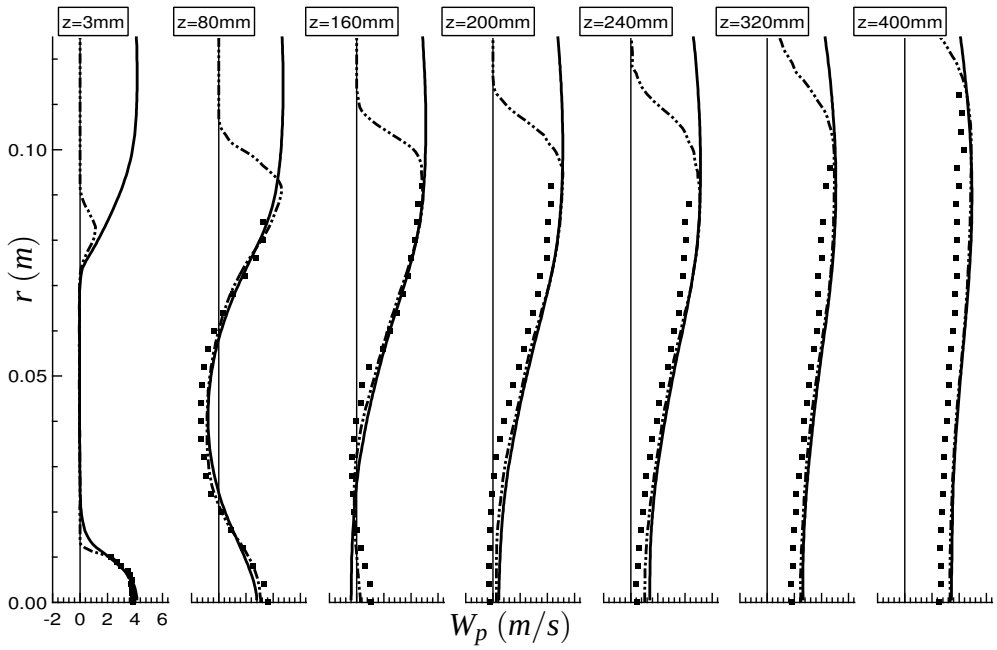

Figure 6.41 - *Radial profiles of mean axial particle velocity at 7 stations along z axis. Symbols: experiment – Dotted-dashed line: AVBP_TPF-EL – Solid line: AVBP_TPF-EE.*

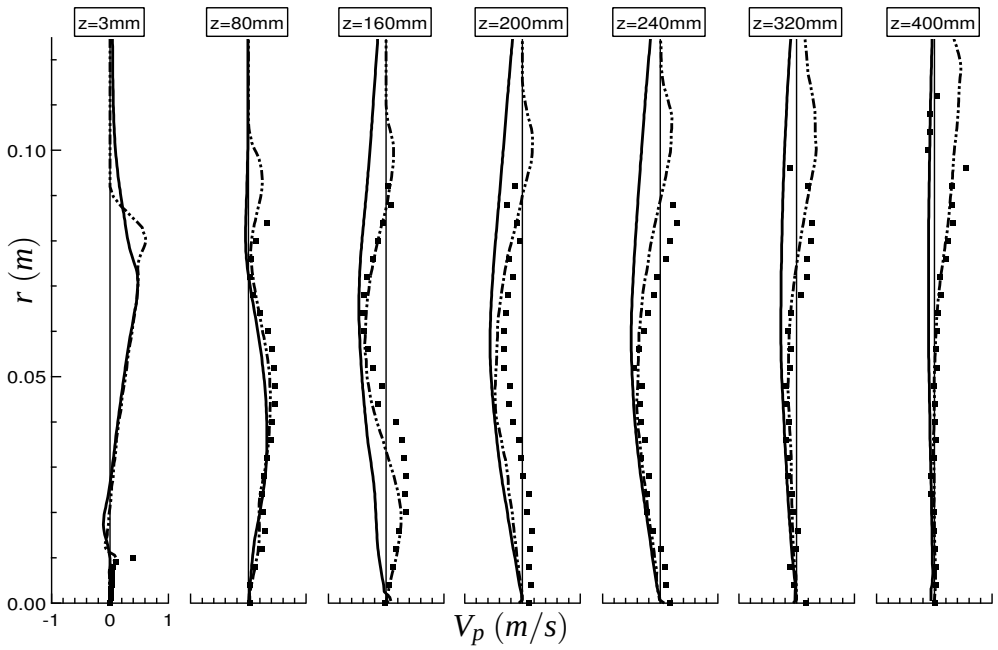

Figure 6.42 - *Radial profiles of mean radial particle velocity at 7 stations along z axis. Symbols: experiment – Dotted-dashed line: AVBP_TPF-EL – Solid line: AVBP_TPF-EE.*

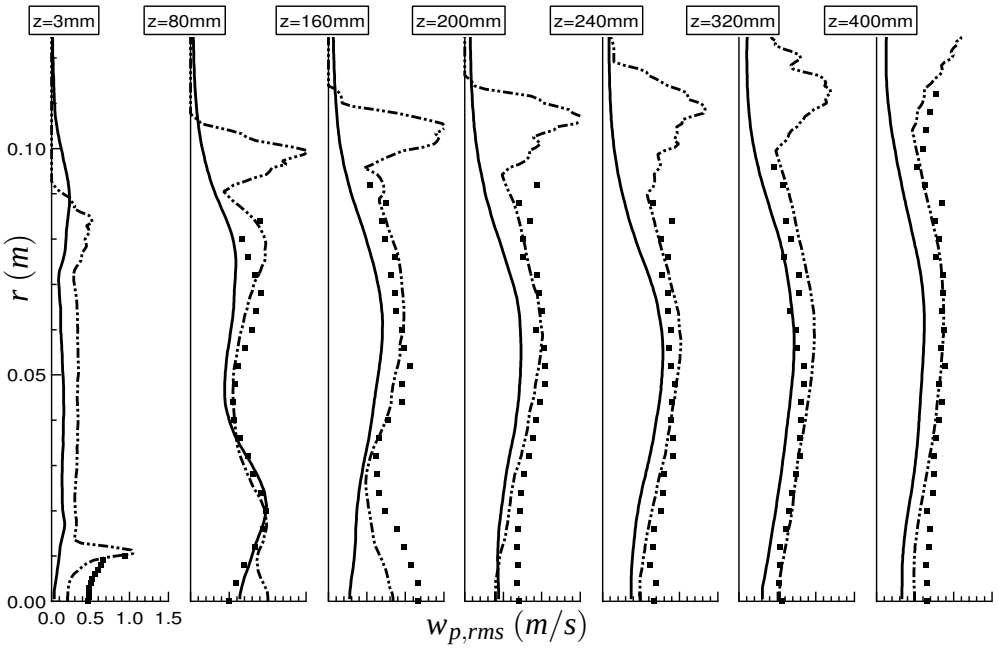

Figure 6.43 - *Radial profiles of RMS axial particle velocity at 7 stations along z axis. Symbols: experiment – Dotted-dashed line: AVBP_TPF-EL – Solid line: AVBP_TPF-EE.*

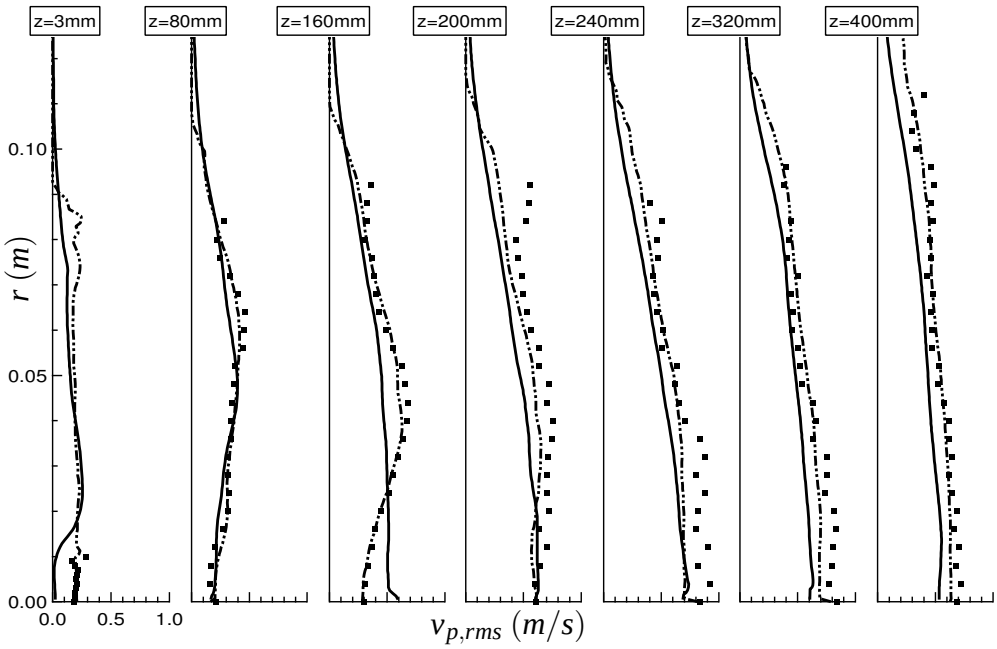

Figure 6.44 - *Radial profiles of RMS radial particle velocity at 7 stations along z axis. Symbols: experiment – Dotted-dashed line: AVBP_TPF-EL – Solid line: AVBP_TPF-EE.*

6.4 Conclusion

There are two main reasons why the particle-laden bluff body configuration has been calculated using LES:

- The context of this work is the simulations of reactive turbulent two-phase flows in aeronautical combustion chambers. After the promising results obtained in the particle-laden confined jet (see Chapter 5), it was necessary to test the new LES EE mesoscopic model in a more realistc geometry showing recirculation zones for instance.
- The validations of the method must be precise and numerous. This is the case for the bluff body configuration: detailed measurements are provided in Borée *et al.* (2001) and direct comparisons between the EL and EE mesoscopic approaches have been made during the CTR Summer program.

In this configuration where particles are inertial, but still much dependent on the gas flow, the predictions of the particle motion strongly depend on the results for the gas phase.
Nevertheless, accurate predictions of the gas phase have been delicate to obtain. Therefore a detailed study has been required to investigate the influence of numerous parameters on the gas flow. The grid and the convective scheme are the major parameters to account for. Concerning the grid, numerous points are required in the whole domain, and especially in the inner pipe and close to the walls. In our case, a structured grid has given the most accurate results. As for the numerical scheme, TTGC is once again the best candidate for the grid resolution affordable today. Then, some other parameters show minor influence on the predictions: the Random Flow Generation method used at the inlet of the pipes prevents relaminarisation of the gas flow in the pipes themselves. Combining no wall treatment with the WALE subgrid model also improves the results. Thus, this detailed study has shown the capability of the gas LES solver from AVBP_TPF to very precisely predict the fluid flow in such a configuration. The results the code provide are in very good agreement with the experiments, and with the results provided by the gas LES solver from CDP.
The accuracy of the Eulerian mesoscopic approach has then been shown by comparison with the experiments and the Lagrangian approach. Because the two approaches can be used in AVBP_TPF, the comparison is direct as both the grid and the gas solver are identical. The results for the dispersed phase are in good agreement with the measurements for both approaches. Concerning the mean quantities, the predictions are very close for both methods. Only the agitation of the particles is slightly under-estimated with the EE mesoscopic approach, suggesting again than the RUM contribution cannot be neglected.

There is still lots of points to be investigated in this bluff body configuation. First, accounting for the RUM modeling is undoubtlessly required to better predict the particle agitation, provided the RUM viscosity model is improved (see Section 5.6). Then, the impact of the two-way

coupling on the gas phase should be analysed in details. As it seems more important for the larger mass loading (Borée *et al.*, 2001), this second case should also be investigated, which requires to model the inter-particle collisions and to account for polydispersion.

Conclusion

Une nouvelle méthode de Simulation aux Grandes Echelles pour les écoulements diphasiques à phase dispersée, turbulents et non-réactifs est proposée. Elle repose sur le formalisme Eulérien mésoscopique introduit par Février *et al.* (2005) qui suggère une décomposition de la vitesse de chaque particule en une vitesse spatialement corrélée, et une vitesse décorrélée. La dérivation des équations LES pour la phase dispersée requiert donc, outre la moyenne d'ensemble conditionnée par une réalisation fluide, l'application d'un filtre spatial LES classique. Il en résulte deux types de termes non fermés à modéliser, qui proviennent de la moyenne d'ensemble d'une part, et du filtrage spatial LES d'autre part. La mise en oeuvre numérique de ce système d'équations ainsi que son application à des géométries complexes nécessitent le développement, l'implantation et la validation de divers modèles :

- **Méthodes numériques :** la résolution numérique des équations particulaires en mode DNS, i.e. avant filtrage LES, s'avère complexe pour deux raisons principales. D'une part, leur dérivation ne fait pas apparaître naturellement de terme diffusif comme c'est le cas pour la phase gazeuse. D'autre part, la phase dispersée est fortement compressible, et ce d'autant plus que l'inertie des particules augmente. Il en résulte l'apparition de très forts gradients de densité par exemple, difficiles à représenter et à convecter sur une grille de calcul. La solution proposée par Kaufmann *et al.* (2006) consiste à introduire un terme de sous-maille dans l'équation de vitesse corrélée et ainsi, à résoudre les équations particulaires pour des grandeurs filtrées (densité, vitesses corrélée et décorrélée). Si la stabilité de la méthode numérique s'en trouve accrue, il apparaît cependant une forte diffusion de la densité de particules. Dans cette étude, l'erreur de dispersion importante du schéma numérique jusqu'alors utilisé (LW) est mise en cause et il est montré que l'utilisation d'un schéma de type Taylor-Galerkin (TTGC) (Colin, 2000), non seulement moins dispersif mais également moins dissipatif, améliore significativement les résultats pour la phase dispersée. Par ailleurs, un modèle de dissipation artificielle basé sur celui de Jameson *et al.* (1981) et adapté à la phase dispersée complète le dispositif pour réaliser des calculs stables et précis. Enfin, un limiteur de flux pour les flux Euler de l'équation de transport de l'énergie décorrélée des particules est utilisé pour garantir la positivité de cette quantité soumise à de fortes variations de cellule à cellule.

- **Modèles de sous-maille particulaires :** ils ont été proposés parallèlement à cette étude par Moreau (2006) qui a utilisé l'approche lagrangienne pour effectuer des DNS de THI chargée en particules. Un double filtrage, au sens moyenne d'ensemble puis LES, a permis de tester *a priori* plusieurs modèles pour les termes non fermés. Ceux issus de la moyenne d'ensemble ont été modélisés par analogie avec les fermetures de type RANS (Simonin, 1991) tandis que ceux résultant du filtrage spatial ont été modélisés par analogie avec les modèles de sous-maille développés pour les écoulements monophasiques compressibles. Dans ce travail, les modèles présentant le meilleur compromis entre d'une part la qualité des résultats *a priori* et d'autre part la facilité d'implantation numérique ont été retenus et intégrés au code AVBP_TPF.

- **Condition limite d'entrée particulaire :** les écoulements diphasiques considérés dans cette étude sont suffisamment dilués pour négliger les collisions inter-particulaires. Par ailleurs, la modélisation des interactions particules-parois n'est pas cruciale pour les configurations retenues. Dans celles-ci pourtant, les particules sont injectées dans la chambre avec de l'air par le biais de tubes. A défaut de calculer l'écoulement gaz-particules dans ces conduits, il est important de tenir compte du mouvement des particules dans les tubes pour écrire une condition aux limites adéquate en entrée de chambre. Les expériences nous indiquent que les fluctuations particulaires sont partiellement corrélées à celles du fluide. Les différences entre les deux phases proviennent principalement de l'inertie des particules, des collisions, même faibles, entre particules, et des interactions particules-parois. Ainsi, la condition aux limites développée dans cette thèse propose d'imposer, en plus de la vitesse particulaire moyenne, une fluctuation de vitesse particulaire qui se décompose par analogie avec la décomposition de Février *et al.* (2005), en une fluctuation spatialement corrélée et une fluctuation décorrélée. Seule la première contribution est alors partiellement corrélée à la fluctuation gazeuse. Le développement de cette condition aux limites s'est faite par étapes et la version la plus élaborée a été implémentée dans le code AVBP_TPF.

L'apport de ces différents modèles pour la compréhension et la simulation des écoulements gaz-particules s'est révélé essentiel pour la calcul des trois configurations retenues dans le cadre cette thèse.

Dans le Chapitre 3, les Simulations Numériques Directes de THI décroissante chargée en particules ont démontré la capacité du nouveau modèle numérique à augmenter la robustesse et la précision du code AVBP_TPF. Dans ces simulations, le terme de sous-maille introduit par Kaufmann *et al.* (2006) et dont la présence était jusqu'alors difficile à justifier, n'est plus nécessaire. Plus encore, la comparaison avec des résultats lagrangiens fournis par Moreau (2006) a montré la capacité du formalisme Eulérien mésoscopique associé aux modèles de fermeture proposés par Simonin *et al.* (2002) puis Kaufmann *et al.* (2006) à prédire précisément le mouvement de particules très inertielles dans une THI gazeuse. Une

analyse de l'évolution spatio-temporelle des grandeurs intégrales telles que l'énergie totale des particules, la corrélation fluide-particules et la ségrégation montre un très bon accord entre les deux méthodes. La ségrégation reste cependant légèrement sous-estimée, d'environ 20%, par l'approche Eulérienne. Par ailleurs, une analyse spectrale confirme la qualité des simulations Eulériennes, légèrement dégradée aux petites échelles où la pente en k^{-2} sugérée par Moreau (2006) n'est pas reproduite. La dépendance des résultats à la résolution spatiale, la sous-estimation de la ségrégation et le défaut de reproduction du spectre aux petites échelles incitent à poursuivre les investigations numériques. Dans cette optique, une thèse vient de débuter au CERFACS et des schémas "upwind" multidimensionnels (voir (Tomaich, 1995) par exemple) sont actuellement à l'étude. Ils sont basés sur une distribution de l'intégrale des flux convectifs d'une cellule aux noeuds du maillage en tenant compte du sens de propagation de l'information. Ces schémas sont potentiellement moins dissipatifs et plus précis que les schémas actuels d'AVBP_TPF, notamment lors du traitement de chocs.

La LES avec une approche Eulérienne du jet d'air turbulent vertical chargé en particules (Hishida *et al.*, 1987) constitue à la connaissance de l'auteur la première tentative de ce genre dans la communauté diphasique. Ce calcul analysé dans le chapitre 5 permet d'affirmer la nécessité d'inclure les fermetures de sous-maille proposées par Moreau (2006). De même la condition aux limites d'entrée portant sur la fluctuation de vitesse particulaire décrite ci-dessus apparaît primordiale pour la juste prédiction de la dispersion des particules dans un tel champ gazeux turbulent. Cette configuration donne l'occasion d'effectuer deux types de calcul. Le premier calcul néglige les effets du mouvement décorrélé en ne résolvant que les équations de transport pour la densité et la vitesse corrélée des particules. Des comparaisons avec les résultats expérimentaux montrent que ce modèle simplifié permet de prédire correctement les flux moyens de masse et de quantité de mouvement des particules. En revanche, l'agitation des particules, qui ne tient compte dans ce calcul que de leur mouvement corrélé, est sous-estimée. Une évaluation *a posteriori* de la contribution du mouvement décorrélé est proposée en utilisant la corrélation de Vance *et al.* (2006). En sommant la contribution du mouvement corrélé issue de la LES et la contribution du mouvement décorrélé estimée *a posteriori*, le niveau d'agitation particulaire s'accorde avec les mesures expérimentales. Le second calcul tient compte de la dissipation du mouvement décorrélé dans l'équation de quantité de mouvement corrélé particulaire et propose de résoudre en outre l'équation pour l'énergie décorrélée des particules. Cependant ce modèle ne s'avère pas satisfaisant car il conduit à une relaminarisation de l'écoulement particulaire. Une série de tests a permis de remettre en cause le modèle de viscosité utilisé pour la fermeture des corrélations doubles : sa valeur semble trop élevée mais sa forme pourrait également, à terme, être discutée. Une nouvelle thèse portant sur la modélisation Eulérienne mésoscopique vient de débuter au sein du groupe EEC de l'IMFT et devrait apporter des réponses à ces questions.

Compte-tenu de ces résultats, le modèle LES Eulérien mésoscopique sans prise en compte directe du mouvement décorrélé, a finalement été mis en oeuvre dans une géométrie réaliste

de chambre de combustion aéronautique. Le calcul d'un jet turbulent recirculant chargé en particules (Borée *et al.*, 2001) fait l'objet du Chapitre 6 et permet de développer deux principaux points. D'une part, les résultats LES de l'écoulement monophasique s'avèrent fortement dépendants du maillage, du schéma convectif, ainsi que des conditions aux limites d'entrée et de paroi. L'influence de l'ensemble des paramètres est décrite et le calcul garantissant les prédictions les plus précises comparativement aux mesures expérimentales est comparé avec un calcul mené par V. Moureau avec le code CDP développé par l'université de Stanford. La précision du solveur gazeux d'AVBP_TPF, pour les grandeurs moyennes et fluctuantes, est ainsi démontrée. D'autre part, le développement d'un module lagrangien dans le code AVBP_TPF dans le cadre de la thèse de M. García a permis de comparer directement les descriptions Lagrangienne et Eulérienne mésoscopique dans cette configuration. Il ressort que les deux modèles s'accordent précisément sur la prédiction des grandeurs moyennes avec les mesures expérimentales tandis qu'une fois encore, l'agitation des particules est sous-estimée par le modèle Eulérien mésoscopique pour les mêmes raisons que dans le calcul du jet confiné.

Enfin, il convient de rappeler que cette étude a en grande partie été motivée par la nécessité de développer une description Eulérienne pour les écoulements diphasiques réactifs dans les chambres de combustion aéronautiques. Le modèle Eulérien mésoscopique sans prise en compte directe du mouvement décorrélé des particules a été couplé à des modèles d'évaporation de gouttelettes et de combustion dans le cadre de thèses menées parallèlement par M. Boileau et plus récemment par N. Lamarque, J. Lavédrine et M. Sanjose au CERFACS. Les calculs effectués ont permis de calculer des séquences d'allumage dans des chambres de combustion réalistes en tenant compte de la dispersion et de l'évaporation des gouttelettes de fuel. Dans cette optique, de nombreux points restent à étudier : la prise en compte du couplage inverse dans le modèle Eulérien mésoscopique (thèse de E. Massi Boscolo au sein du groupe EEC de l'IMFT), la polydispersion en sortie d'injecteur (thèse de J. Lavédrine au CERFACS), les collisions inter-particulaires (travaux de recherche de P. Fede à l'IMFT), l'influence des gouttes liquides dans la flamme (thèse de M. Sanjose au CERFACS) et la modélisation des films liquides aux parois (thèse de G. Desoutter à l'IFP) en sont quelques exemples.

Bibliography

ABRAHAMSON, J. 1975 Collision rate of small particles in a vigorously turbulent flow. *Chemical Engineering Science* **30**, 1371 – 1379.

ALBRECHT, A., BÉDAT, B., POINSOT, T. & SIMONIN, O. 1999 Direct numerical simulation and modelling of evaporating droplets in homogeneous turbulence : application to turbulent flames. In *15th Annual Conference on Liquid Atomization and Spray System - ILASS Europe*. Toulouse, France.

ALIPCHENKOV, V. M. & ZAICHIK, L. I. 2006 Modeling of the turbulent motion of particles in a vertical channel. *Fluid Dynamics* **41** (4).

ANDERSON, J.D. 1990 *Modern Compressible Flow*. New York: McGraw-Hill.

ANDREUX, R., HEMATI, M., SIMONIN, O. & FERSCHNEIDER, G. 2002 Hydrodynamic investigation of a cfb: Numerical study and experimental validation. In *Circulating Fluidized Bed Technology VII, Proc. of the 7th Int. Conference on Circulating Fluidized Beds*. Niagara Falls, Canada.

APTE, S.V., GOROKHOVSKI, M. & MOIN, P. 2003*a* Large-eddy simulation of atomizing spray with stochastic modeling of secondary breakup. *Int. J. Multiphase Flow* **29**, 1503–1522.

APTE, S.V., MAHESH, K. & LUNDGREN, T. 2003*b* A Eulerian-Lagrangian model to simulate two-phase particulate flows. In *Annual Research Briefs*. Center for Turbulence Research, NASA Ames/Stanford Univ.

ARMENIO, V., PIOMELLI, U. & FIOROTTO, V. 1999 Effect of the subgrid scales on particle motion. *Phys. Fluids* **11** (10), 3030–3042.

AUPOIX, B. & COUSTEIX, J. 1982 Modèles simples de tensions de sous-maille en turbulence homogène isotrope. *Rech. Aéro.* **4**, 273–283.

BACHALO, W.D. & HOUSER, M.J. 1984 Phase/doppler spray analyser for simultaneous measurements of drop size and velocity distributions. *Opt. Eng.* **23**, 583–590.

BARDINA, J., FERZIGER, J.H. & REYNOLDS, W.C. 1983 "improved turbulence models based on large-eddy simulation of homogeneous, incompressible, turbulent flows. *Tech. Rep.* TF-19. Department of Mechanical Engineering, Stanford University.

BASSET, A.B. 1888 *Treatise on Hydrodynamics, vol. 2*. Deighton Bell, London.

BATCHELOR, G.K. 1949 Diffusion in a file of homogeneous turbulence. Eulerian analysis. *Aust. J. Sci. Res* **2**, 437–450.

BAUM, M. & POINSOT, T. 1992 A direct numerical simulation code for studies of combustion phenomena. *Tech. Rep.* 920201. Laboratoire EM2C du CNRS et de l'Ecole Centrale de Paris.

BOILEAU, M., PASCAUD, S., RIBER, E., CUENOT, B., GICQUEL, L. & POINSOT, T.J. 2007 Large eddy simulation of spray combustion in gas turbines. *Submitted to Flow Turb. and Combustion* .

BOIVIN, M., SIMONIN, O. & SQUIRES, K. D. 1998 Direct numerical simulation of turbulence modulation by particles in isotropic turbulence. *J. Fluid Mech.* **375**, 235–263.

BORÉE, J., ISHIMA, T. & FLOUR, I. 2001 The effect of mass loading and inter-particle collisions on the development of the polydispersed two-phase flow downstream of a confined bluff body. *J. Fluid Mech.* **443**, 129–165.

BOUDIER, P., HENRIOT, S., POINSOT, T. & T., BARITAUD 1992 A model for turbulent flame ignition and propagation in spark ignition engines. In *Twenty-Fourth Symposium (International) on Combustion* (ed. The Combustion Institute), pp. 503–510.

BOUGHANEM, H. & TROUVÉ, A. 1996 Validation du code de simulation directe ntmix3d pour le calcul des écoulements turbulents réactifs. *Tech. Rep.* 42907. Institut Français du Pétrole.

BOUSSINESQ, J. 1877 Théorie de l'écoulement tourbillant. *Mém. Présentés par Divers Savants. Acad. Sci. Inst. Fr.* **23**, 46–50.

BOUSSINESQ, J. 1885 Sur la résistance qu'oppose un liquide indéfini au repos... *Comptes-rendus. Acad. Sci. Inst. Fr.* .

CARAENI, D., BERGSTROM, C. & FUCHS, L. 2000 Modeling of liquid fuel injection, evaporation and mixing in a gas turbine burner using large eddy simulation. *Flow Turb. and Combustion* **65**, 223–244.

CARAMAN, N., BORÉE, J. & SIMONIN, O. 2003 Effect of collisions on the dispersed phase fluctuation in a dilute tube flow : Experimental and theoretical analysis. *Phys. Fluids* **15** (12), 3602–3612.

CATE, A. TEN, DERKSEN, J.J., PORTELA, L.M. & DEN AKKER, H.E.A VAN 2004 Fully resolved simulations of colliding monodisperse spheres in forced isotropic turbulence. *J. Fluid Mech.* **519**, 233–271.

CELIK, I., SMIRNOV, A. & SMITH, J. 1999 Appropriate initial and boundary conditions for les of a ship wake. In *Proceedings of the 3rd ASME/JSME Joint Fluids Engineering Conference, FEDSM99-7851*. San Francisco, California, USA.

CHAKRAVARTHY, S.R. & OSHER, S. 1977 High resolution applications of the osher upwind scheme for the euler applications. In *Proc. AIAA 6th Computational Fluid Dynamics Conference*.

CHASSAING, P. 2000 *Turbulence en mécanique des fluides*. CEPADUES Editions.

CHIN, L.P. & TANKIN, R.S. 1992 Vortical structures from a two-dimensional nozzle with a bluff-body slot. *Physics of Fluids A* **4** (8), 1724–1736.

CLIFT, R., GRACE, J.R. & WEBER, M.E. 2004 Filtered particle tracking for dispersed two-phase turbulent flows. *Academic Press* .

COLIN, O. 2000 Simulations aux grandes échelles de la combustion turbulente prémélangée dans les statoréacteurs. PhD thesis, INP Toulouse.

COLIN, O. & RUDGYARD, M. 2000 Development of high-order taylor-galerkin schemes for unsteady calculations. *J. Comput. Phys.* **162** (2), 338–371.

CRUMPTON, P.I., MACKENZIE, J.A. & MORTON, K.W. 1993 Cell vertex algorithms for the compressible Navier-Stokes equations. *J. Comput. Phys.* **109** (1), 1–15.

CUENOT, B. & POINSOT, T. 1996 Asymptotic and numerical study of diffusion flames with variable lewis number and finite rate chemistry. *Combust. Flame* **104**, 111–137.

DAHM, W.J.A. & DIMOTAKIS, P.E. 1990 Mixing at large Schmidt number in the self-similar far fiel of turbulent jets. *J. Fluid Mech.* **217**, 299–330.

DANON, H., WOLFSHTEIN, M. & HETSRONI, G. 1977 Numerical calculations of two-phase turbulent round jet. *Int. J. Multiphase Flow* **3**, 223–234.

DESJONQUERES, P., BERLEMONT, A. & GOUESBET, G. 1988 A Lagrangian approach for the prediction of particle dispersion in turbulent flow. *J. Aerosol Sci.* **19** (99).

DESJONQUERES, P., GOUESBET, G., BERLEMONT, A. & PICART, A. 1986 Dispersion of discrete particles by continuous turbulent motions: new results and discussions. *Phys. Fluids* **29**, 2147–2151.

DEUTSCH, E. 1992 Dispersion de particules dans une turbulence homogene isotrope stationaire calculee par simulation numerique directe des grandes echelles. Phd thesis, Electricité de France, Chatou.

DEUTSCH, E. & SIMONIN, O. 1991 Large eddy simulation applied to the motion of particles in stationary homogeneous fluid turbulence. *ASME FED* .

DRUZHININ, O.A. 1995 On the two-way interaction in two-dimensional particle-laden flows - the accumulation of particles a nd flow modification. *J. Fluid Mech.* **297**, 49–76.

DRUZHININ, O.A. 2001 The influence of particle inertia on the two-way coupling and modification of isotropic turbulence by microparticles. *Phys. Fluids* **13** (12), 3738–3755.

DRUZHININ, O.A. & ELGHOBASHI, S. 1998 Direct numerical simulations of bubble-laden turbulent flows using the two-fluid formulation. *Physics of Fluids* **10** (3), 685–697.

DUBIEF, Y. & DELCAYRE, F. 2000 On coherent-vortex identification in turbulence. *J. Turb.* **1**, 1–22.

DUCROS, F., COMTE, P. & LESIEUR, M. 1998*a* Large-eddy simulation of transition to turbulence in a boundary layer spatially developing over a flat plate. *J. Fluid Mech.* pp. 1–36.

DUCROS, F., NICOUD, F. & POINSOT, T. 1998*b* Wall-adapting local eddy-viscosity models for simulations in complex geometries. In *Proc. of* 6^{th} *ICFD Conference on Numerical Methods for Fluid Dynamics*, pp. 293–299.

DURST, F., MELLING, A. & WHITELAW, J.H. 1976 *Principles and practice of laser Doppler anemometry*. Academic Press, London.

ELGHOBASHI, S., ABOU-ARAB, T., RIZK, M. & MOSTAFA, A. 1984 Prediction of the particle-laden jet with a two-equation turbulence model. *Int. J. Multiphase Flow* **10**, 697–710.

ELGHOBASHI, S. & TRUESDELL, G. 1993 On the two-way interaction between homogeneous turbulence and dispersed solid particles. *Phys. Fluids* **5** (7), 1790–1801, eR.

ERLEBACHER, G., HUSSAINI, M. Y., SPEZIALE, C. G. & ZANG, T. A. 1992 Toward the large-eddy simulation of compressible flows. *J. Fluid Mech.* **238**, 155–185.

FAVRE, A. 1969 Statistical equations of turbulent gases. In *Problems of hydrodynamics and continuum mechanics*, pp. 231–266. Philadelphia: SIAM.

FEDE, P. 2004 Modélisation et simulation de l'influence de la turbulence sur les collisions dans les écoulements mono et bi-solides. Phd thesis, INP Toulouse.

FEDE, P. & SIMONIN, O. 2006 Numerical study of the subgrid fluid turbulence effects on the statistics of heavy colliding particles. *Phys. Fluids* **18** (045103).

FERRANTE, A. & ELGHOBASHI, S. 2003 On the physical mechanisms of two-way coupling in particle-laden isotropic turbulence. *Phys. Fluids* **15** (22), 315–329.

FERRY, J. & BALACHANDAR, E. 2001 A fast Eulerian method for disperse two-phase flow. *Int. J. Multiphase Flow* **27**, 1199–1226.

FERRY, J. & BALACHANDAR, E. 2002 Equilibrium expansion for the Eulerian velocity of small particles. *Powder Technology* **125**, 131–139.

FÉVRIER, P. & SIMONIN, O. 2000 Statistical and continuum modelling of turbulent reactive particulate flows. part 2: Application of a two-phase second-moment transport model for prediction of turbulent gas-particle flows. In *Theoretical and Experimental Modeling of Particulate Flows, Lecture Series 2000-06, von Karman Institute for Fluid Dynamics, Rhode Saint Genese (Belgium)*.

FÉVRIER, P., SIMONIN, O. & SQUIRES, K. 2005 Partitioning of particle velocities in gas-solid turbulent flows into a continuous field and a spatially uncorrelated random distribution: Theoretical formalism and numerical study. *J. Fluid Mech.* **533**, 1–46.

FLECKHAUS, D., HISHIDA, K. & MAEDA, M. 1987 Effect of laden solid particles on the turbulent flow structure of a round free jet. *Experiments in Fluids* **5** (323-333).

FORKEL, H. & JANICKA, J. 2000 Large-eddy simulation of a turbulent hydrogen diffusion flame. *Flow Turb. and Combustion* **65** (2), 163–175.

GARCÍA, M., SOMMERER, Y., SCHÖNFELD, T. & POINSOT, T. 2005 Evaluation of euler-euler and euler-lagrange strategies for large-eddy simulations of turbulent reacting flows. In *ECCOMAS thematic conference on computational combustion*. Lisbon, Portugal.

GATIGNOL, R. 1983 The faxén formulae for a rigid particle in an unsteady non-uniform stokes flow. *Journal de mécanique théorique et appliquée* **1(2)**, 143–160.

GERMANO, M. 1992 Turbulence: the filtering approach. *J. Fluid Mech.* **238**, 325–336.

GERMANO, M., PIOMELLI, U., MOIN, P. & CABOT, W. 1991 A dynamic subgrid-scale eddy viscosity model. *Phys. Fluids* **3** (7), 1760–1765.

GHOSAL, S., LUND, T.S., MOIN, P. & AKSELVOLL, K. 1995 A dynamic localization model for large eddy simulation. *J. Fluid Mech.* **286**, 229–255.

HAM, F., APTE, S.V., IACCARINO, G., WU, X., HERRMANN, M., CONSTANTINESCU, G., MAHESH, K. & MOIN, P. 2003 Unstructured les of reacting multiphase flows in realistic gas turbine combustors. In *Annual Research Briefs*. Center for Turbulence Research, NASA Ames/Stanford Univ.

HAM, F. & IACCARINO, G. 2004 Energy conservation in collocated discretization schemes on unstructured meshes. In *Annual Research Briefs*, pp. 3–14. Center for Turbulence Research, NASA Ames/Stanford Univ.

HARDALUPAS, Y., LIU, C.H. & WHITELAW, J.H. 1994 Experiments with disk stabilised kerosene-fuelled flames. *Combust. Sci. Tech.* **97**, 157–191.

HAWORTH, D.C. & POPE, S.B. 1986 A generalized langevin model for turbulent flows. *Physics of Fluids* **2**, 738–744.

HINZE, J.O. 1975 *Turbulence*. New-York: McGraw-Hill.

HIRSCH, C. 1988 *Numerical Computation of internal and external flows*. New York: John Wiley.

HISHIDA, K., KANEKO, K. & MAEDA, M. 1985 Turbulence structire of gas-solid two-phase circular jet. *Trans. JSME* **467** (2330-2337).

HISHIDA, K. & MAEDA, M. 1990 Application of laser/phase Doppler anemometer to dispersed two-phase jet flow. *Particle and Particle Systems Characterization* **7** (1-4), 152–159.

HISHIDA, K., TAKEMOTO, K. & MAEDA., M. 1987 Turbulent characteristics of gas-solids two-phase confined jet. *Japanese Journal of Multiphase Flow* **1** (1), 56–69.

HORIUTI, K. 1989 The role of the bardina model in large eddy simulation of turbulent channel flow. *Phys. Fluids A* **1** (2), 426–428.

HU, H. H. 1996 Direct simulation of flows of solid-liquid mixtures. *Int. J. Multiphase Flow* **22**, 335–352.

HUSSAIN, F. & JEONG, J. 1995 On the identification of a vortex. *J. Fluid Mech.* **285**, 69–94.

JAMESON, A. 1991 Time dependent calculations using multigrid, with applications to unsteady flows past airfoils and wings. *Tech. Rep.* AIAA-91-1596. AIAA 10th Computational Fluid Dynamics Conference.

JAMESON, A., SCHMIDT, W. & TURKEL, E. 1981 Numerical solution of the euler squations by finite volume methods using runge-kutta time stepping schemes. In *14th Fluid and Plasma Dynamic Conference* (ed. AIAA paper 81-1259). Palo Alto.

JIMENEZ, J. & MOIN, P. 1991 The minimal flow unit in near-wall turbulence. *J. Fluid Mech.* **225**, 213–240.

KAUFMANN, A. 2004 Towards Eulerian-Eulerian large-eddy simulation of reactive two-phase flows. PhD thesis, INP, Toulouse.

KAUFMANN, A., HÉLIE, J., SIMONIN, O. & POINSOT, T. 2005 Comparison between Lagrangian and Eulerian particle simulations coupled with dns of homogeneous isotropic decaying turbulence. In *Proceedings of the Estonian Academy of Sciences, Tallinn, Estonia*, , vol. 11, pp. 91–105.

KAUFMANN, A., MOREAU, M., SIMONIN, O. & HELIE, J. 2006 Comparison between Lagrangian and Eulerian mesoscopic modelling approaches for inertial particles suspended in decaying isotropic turbulence. *submitted to J. Comput. Phys.* .

KHALITOV, D. & LONGMIRE, E. 2003 Effect of particle size on velocity correlations in turbulent channel flow. In *4th ASME/FED and JSME Joint Fluids Conference*. Honolulu, Hawaii.

KIM, J. & MOIN, P. 1985 Application of a fractional-step method to incompressible navier-stokes equations. *J. Comput. Phys.* **59** (2), 308–23.

KIM, W.W. & MENON, S. 1999 An unsteady incompressible navier stokes solver for les of turbulent flows. *Int. J. Num. Meth. Fluids* **31**, 983–1017.

KONAN, N. A., SIMONIN, O. & SQUIRES, K. D. 2006 Rough wall boundary condition derivation for particle continuum equations : validation from LES/DPS of gas-solid turbulent channel flow. In *Proceedings of FEDSM2006, ASME Joint U.S.-European Fluids Engineering Summer Meeting, Miami, Floride, USA. ASME FED*, , vol. FEDSM2000-11215.

KULICK, J. D., FESSLER, J. R. & EATON, J. K. 1994 Particle response and turbulence modification in fully developed channel flow. *J. Fluid Mech.* **6**, 3742–3749, eRbib.

LATHOUWERS, D. & BELLAN, J. 2001 Modeling of dense gas-solid reactive mixtures applied to biomass pyrolysis in a fluidized bed. *Int. J. Multiphase Flow* **27** (12), 2155–2187.

LAVIEVILLE, J. 1997 Simulations numériques et modélisation des interactions entre l'entrainement par la turbulence et les collisions interparticulaires en écoulement gaz-solide. PhD thesis, Université de Rouen.

LAX, P. D. & WENDROFF, B. 1960 Systems of conservation laws. *Comm. Pure Appl. Math.* **13**, 217–237.

LELE, S. 1992 Compact finite difference schemes with spectral like resolution. *J. Comput. Phys.* **103**, 16–42.

LENORMAND, E., SAGAUT, P., TA PHUOC, L. & COMTE, P. 2000 Subrig-scale models for large-eddy simulations of compressible wall bounded flows. *Am. Inst. Aeronaut. Astronaut. J.* **41** (6).

LEONARD, A. 1974 Energy cascade in large eddy simulations of turbulent fluid flows. *Adv. Geophys.* **18** (A), 237–248.

LILLY, D.K. 1967 The representation of small-scale turbulence in numerical simulation experiments. In *Proceedings of the IBM Scientific Computing Symposium on Environmental Sciences*. Yorktown Heights, USA.

LILLY, D.K. 1992 A proposed redefinition of the germano subgrid-scale closure method. *Phys. Fluids A* **4**, 633–635.

MAGNAUDET, J., RIVERO, M. & FABRE, M. 1995 Accelerated flows past a solid sphere or a spherical bubble. part 1. steady straining flow. *J. Fluid Mech.* **284**, 97–135.

MAHESH, K., CONSTANTINESCU, G. & MOIN, P. 2004 A numerical method for large-eddy simulation in complex geometries. *J. Comput. Phys.* **197** (1), 215–240.

MARCHIOLI, C., PICCIOTTO, M. & SOLDATI, A. 2006 Particle dispersion and wall-dependent fluid scales in turbulent bounded flow: Implications for local equilibrium models. *J. Turb.* **7** (60), 1–12.

MARTIN, C., BENOIT, L., SOMMERER, Y., NICOUD, F. & POINSOT, T. 2006 Les and acoustic analysis of combustion instability in a staged turbulent swirled combustor. *AIAA Journal* **44** (4), 741–750, jX NF.

MARTIN, M.P., PIOMELLI, U. & CANDLER, G.V. 2000 Subgrid-scale models for compressible large eddy simulations. *Theoretical Computational Fluid Dynamics* **13**, 361–376.

MASSOL, A. 2004 Simulations numériques d'écoulements à travers des réseaux fixes de sphères monodisperses et bidisperses, pour des nombres de Reynolds modérés. PhD thesis, INP, Toulouse.

MAXEY, M.R. 1987 The gravitational settling of aerosol particles in homogeneous turbulence and random flow fields. *J. Fluid Mech.* **174**, 441–465.

MAXEY, M. & RILEY, J. 1983 Equation of motion for a small rigid sphere in a nonuniform flow. *Phys. Fluids* **26** (4).

MENEVEAU, C. & KATZ, J. 2000 Scale-invariance and turbulence models for large eddy simulation. *Ann. Rev. Fluid Mech.* **32**, 1–32.

MOIN, P. 2004 Large-eddy simulation of multiphase turbulent flows in realistic combustors. *Prog. in Comp. Fluid Dynamics* **4**, 237–240.

MOIN, P., SQUIRES, K., CABOT, W. & LEE, S. 1991 A dynamic subgrid-scale model for compressible turbulence and scalar transport. *Phys. Fluids* **A 3** (11), 2746–2757.

MONTAZEL, X., SAMANIEGO, J-M., LACAS, F., POINSOT, T. & CANDEL, S. 1992 Turbulent combustion modelling in a side dump ramjet combustor. In *AIAA/SAE/ASME/ASEE 28th Joint Propulsion Conference and Exhibit* (ed. Paper 92-3599). Nashville, TN: AIAA.

MOREAU, M. 2006 Modélisation numérique directe et des grandes échelles des écoulements turbulents gaz-particules dans le formalisme eulérien mésoscopique. PhD thesis, INP Toulouse.

MOUREAU, V. 2004 Simulation aux grandes échelles de l'aérodynamique interne des moteurs à piston. PhD thesis, Ecole Centrale Paris.

MOUREAU, V., LARTIGUE, G., SOMMERER, Y., ANGELBERGER, C., COLIN, O. & POINSOT, T. 2005 High-order methods for dns and les of compressible multi-component reacting flows on fixed and moving grids. *J. Comput. Phys.* **202** (2), 710–736.

NAMAZIAN, M., KELLY, J. & SCHEFER, R.W. 1992 Concentration imaging measurements in turbulent concentric-jet flows. *Am. Inst. Aeronaut. Astronaut. J.* **30**, 384–394.

ORSZAG, S.A. & PATTERSON, G.S. 1972 Numerical simulation of three-dimensional homogeneous isotropic turbulence. *Phys. Rev. Lett.* **28**, 76–79.

OSEEN, C.W. 1927 *Hydrodynamik*. Leipzig.

PAN, Y. & BANERJEE, S. 1997 Numerical investigation of the effects of large particles on wall-turbulence. *Phys. Fluids* **9**, 3786–3807.

PANDYA, R. & MASHAYEK, F. 2002 Two-fluid large-eddy simulation approach for particle-laden turbulent flows. *Int. J. Heat Mass Transfer* **45**, 4753–4759.

PAOLI, R., HÉLIE, J. & POINSOT, T. 2004 Contrail formation in aircraft wakes. *J. Fluid Mech.* **502**, 361–373.

PASSOT, T. & POUQUET, A. 1987 Numerical simulation of compressible homogeneous flows in the turbulent regime. *J. Fluid Mech.* **181**, 441 – 466.

PICCIOTTO, M., MARCHIOLI, C., REEKS, M. W. & SOLDATI, A. 2005*a* Statistics of velocity and preferential accumulation of micro-particles in boundary layer turbulence. *Nuclear Eng. and Design* **255**, 1239–1249.

PICCIOTTO, M., MARCHIOLI, C. & SOLDATI, A. 2005*b* Characterization of near-wall accumulation regions for inertial particles in turbulent boundary layers. *Phys. Fluids* **17** (098101).

PIOMELLI, U. 1999 Large-eddy simulation: achievements and challenges. *Progress in Aerospace Sciences* **35**, 335–362.

POINSOT, T., HAWORTH, D. & BRUNEAUX, G. 1993 Direct simulation and modelling of flame-wall interaction for premixed turbulent combustion. *Combust. Flame* **95** (1/2), 118–133.

POINSOT, T. & LELE, S.K. 1992*a* Boundary conditions for direct simulation of compressible viscous flows. *J. Comput. Phys.* **101**, 104–129.

POINSOT, T. & LELE, S. 1992*b* Boundary conditions for direct simulations of compressible viscous flows. *J. Comput. Phys.* **101** (1), 104–129.

POPE, S.B. 1994 Lagrangian pdf methods for turbulent flows. *Annu. Rev. Phys. Mech.* **26**, 23–63.

POPE, S. B. 2000 *Turbulent flows*. Cambridge University Press.

PORTER, D.H., POUQUET, A. & WOODWARD, P.R. 1992 Three-dimensional supersonic homogeneous turbulence: A numerical study. *Phys. Rev. Lett.* **68**, 3156–3159.

POZORSKY, J., APTE, S.V. & RAMAN, V. 2004 Filtered particle tracking for dispersed two-phase turbulent flows. In *Proceedings of the Summer Program*. Center for Turbulence Research, NASA Ames/Stanford Univ.

PRIÈRE, C., GICQUEL, L.Y.M., GAJAN, P., STRZELECKI, A.., POINSOT, T. & BÉRAT, C. 2005 Experimental and numerical studies of dilution systems for low emission combustors. *Am. Inst. Aeronaut. Astronaut. J.* **43** (8), 1753–1766.

RANI, S. & BALACHANDAR, E. 2003 Evaluation of the equilibrium Eulerian approach for the evolution of particle concentration in isotropic turbulence. *Int. J. Multiphase Flow* **29**, 1793–1816.

RANI, S. & BALACHANDAR, E. 2004 Preferential concentration of particles in isotropic turbulence: a comparison of the Lagrangian and the equilibrium Eulerian approaches. *Int. J. Multiphase Flow* **141** (1-2), 109–118.

REEKS, M.W. 1991 On a kinetic equation for the transport of particles in turbulent flows. *Phys. Fluids* **3** (3).

REEKS, M. 1992 On the continuum equations for dispersed particles in nonuniform flows. *Phys. Fluids* **4** (6), 1290–1303.

RIBER, E., GARCIA., M., MOUREAU, V., PITSCH, H., SIMONIN, O. & POINSOT, T. 2006 Evaluation of numerical strategies for les of two-phase reacting flows. In *Proc of the Summer Program*. Center for Turbulence Research, NASA Ames/Stanford Univ.

RICHARDSON, L.F. 1922 *Weather Prediction by Numerical Process*, cambridge edn. Cambridge University Press.

RILEY, J.J. & PATERSON, G.S. 1974 Diffusion experiments with numerically integrated isotropic turbulence. *Phys. Fluids* **17**, 292–297.

ROE, P.L. 1984 Generalized formulation of TVD Lax-Wendroff schemes. *Tech. Rep.* ICASE Report 84-53, NASA CR-172478. NASA Langley Research Center.

ROE, P.L. 1987 Error estimates for cell vertex schemes. *Tech. Rep.* ICASE 87-6. NASA LRC, Hampton VA.

ROUSON, D.W.I. & EATON, J.K. 2001 On the preferential concentration of solid particles in turbulent channel flow. *J. Fluid Mech.* **428**, 149–169.

RUDGYARD, M.A. 1990 Cell vertex methods for compressible gas flows. PhD thesis, University of Oxford. UK.

SAGAUT, P. 2000 *Large Eddy Simulation for Incompressible flows*. Springer-Verlag.

SAKIZ, M. 1999 Simulation numérique lagrangienne et modélisation eulérienne d'écoulements diphasiques gaz-particules en canal vertical. Phd thesis, Ecole Nationale des Ponts et Chaussées, France.

SANKARAN, V. & MENON, S. 2002 Les of spray combustion in swirling flows. *J. Turb.* **3**, 011.

SCHEFER, R.W., NAMAZIAN, M. & KELLY, J. 1994 Velocity measurements in turbulent bluff-body stabilized flows. *Am. Inst. Aeronaut. Astronaut. J.* **32** (9), 1844–1851.

SCHILLER, L. & NAUMAN, A. 1935 A drag coefficient correlation. *VDI Zeitung* **77**, 318–320.

SCHMITT, P., POINSOT, T., SCHUERMANS, B. & GEIGLE, K. 2007 Large-eddy simulation and experimental study of heat transfer, nitric oxide emissions and combustion instability in a swirled turbulent high pressure burner. *J. Fluid Mech.* **570**, 17–46.

SCHUMANN, U. 1975 Subgrid scale model for finite difference simulations of turbulent flows in plane channels and annuli. *J. Comput. Phys.* **18**, 376–404.

SELLE, L., BENOIT, L., POINSOT, T., NICOUD, F. & KREBS, W. 2006 Joint use of compressible large-eddy simulation and Helmholtz solvers for the analysis of rotating modes in an industrial swirled burner. *Combust. Flame* **145** (1-2), 194–205.

SELLE, L., LARTIGUE, G., POINSOT, T., KOCH, R., SCHILDMACHER, K.-U., KREBS, W., PRADE, B., KAUFMANN, P. & VEYNANTE, D. 2004 Compressible large-eddy simulation of turbulent combustion in complex geometry on unstructured meshes. *Combust. Flame* **137** (4), 489–505.

SELMIN, V. 1987 Third order finite element schemes for the solution of hyperbolic problems. *Tech. Rep*. INRIA Report, 707. INRIA. Sophia Antipolis, France.

SENGISSEN, A., POINSOT, T., VANKAMPEN, J. & KOK, J. 2005 Response of a swirled non-premixed burner to fuel flow rate modulation. *The Cyprus International Symposium on Complex Effects in Large Eddy Simulation* .

SHOTORBAN, B. & BALACHANDAR, S. 2006 Two-fluid large-eddy simulation approach for gas-particle turbulent flows using equilibrium assumption. In *Proceedings of ASME 2nd Joint U.S.-European Fluids Engineering Summer Meeting, Miami, FL*.

SHUEN, J.S., CHEN, L.D. & FAETH, M. 1983 Evaluation of a stochastic model of particle dispersion in a turbulent round jet. *AIChE J.* **29**, 167–170.

SIMONIN, O. 1991 Prediction of the dispersed phase turbulence in particle-laden jets. In *Proc. 4th Int. Symp. on gas solid flows, ASME FED, ,* vol. 121, pp. 197–206.

SIMONIN, O. 1996 Combustion and turbulence in two phase flows. Lecture Series 1996-02. Von Karman Institute fo Fluid Dynamics.

SIMONIN, O., FEVRIER, P. & LAVIEVILLE, J. 2002 On the spatial distribution of heavy particle velocities in turbulent flow : from continuous field to particulate chaos. *J. Turb.* **3**.

SMAGORINSKY, J. 1963 General circulation experiments with the primitive equations. i: The basic experiment. *Monthly Weather Review* **91(3)**, 99–165.

SMIRNOV, A., SHI, S. & CELIK, I. 2001 Random flow generation technique for large eddy simulations and particle-dynamics modeling. *Trans. ASME. Journal of Fluids Engineering* **123**, 359–371.

SNYDER, W.H. & LUMLEY, J.L. 1971 Some measurements of particle velocity autocorrelation functions in a turbulent flow. *J. Fluid Mech.* **48** (1), 41–71.

SOMMERFELD, M. & QIU, H.H. 1991 Detailed measurements in a swirling particulate two-phase flow by a phase-doppler anemometer. *Int. J. Heat Fluid Flow* **12** (1).

SPEZIALE, C. G. 1985 Galilean invariance of subgrid-scale stress models in the large-eddy simulation of turbulence. *J. Fluid Mech.* **156**, 55–62.

SQUIRES, K. & EATON, J. 1990 Particle response and turbulence modification in isotropic turbulence. *Phys. Fluids* **2** (7), 1191–1203.

SQUIRES, K. & EATON, J. 1991*a* Measurements of particle dispersion obtained from direct numerical simulations of isotropic turbulence. *J. Fluid Mech.* **226**, 1–35.

SQUIRES, K. & EATON, J. 1991*b* Preferential concentration of particles by turbulence. *Phys. Fluids* **3** (5), 1169–1178.

STOESSEL, A., HILKA, M. & BAUM, M. 1994 2d direct numerical simulation of turbulent combustion on massively parallel processing platforms. In *1994 EUROSIM Confence on Massively Parallel Computing*, pp. 793–800. Delft: Elsevier Science B.V., crct CONF.

STOKES, G. G. 1851 On the effect of the inertial friction of fluids on the motions of pendulums. *Trans. Cambridge Phil. Soc.* **9**, 8–23.

TAYLOR, G.I. 1921 Diffusion by continuous movements. *Proc. London Math. Soc* **20**, 196–211.

TCHEN, C.M. 1947 Mean value and correlation problems connected with the motion of small particles suspended in a turbulent fluid. PhD thesis, University of Delft, The Hague.

TOMAICH, T. 1995 A genuinely multi-dimensional upwinding algorithm for the navier-stokes equations on unstructured grids using a compact, highly-parallelizable spatial discretization. PhD thesis, University of Michigan, USA.

TSUJI, Y., MORIKAWA, Y. & SHIOMI, H. 1984 Ldv measurements of an air-solid two-phase flow in a vertical pipe. *J. Fluid Mech.* **139**, 417–434.

VAN LEER, B. 1977 Towards the ultimate conservative difference scheme IV. A new approach to numerical convection. *J. Comput. Phys.* **23**, 276–299.

VANCE, M.W., SQUIRES, K.D. & SIMONIN, O. 2006 Properties of the particle velocity field in gas-solid turbulent channel flow. *Phys. Fluids* **18** (063302).

VERMOREL, O., BEDAT, B., SIMONIN, O. & POINSOT, T. 2003 Numerical study and modelling of turbulence modulation in a particle laden slab flow. *J. Turb.* **4, 025**.

VEYNANTE, D. & KNIKKER, R. 2006 Comparison between LES results and experimental data in reacting flows. *J. Turb.* **7** (35), 1–20.

VIT, C., FLOUR, I. & SIMONIN, O. 1999 Modelling of a confined bluff body flow laden with polydispersed particles. In *Two-Phase Flow Modelling and Experimentation 1999*, pp. 1877–1884. Edizioni ETS.

VON NEUMANN, J. & RICHTMEYER, R. D. 1950 A method for the numerical calculation of hydrodynamic shocks. *J. Appl. Phys.* **21**, 231.

VREMAN, B. 1995 Direct and large-eddy simulation of the compressible turbulent mixing layer. Phd thesis, University of Twente.

VREMAN, B., GEURTS, B. & KUERTEN, H. 1995 Subgrid modeling in LES of compressible flow. *Appl. Sci. Res.* **54**, 191–203.

WANG, L.P., WEXLER, A.S. & ZHOU, Y. 2000 Statistical mechanical description and modelling of turbulent collision of inertial particles. *J. Fluid Mech.* **415**, 117–153.

WANG, Q. & SQUIRES, K. 1996 Large eddy simulation of particle-laden turbulent channel flow. *Phys. Fluids* **8** (5), 1207–1223.

WHITAKER, S. 1999 *The method of volume averaging*. Kluwer Academic Publishers.

YOSHIZAWA, A. & HORIUTI, K. 1985 A statistically-derived subgrid-scale kinetic energy model for the large-eddy simulation of turbulent flows. *J. Phys. Soc. Japan* **54** (8), 2834–2839.

ZAICHIK, L.I. 1999 A statistical model of particle transport and heat transfer in turbulent shear flows. *Phys. Fluids* **11** (6), 1521–1534.

ZANG, T.A., DAHLBURG, R.B. & DAHLBURG, J.P. 1992 Direct and large-eddy simulations of three-dimensional compressible Navier-Stokes turbulence. *Phys. Fluids A* **4** (1), 127–140.

Appendix

Appendix A

Bluffbody: additional graphs

For the sake of clearness, not all the graphs have been included in the discussion of Chapter 6. Hereafter, the missing ones are provided to complete the analysis.

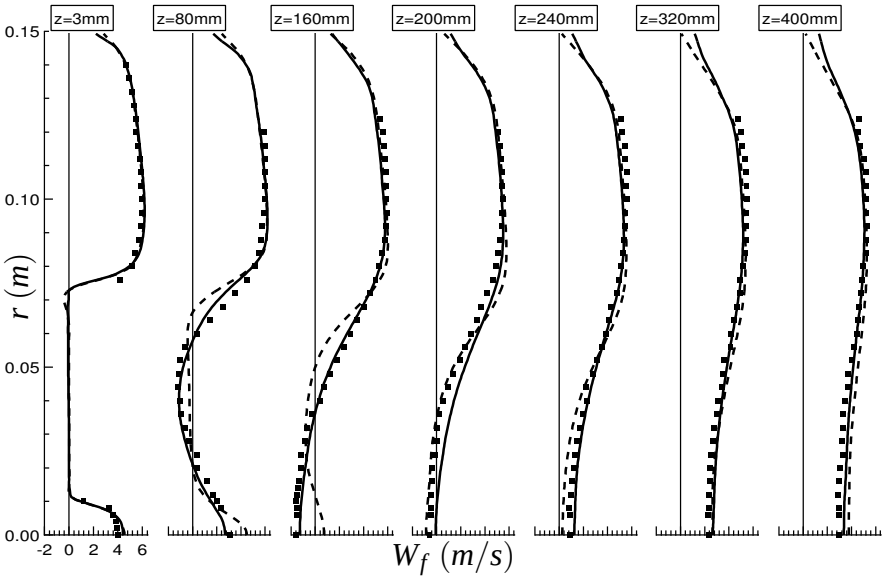

Figure A.1 - **Convective scheme influence.** *Radial profiles of mean axial gas velocity at 7 stations along z axis. Symbols: experiment – Dashed line: Nst1_lw_smago_lwm_norfg – Solid line: Nst1_ttgc_smago_lwm_norfg.*

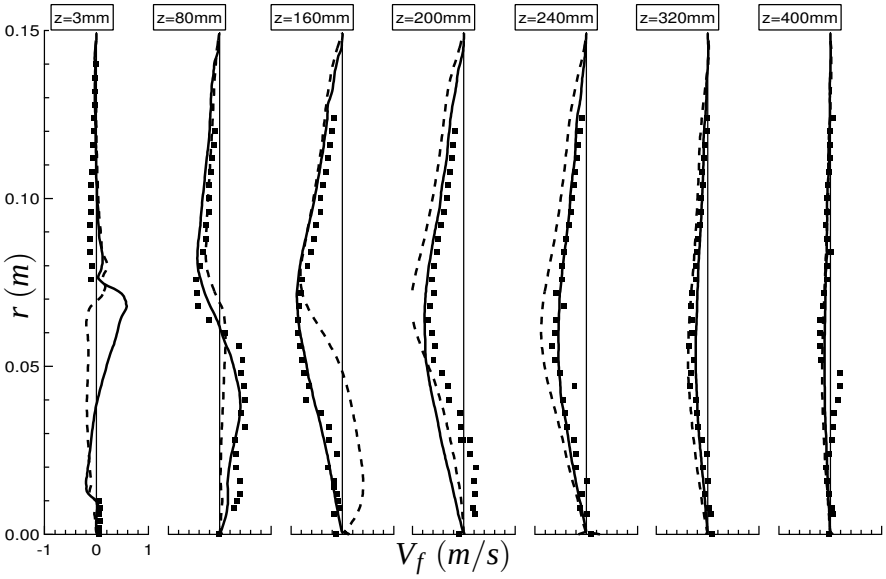

Figure A.2 - **Convective scheme influence.** *Radial profiles of mean radial gas velocity at 7 stations along z axis. Symbols: experiment – Dashed line: Nst1_lw_smago_lwm_norfg – Solid line: Nst1_ttgc_smago_lwm_norfg.*

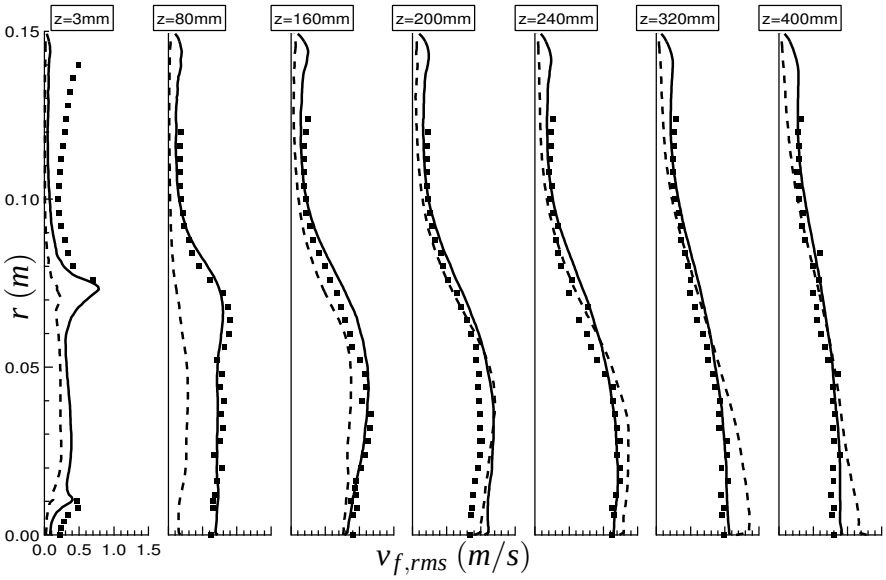

Figure A.3 - **Convective scheme influence.** *Radial profiles of RMS radial gas velocity at 7 stations along z axis. Symbols: experiment – Dashed line: Nst1_lw_smago_lwm_norfg – Solid line: Nst1_ttgc_smago_lwm_norfg.*

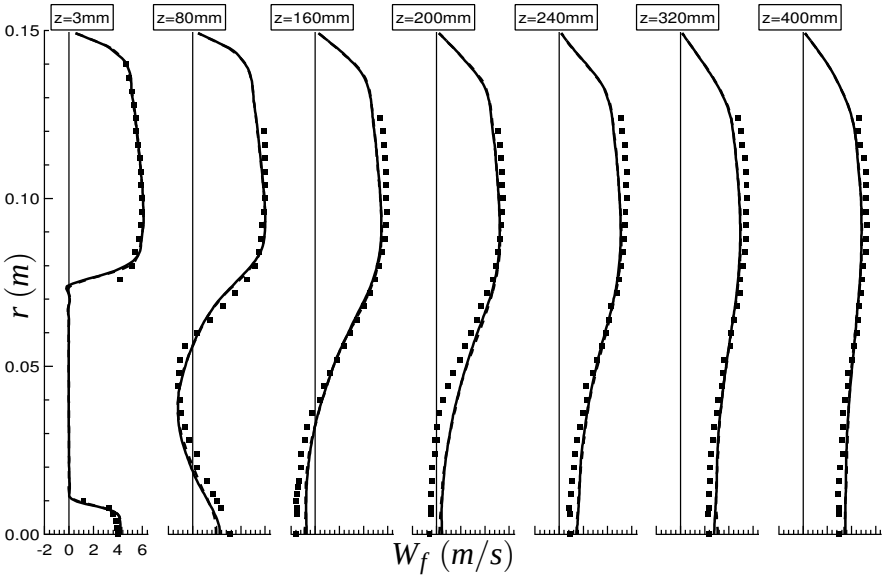

Figure A.4 - **Grid influence.** *Radial profiles of mean axial gas velocity at 7 stations along z axis. Symbols: experiment – Dashed line: Nst1_ttgc_wale_wnm_rfgint – Solid line: Nst2_ttgc_wale_wnm_rfgint.*

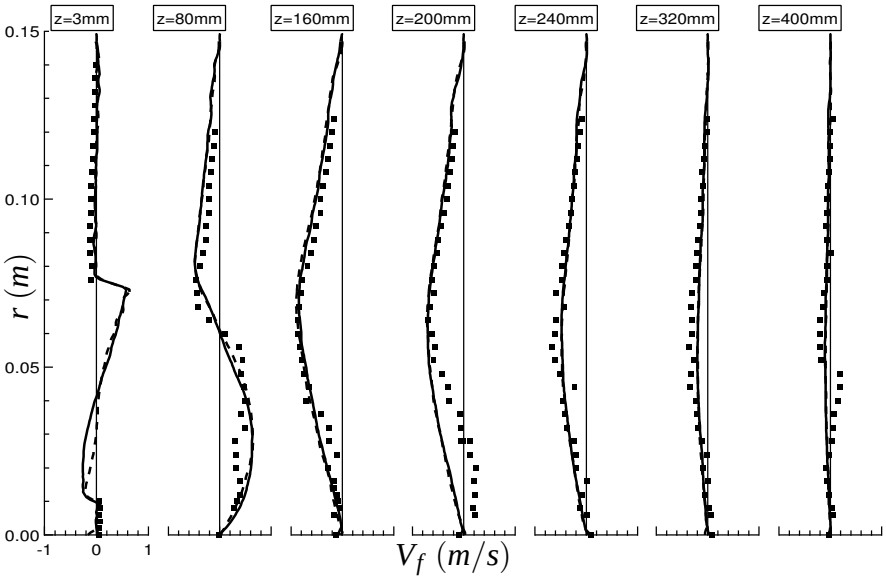

Figure A.5 - **Grid influence.** *Radial profiles of mean radial gas velocity at 7 stations along z axis. Symbols: experiment – Dashed line: Nst1_ttgc_wale_wnm_rfgint – Solid line: Nst2_ttgc_wale_wnm_rfgint.*

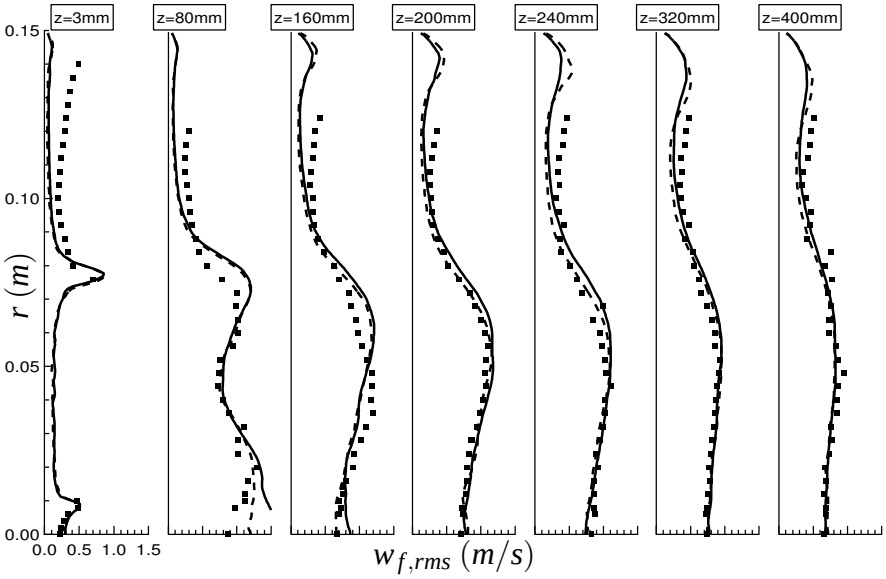

Figure A.6 - **Grid influence.** *Radial profiles of RMS axial gas velocity at 7 stations along z axis. Symbols: experiment – Dashed line: Nst1_ttgc_wale_wnm_rfgint – Solid line: Nst2_ttgc_wale_wnm_rfgint.*

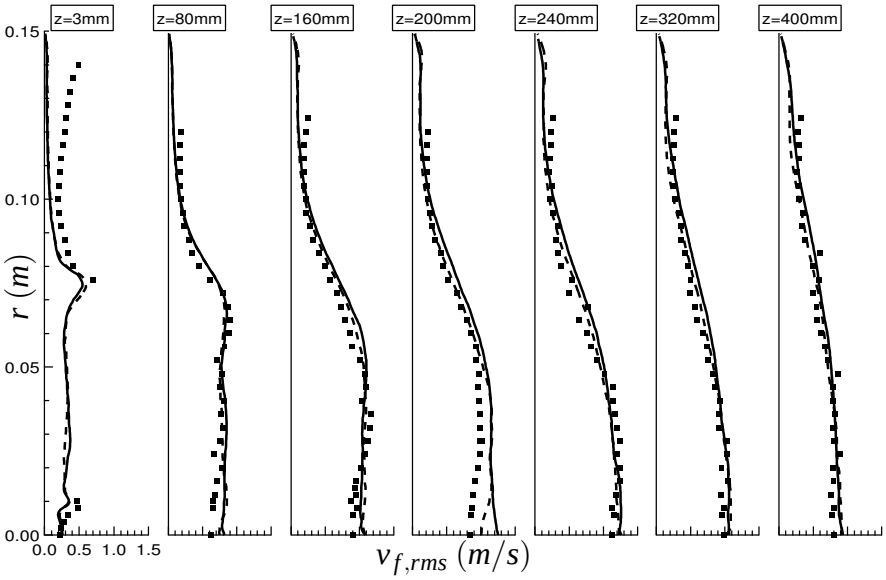

Figure A.7 - **Grid influence.** *Radial profiles of RMS radial gas velocity at 7 stations along z axis. Symbols: experiment — Dashed line: Nst1_ttgc_wale_wnm_rfgint – Solid line: Nst2_ttgc_wale_wnm_rfgint.*

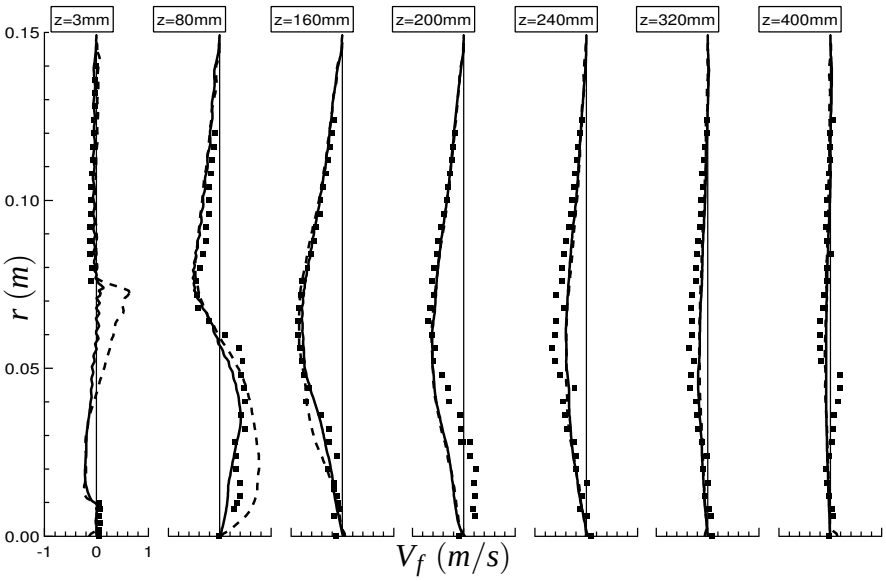

Figure A.8 - **Grid influence.** *Radial profiles of mean radial gas velocity at 7 stations along z axis. Symbols: experiment – Dashed line: Nst2_ttgc_wale_wnm_rfgall– Solid line: St_ttgc_wale_wnm_rfgall.*

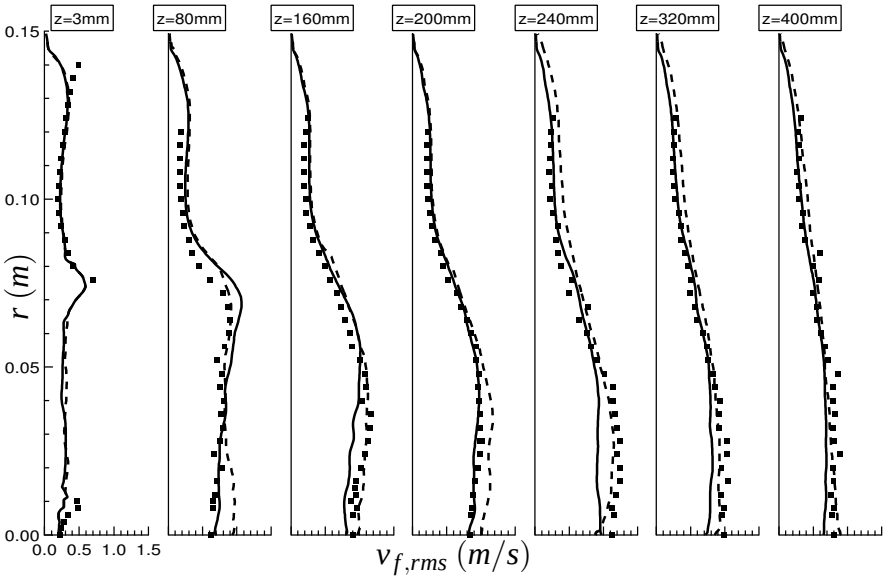

Figure A.9 - **Grid influence.** *Radial profiles of RMS radial gas velocity at 7 stations along z axis. Symbols: experiment – Dashed line: Nst2_ttgc_wale_wnm_rfgall– Solid line: St_ttgc_wale_wnm_rfgall.*

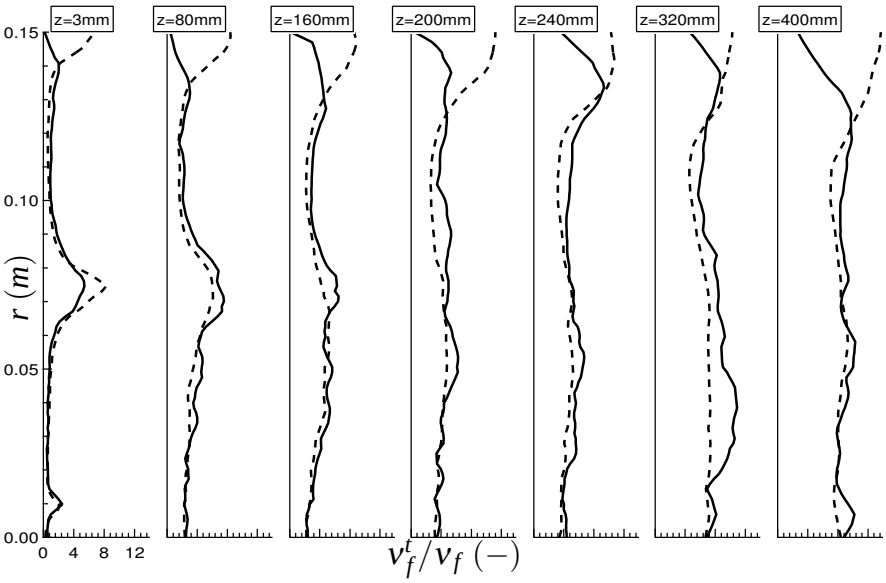

Figure A.10 - **LES and wall modeling influence.** *Radial profiles of mean non-dimension turbulent viscosity at 7 stations along z axis. Symbols: experiment – Dashed line: Nst1_ttgc_smago_lwm_norfg – Solid line: Nst1_ttgc_wale_wnm_norfg.*

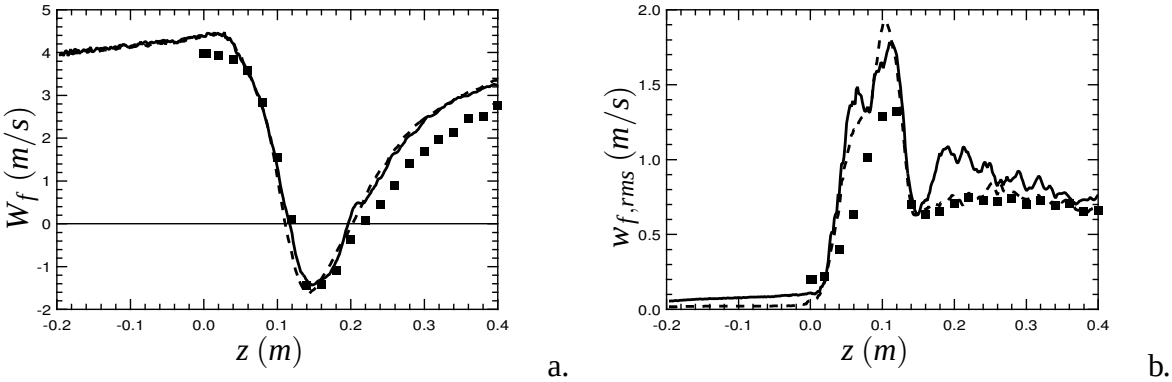

a. b.

Figure A.11 - **LES and wall modeling influence.** *Axial profiles of mean (a.), and RMS (b.), axial gas velocity. Symbols: experiment – Dashed line: Nst1_ttgc_smago_lwm_norfg – Solid line: Nst1_ttgc_wale_wnm_norfg.*

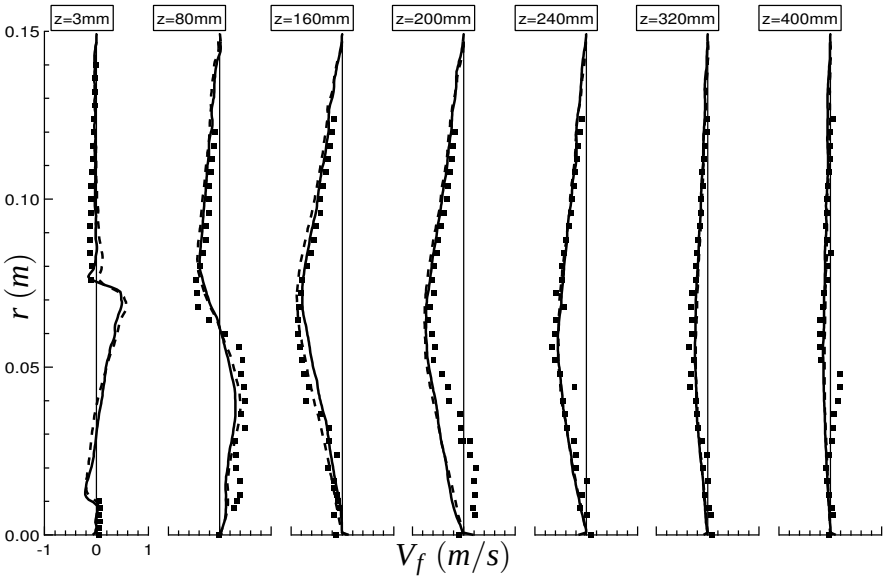

Figure A.12 - **LES and wall modeling influence.** *Radial profiles of mean radial gas velocity at 7 stations along z axis. Symbols: experiment – Dashed line: Nst1_ttgc_smago_lwm_norfg – Solid line: Nst1_ttgc_wale_wnm_norfg.*

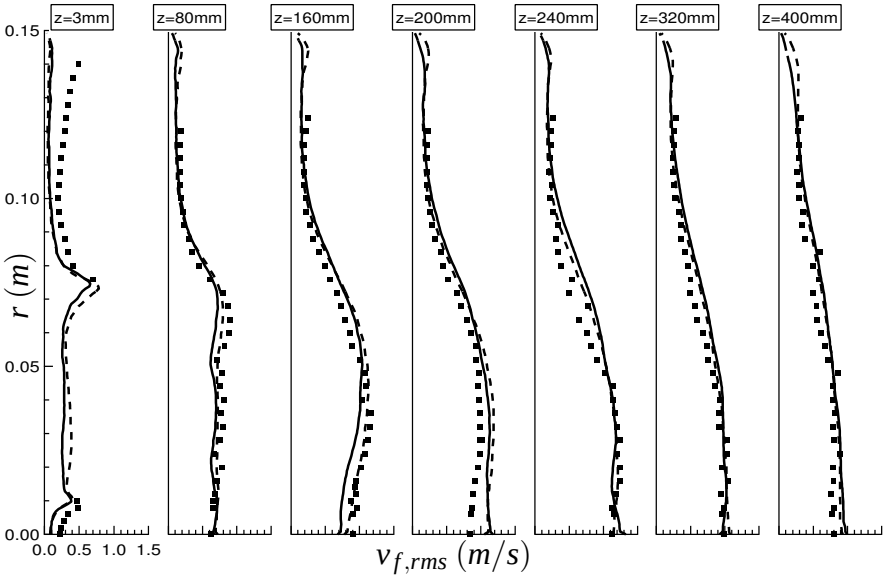

Figure A.13 - **LES and wall modeling influence.** *Radial profiles of RMS radial gas velocity at 7 stations along z axis. Symbols: experiment – Dashed line: Nst1_ttgc_smago_lwm_norfg – Solid line: Nst1_ttgc_wale_wnm_norfg.*

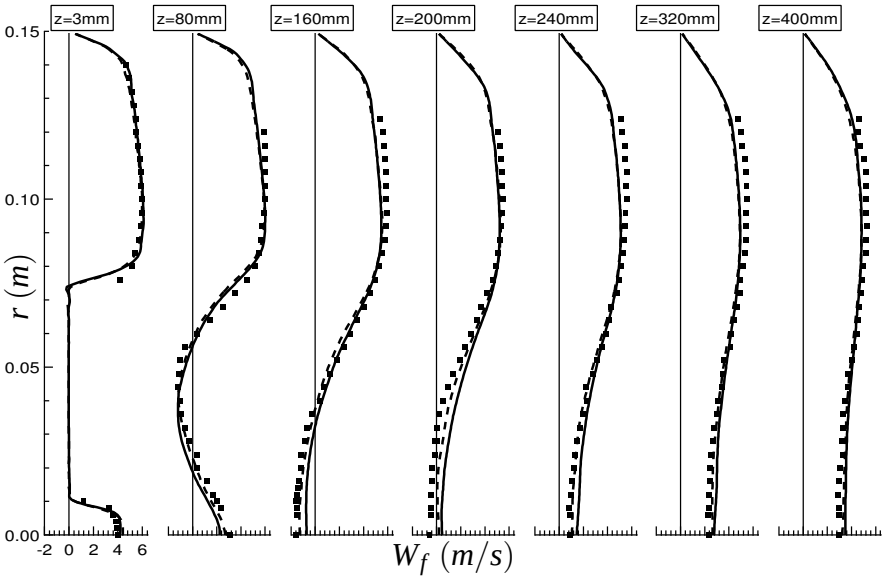

Figure A.14 - **Inner tube turbulent forcing influence.** *Radial profiles of mean axial gas velocity at 7 stations along z axis. Symbols: experiment – Dashed line: Nst1_ttgc_wale_wnm_norfg – Solid line: Nst1_ttgc_wale_wnm_rfgint.*

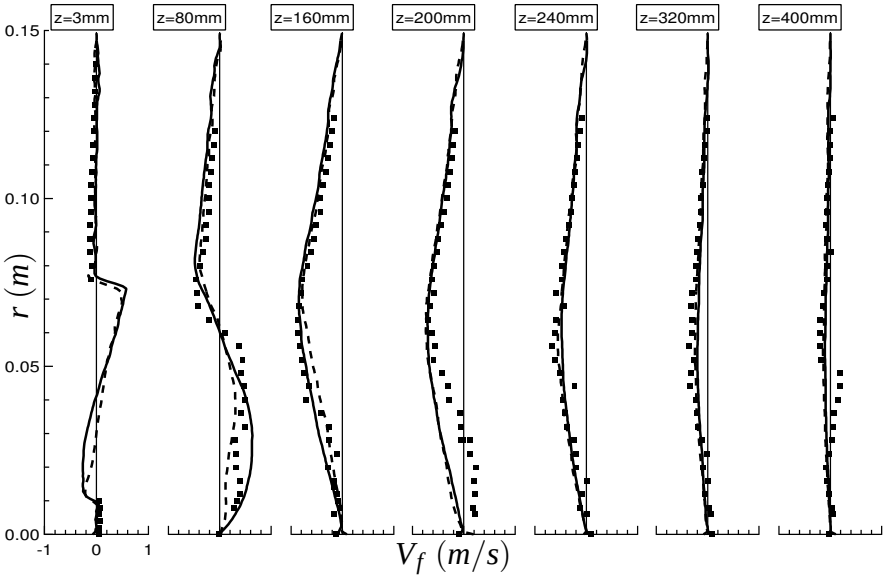

Figure A.15 - **Inner tube turbulent forcing influence.** *Radial profiles of mean radial gas velocity at 7 stations along z axis. Symbols: experiment – Dashed line: Nst1_ttgc_wale_wnm_norfg – Solid line: Nst1_ttgc_wale_wnm_rfgint.*

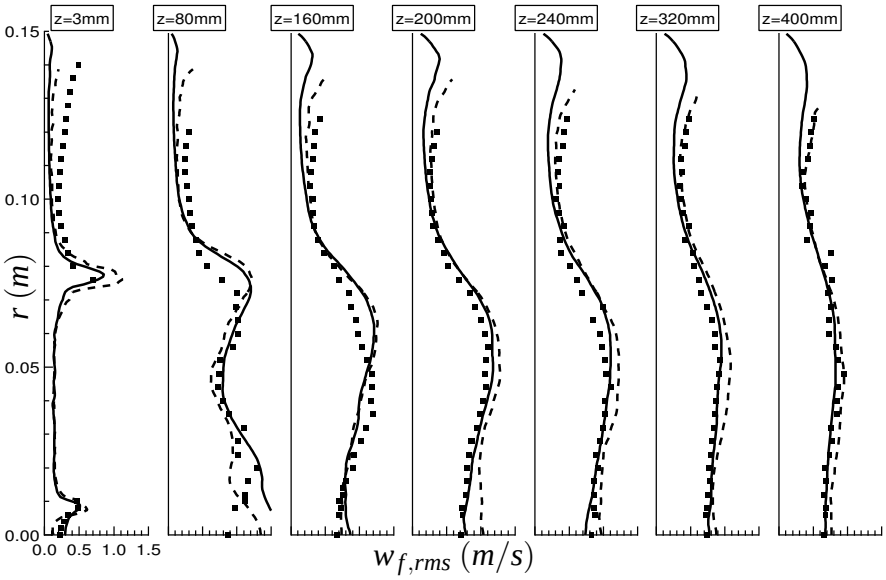

Figure A.16 - **Inner tube turbulent forcing influence.** *Radial profiles of RMS axial gas velocity at 7 stations along z axis. Symbols: experiment – Dashed line: Nst1_ttgc_wale_wnm_norfg – Solid line: Nst1_ttgc_wale_wnm_rfgint.*

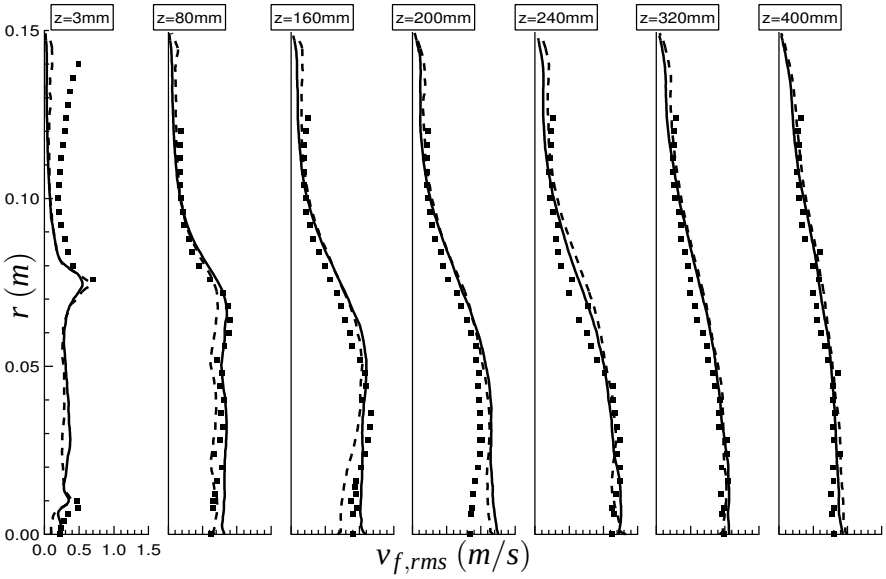

Figure A.17 - **Inner tube turbulent forcing influence.** *Radial profiles of RMS radial gas velocity at 7 stations along z axis. Symbols: experiment – Dashed line: Nst1_ttgc_wale_wnm_norfg – Solid line: Nst1_ttgc_wale_wnm_rfgint.*

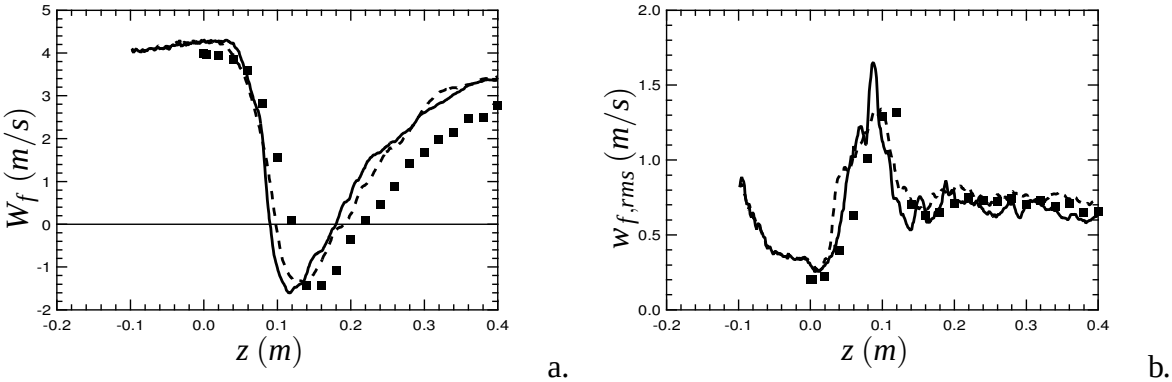

Figure A.18 - **Coflow turbulent forcing influence.** *Axial profiles of mean (a.), and RMS (b.), axial gas velocity. Symbols: experiment – Dashed line: Nst2_ttgc_wale_wnm_rfgint – Solid line: Nst2_ttgc_wale_wnm_rfgall.*

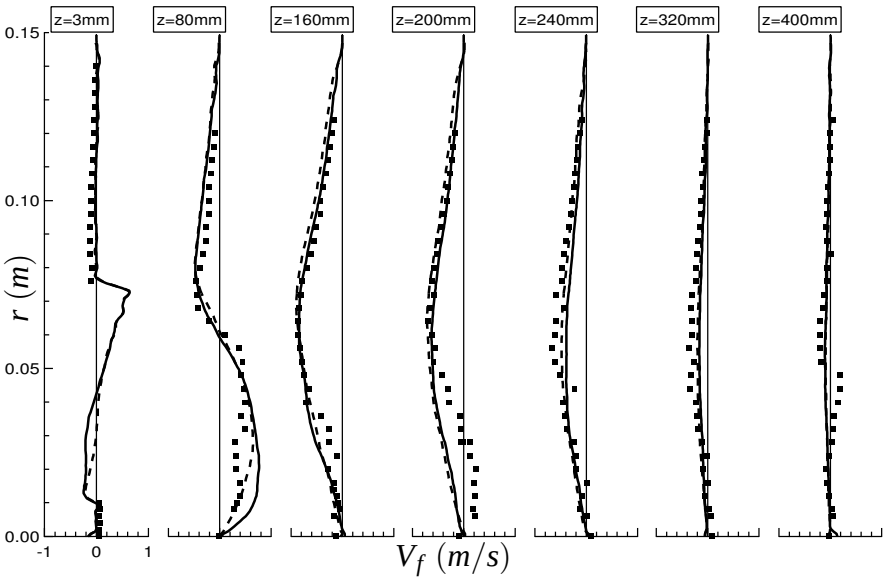

Figure A.19 - **Coflow turbulent forcing influence.** *Radial profiles of mean radial gas velocity at 7 stations along z axis. Symbols: experiment — Dashed line: Nst2_ttgc_wale_wnm_rfgint – Solid line: Nst2_ttgc_wale_wnm_rfgall.*

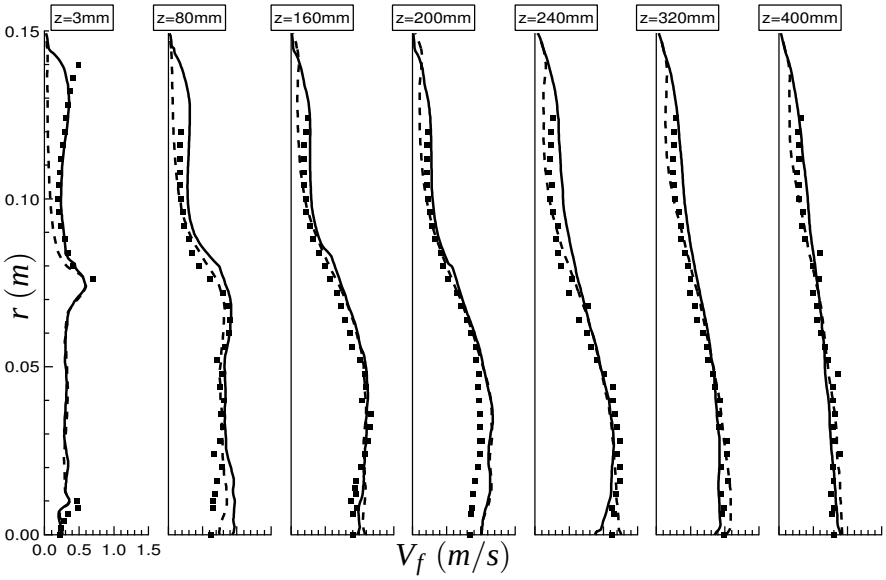

Figure A.20 - **Coflow turbulent forcing influence.** *Radial profiles of RMS radial gas velocity at 7 stations along z axis. Symbols: experiment – Dashed line: Nst2_ttgc_wale_wnm_rfgint – Solid line: Nst2_ttgc_wale_wnm_rfgall.*